UNIVERSITY OF CALIFORNIA SAN DIEGO

Cellular and Biochemical Underpinnings of Stem Cell Gene Therapies for Cystinosis

A thesis submitted in partial satisfaction of the requirements
for the degree Master of Science

in

Biology

by

Meisha Mahnoor Naz Khan

Committee in charge:

Professor Stephanie Cherqui, Chair
Professor Stephen Hedrick, Co-Chair
Professor Gen-Sheng Feng
Professor Aleem Siddiqui

2020

The Thesis of Meisha Mahnoor Naz Khan is approved, and it is acceptable in quality and form for publication on microfilm and electronically:

Co-Chair

Chair

University of California San Diego

2020

DEDICATION

To my dearest cousin, Saba Appa, the resilient Wind:

Into this Universe, and why not knowing,
Nor whence, like Water willy-nilly flowing:
And out of it, as Wind along the Waste,
I know not whither, willy-nilly blowing.
Omar Khayyam

To my dearest grandfather, Abba, whose wisdom knew no bounds:

نا تھا کچھ تو خدا تھا، کچھ نا ہوتا تو خدا ہوتا
ڈبایا مجھ کو ہونے نے، نا ہوتا میں تو کیا ہوتا؟
Ghalib Mirza

and

To my beloved parents, brother, and family,
whose selfless sacrifices, relentless love, and innumerable prayers safeguarded my journey.

EPIGRAPH

میں کنارے پر رہتا ہوں
، آپ پاگل پن کی وجوہات جاننا چاہتے ہیں
آپ نے دروازہ کھٹکھٹایا اور یہ کھلتا ہے
!میں اندر سے ٹہل رہا ہوں باہر
اصل قدر پاگل پن سے آتی ہے
معذرت ، نیچے سائنسدان۔

ہر ایک محبت کرتا ہے
چوٹ اور غم کی زد میں
یہ خالی پن میں غائب ہوجاتا ہے
ایک ہزار نئی مساج

I have lived on the lip
of insanity, wanting to know reasons,
knocking on a door. It opens.
I've been knocking on the inside!

Real value comes from madness
matzub below, scientist above.

Whoever finds love
beneath hurt and grief
disappears into emptiness
with a thousand new disguises.

Jalāl ad-Dīn Muhammad Rūmī

TABLE OF CONTENTS

LIST OF FIGURES

LIST OF SUPPLEMENTAL FILES

Supplemental File 1: Supplementary materials for Chapter 2

Supplemental File 2: Supplementary materials for Chapter 3

Supplementary Videos 2.1, 2.2: 3D modeling of eGFP BMDM and IC-21 reveals TNT-like protrusions above surface of dish

Supplementary Videos 2.3, 2.4, 2.5: 3D-modeling of cystinosin- and frataxin-eGFP IC-21 with DsRed+ fibroblasts reveal intercellular transfer of lysosomes and mitochondria through macrophage-derived membrane protrusions

ACKNOWLEDGEMENTS

I would like to sincerely thank Dr. Stephanie Cherqui for affording me the opportunity to join her research team and pursing my master's degree in her lab. As a leading pioneer in the world of gene therapy for cystinosis, you inspire me as a young woman in science to tenaciously and passionately pursue my ambitions. I am immensely indebted to (Dr.!) Spencer Goodman for his patient mentorship. You have taught me everything I know about research and I cannot thank you enough. A huge thank you to all my amazing lab members who all at some point had to answer my incessant questions. I also want to thank Tatiana Lobry for accepting my resume and passing it over to Spencer one fateful day in 2018 – you quite literally changed my life. I would like to extend a grateful token of appreciation to my committee members for taking the time out of their busy schedules to assist me in the inception of my scientific journey. A huge thank you to Jeanette Fox, for coordinating the BS/MS program so gracefully. Finally, a humble thank you to my family and friends for all the love; this one is for you.

Chapter 1, in part, is currently being prepared for submission for publication of the material, *Goodman S., **Khan M**., Sharma J., Cano J., Zi, L., Estrada, V., Gertsman, I., Cherqui, S. "Shpk-deficient hematopoietic stem cell therapy remains effective to rescue cystinosis."* The master's thesis author was a key investigator and author of this paper.

Chapter 2, in part, is a reprint of the material as it appears in *Goodman, S., Naphade, S., **Khan, M.**, Sharma, J. & Cherqui, S. Macrophage polarization impacts tunneling nanotube formation and intercellular organelle trafficking. Sci Rep 9, 14529, doi:10.1038/s41598-019-50971-x (2019).* The master's thesis author was a key investigator and author of this paper.

Chapter 3, in part, is currently being prepared for submission for publication of the material, *Goodman S., **Khan M**., Sharma J., Cano J., Zi, L., Estrada, V., Gertsman, I., Cherqui, S. "Shpk-deficient hematopoietic stem cell therapy remains effective to rescue cystinosis."* The master's thesis author was a key investigator and author of this paper.

VITA

2018	Bachelor of Science, University of California San Diego
2016-2018	Undergraduate Researcher, University of California San Diego
2017, 2019	Teaching Assistant, University of California San Diego
2018	Research Assistant, Samumed
2018-2020	Undergraduate/Graduate Researcher, University of California San Diego

PUBLICATIONS

Goodman, S., Naphade, S., **Khan, M**., Sharma, J., & Cherqui, S. Macrophage polarization impacts tunneling nanotube formation and intercellular organelle trafficking. *Sci Rep* **9,** 14529 (2019). https://doi.org/10.1038/s41598-019-50971-x

Goodman, S., **Khan, M**., Sharma, J., Cano, J., Zi, L., Estrada, V., Gertsman, I., & Cherqui, S. Shpk-deficient hematopoietic stem cell therapy remains effective to rescue cystinosis. (2020) Manuscript in progress.

ABSTRACT OF THE THESIS

Cellular and Biochemical Underpinnings of Stem Cell Gene Therapies for Cystinosis

by

Meisha Mahnoor Naz Khan

Master of Science in Biology

University of California San Diego, 2020

Professor Stephanie Cherqui, Chair
Professor Stephen Hedrick, Co-Chair

Cystinosis is an early onset multisystemic lysosomal storage disorder characterized by deleterious *CTNS* gene mutations causing defective export and crystallization of amino acid dimer cysteine within lysosomes. Previous studies found that wild-type hematopoietic stem and progenitor cell (HSPC) transplantation into cystinotic (*Ctns*$^{-/-}$) mice prevents disease progression via HSPC-derived macrophage-mediated TNT delivery of functional *Ctns*-carrying lysosomes to diseased cells. While Phase I/II clinical trials for *ex vivo* lentivirally gene-corrected autologous HSPC transplantation is ongoing at UC San Diego, this approach does not yet extend to 40% of patients harboring homozygous 57 kilobase pair mutations eliminating both *CTNS* and neighboring pentose phosphate pathway *SHPK* genes. With roles in both

metabolism and macrophage polarization, understanding the clinical relevance of *SHPK* to our macrophage-based gene therapy is essential to elucidate if *SHPK*-deficient patients are likely to benefit from the therapy. In this pursuit, we examined the role of polarization conditions mediating macrophage-derived TNT intracellular trafficking in robust *in vitro* and *in vivo* systems. We generated novel *Shpk* knockout (*Shpk*$^{-/-}$) mice models which upheld mild metabolic phenotypes as a consequence of isolated *Shpk*-deficiency. Furthermore, we found that *Shpk*$^{-/-}$/*Ctns*$^{+/+}$ HSPC transplantation into lethally-irradiated cystinotic *Ctns*$^{-/-}$/*Shpk*$^{+/+}$ mice resulted in normal macrophage tissue integration, restored *Ctns* mRNA expression, reduced cystine content, and improved renal function, inducing widespread disease rescue. Ultimately, these findings provide insight into the pathogenic role of *SHPK* in cystinosis, validate the utility of HSPC transplantations as gene-modifying therapies for disorders of similar cellular/molecular underpinnings, and confirms eligibility of patients with *SHPK*-deficiency for cystinosis clinical trials.

Chapter 1: Introduction

The following section 1, in part, is a reprint of material that appears in *Scientific Reports* on October 10, 2019.
The following section 1, in part, is a reprint of a manuscript entitled "*Shpk*-deficient hematopoietic stem cell therapy remains effective to rescue cystinosis" that is in preparation for publication.

1.1: Cystinosis. Cystinosis is an autosomal-recessive lysosomal storage disorder (LSD) characterized by defective export and subsequent crystallization of cystine in lysosomes, causing early onset multisystemic metabolic and physiological dysregulation (Cherqui et al., 2002). Lysosomes are membrane-bound organelles tasked with cellular waste removal through hydrolytic degradation (via hydrolyses) and subsequent expulsion (via transporters) of biomolecules (Pu et. Al., 2016). In cystinosis, deleterious mutations of ubiquitously expressed *CTNS* gene on chromosome 17p13 incapacitates cystinosin, a transmembrane cystine-proton co-transporter localized to lysosomes (Cherqui et al., 2002). This protein facilitates transport of cystine, a stabilized dimerized biproduct of amino acid cysteine (Kalatzis et al., 2004). However, truncated cystinosin activity prevents lysosomal efflux of insoluble cystine content, which amasses into crystalized deposits throughout the body. Compromised cellular excretion of waste materials ultimately destroys normal kidney, eye, muscle, liver, pancreas, and brain function (Elmonem et al., 2016).

The hallmark condition of cystinosis is chronic kidney malfunction, also known as nephropathy (Bäumner and Weber 2018). This rare disease (1:100,000 cases) manifests as three main clinical forms with varying symptomatic severity and onset age: infantile nephropathic cystinosis (infants), juvenile nephropathic cystinosis (adolescents), and non-nephropathic cystinosis (adults) (Bäumner and Weber 2018). Infantile nephropathic cystinosis is the most common and severe of the subtypes, in which symptoms appear within the first birth year and may be fatal if untreated. The hallmark symptom is Fanconi Syndrome, a pediatric disease characterized by fractured nutrient reuptake by proximal tubules of the kidney causing polyuria, polydipsia, and acidosis (Cherqui and Courtoy 2017; Cherqui et al., 2002; Haffner et al., 1999). In addition, patients also experience glomerular impairments, rickets, growth retardation, corneal crystallization causing photophobia, cystine deposition-induced cellular and tissue dysfunction, and

ultimately failure to thrive Emma et al., 2014; Cherqui et al., 2002). Symptomatic onsets in juvenile nephropathic cystinosis occur in adolescence, presenting with less severe symptoms of renal dysregulation, as well as photophobia, muscle atrophy, diabetes, cerebral neuromotor impairments, and hypothyroidism (Bäumner and Weber 2018). The third non-nephropathic form of cystinosis primarily occurs in adults and is characterized by corneal complications leading to photophobia, with no renal dysregulation. Current treatment options include drug-based abatement of cystine crystal deposition and kidney transplant restoration of renal function, but are far from holistically curative or permanent (Ariceta et al., 2019). The field of stem cell gene therapy has shown promising potential as an alternative long-lasting remedial therapy (Rocca and Cherqui 2019).

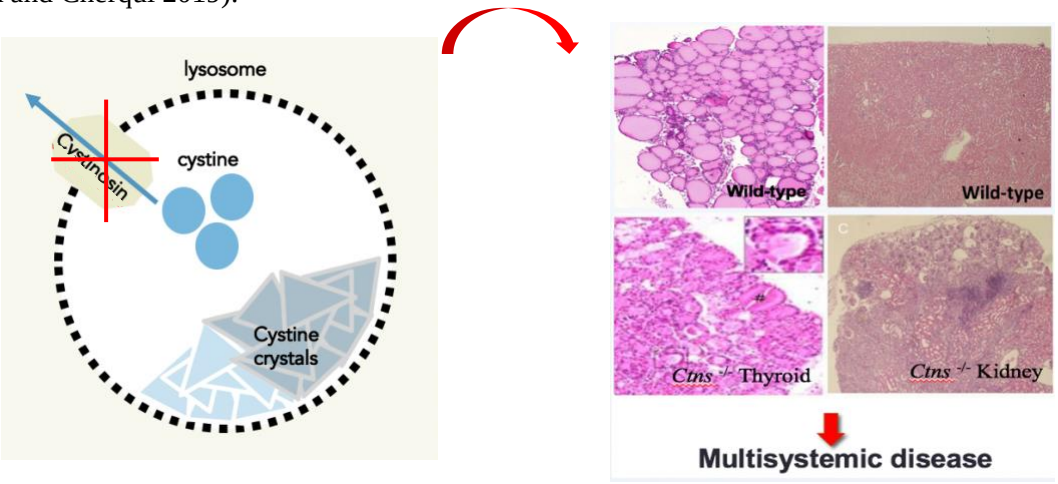

Figure 1.1: Schematic of cystinosis molecular and physiological pathogenesis. Accreted cystine crystalizes within lysosomes causing degradation of thyroid and kidney morphology. Adapted from Gaide Chevronnay et al., 2016; Yeagy et al., 2011.

1.2: Genetic Underpinnings. Investigations into the genetic bases of cystinosis have revealed over 100 existing mutations of the *CTNS* gene, most of which compromise cystinosin transporter function (Elmonem et al., 2016). Bi-allelic loss of *CTNS* characterizes the severity of infantile nephropathic cystinosis in 95% of patients, causing cystine accumulation and renal dysfunction in the first year after birth and gradually overtaking tissue functions by young adolescence (Touchman et al, 2000). Juvenile nephropathic and non-nephropathic cystinosis harbor milder phenotypes associated with heterozygous or compounded heterozygous mutations causing defective cystinosin in 5% of patients (Bäumner and Weber 2018). However, direct linkage of genotype-phenotype correlations is yet to be determined (Kalatzis et al., 2014).

The most common mutation of cystinosis affecting 40% of patients constitutes a 57 kilobase pair (kb) homozygous deletion spanning all 12 *CTNS* exons, as well as partial eliminations of neighboring genes *TRPV-1* and *SHPK* (Touchman et al, 2000). The *TRPV-1* gene encodes capsaicin receptor and the vanilloid receptor 1 protein which facilitates pain and heat sensitivity; deletions in the non-coding regions of *TRPV-1* halt sensitivity to spices and temperature-related pain in mice (Buntix et al., 2016). While consequences of the 57-kbp deletion has been well elucidated in relation to *TRPV-1*, genotype-phenotype correlations between *SHPK* and cystinosis appear less clear (Wamelink et al., 2015). The *SHPK* gene encodes sedoheptulokinase, a pentose phosphate pathway (PPP) enzyme that metabolizes glycolysis intermediates to provide derivative carbon sources for glucose metabolism (Haschemi and Nagy 2013). Clinical studies have reported *SHPK*-deficiency (SHPKD) as a consequence of the 57-kbp mutation, causing elevated urinary levels of erythritol and sedoheptulose which are PPP substrates affected by *SHPK* metabolic activity. However, patient genome profiles and symptom presentations are extremely variable, complicating genotypic-phenotypic tracing to cystinosis (Wamelink et al., 2015). Nevertheless, metabolic perturbations associated with SHPKD in cystinosis patients suggests that the gene may play a role in the clinical heterogeneity of the disease (Wamelink et al., 2015).

1.3: Existing Therapies and Limitations. Current cystinosis therapies provide limited preventative measures that focus on the molecular restoration of cystine lysosomal export and physiological mediation of multisystemic tissue dysfunction (e.g., renal and ocular dysregulation) (Ariceta et al., 2019). Cysteamine, the main therapeutic drug for cystinosis since 1976, has clinically proven effective in enabling lysosomal cystine export which enacts these molecular and physiological remedies, prolonging life-expectancy to late adulthood (Biff 2017). Cysteamine provides an alternative mechanism for cystine depletion: degradation of cystine crystals into catabolized cysteine and cysteine-cysteamine disulfide which can be rapidly exported out of lysosomes via respective transport proteins cationic cysteine transporter and lysine/arginine transporter (Theone et al., 1976). As a result, cellular and tissue function is improved throughout the body following appropriate oral or eye drop cysteamine administration (Ariceta et al., 2019).

Although effective in managing disease progression, cysteamine has several drawbacks. Patients must ascribe to stringent drug dosing schedules supplemented with several additional regulatory medications such as indomethacin and angiotensin modulators; procedures such as immunosuppressive and proton pump inhibitor therapies; and specified diet and exercise (Emma et al., 2014), outside of which mortality rates remain low (Bäumner and Weber 2018). Side effects of cysteamine include digestion issues, vomiting, appetite loss, and unpleasant odors (Cherqui et al., 2002). Patients may also undergo multiple kidney transplantations when cystine depletion fails to prevent End Stage Renal Disease (ESRD). Complications following transplants include grafting survival, redevelopment of ESRD, diabetes, hypothyroidism, and hepatic and neurological impairments (Cohen et. al., 2015). Ultimately, cystine depletion therapies merely circumvent genetic lysosomal defects, delay consequential multisystemic dysfunctions, and do not account for long-term intracellular damage (Bäumner and Weber 2018). While previous therapies address molecular and physiological underpinnings of cystinosis, new avenues in gene therapy reveal yet another fundamental biological level that can be clinically targeted – the *genomic* level.

1.4: LSD Cross-Correction and advent of HSPC Gene Therapy. "Cross-correction" refers to the secretion-and-recapture mechanism and subsequent lysosome-targeting of WT-secreted LSD enzymes exhibited by LSD diseased cells (Hasilik et al., 1980). Enzyme replacement therapies (ERT) employ this cross-correction phenomenon through lifelong intravenous administration of respective recombinant LSD enzymes for disease improvement in Pompe disease, type I Gaucher disease, Fabry disease, and MPS, type I, II, IVA VI, and VII (Penati et al., 2017). ERT cross-correction has proven uniquely viable as a LSD gene therapy mechanism for several reasons: (1) The recessive, single-gene nature of LSDs are well-elucidated and patho-physiologically reproducible in animal models for use in clinical therapeutic studies; (2) clinical analyses of cross-correctional in mild LSD patients indicate the replenishing a small fraction of otherwise-absent enzymatic activity can contribute to long-term and widespread disease mediation; and (3) successful gene therapy methods of ERT may provide supranormal quantities of lysosomal enzymes that can be captured by enzyme-deficient tissue for systemic disease recovery (Rastall and Amalfitano 2015).

However, ERT are limited to secretory LSD enzymes, can instigate immune responses to foreign recombinant DNA, and are inaccessible to blood brain barrier, preventing resolution of CNS phenotypes (Penati et al., 2017). In response to ERT limitations, transplanted hematopoietic stem and progenitor cell (HSPCs) have been shown to mobilize from the bone marrow, home to diseased tissue, and differentiate into healthy immune cell progenies capable of delivering functional proteins for LSDs such as Metachromatic leukodystrophy (MD) (Biffi et al., 2006) and mucopolysaccharidosis type I (MPS-I) (Penati et al., 2017). As such, HSPCs evade antithetical immune responses via immune system reconstitution, facilitate autologous gene modification, and provide life-long supply of otherwise-absent LSD enzymes at the cellular and systemic levels following tissue integration of HSPC immune progenies (Syres et al., 2009).

The Cherqui lab evaluated the utility of stem cell-based therapies for cystinosis using our novel cystinosin-deficient (*Ctns*$^{-/-}$) mice generated to characterize the pathology and treatment of cystinosis (Cherqui et al., 2002). These mice have been shown to effectively reproduce many symptomatic characteristics of human cystinosis (Cherqui et al., 2002). Our lab investigated the therapeutic efficacy of healthy HSPC reconstitution into *Ctns*$^{-/-}$ diseased mice and its mechanism for functional cystinosin protein delivery (Syres et al., 2009). Transplantation of wild-type (WT) HSPCs resulted in abundant tissue integration of bone marrow-derived cells, significant decrease of cystine accumulation (up to 97% clearance) (Syres et al., 2009), and long-term preservation of the kidney, eye, and thyroid (Yeagy et al., 2011; Rocca et al., 2015; Gaide Chevronnay et al., 2016). Then, an autologous lentiviral-corrected HSPC transplantation protocol was established using congenic HSPCs lenti-virally transduced with human *CTNS* (Harrison et al., 2013). Lentiviral vectors offer direct delivery of DNA/RNA molecules to host genome and facilitate permanent gene integration, which is optimal for regenerative cell-based therapies. We discovered that transplanted HSPC-derived macrophage progenies supplied functional *CTNS* directly to diseased tissue sites (Harrison et al., 2013). Remarkably, widespread disease rescue was additionally noted in the form of reduced intralysosomal cystine levels and widespread tissue morphological rescue lasting the entirety of cystinotic mouse lifespan (Harrison et al., 2013; Rocca et al., 2013).

Given therapeutic success of *in vivo* HSPC-mediated intracellular delivery of lysosomal compartments (Harrison et al., 2013; Naphade et al., 2015), the Cherqui group received FDA-approval to initiate Phase I/II clinical trials conducted by Dr. Stephanie Cherqui of the UCSD School of Medicine Pediatrics Department, with collaborators California Institute for Regenerative Medicine (CIRM) and the Cystinosis Research Foundation (ClinicalTrials.gov Identifier: NCT03897361), which began in July of 2019. Endogenous patient HSPCs undergo genomic remodeling *ex vivo* using a SIN-lentiviral vector, pCCL-CTNS (Cherqui 2019; Canté-Barrett et al., 2016). After patient HSPCs are transduced with functional *CTNS* gene, stem cells are subsequently transplanted back into the myeloablated patients, evading engraftment risks arising from stem cell donor matching for allogeneic transplants (ClinicalTrials.gov Identifier: NCT03897361). If the mouse model is an accurate prediction, following engraftment of transplanted HSPCs in the bone marrow, we expect HSPCs to differentiate into macrophages that supply functional cystinosin protein to diseased tissues, ultimately inducing long-term multisystemic disease rescue (ClinicalTrials.gov Identifier: NCT03897361).

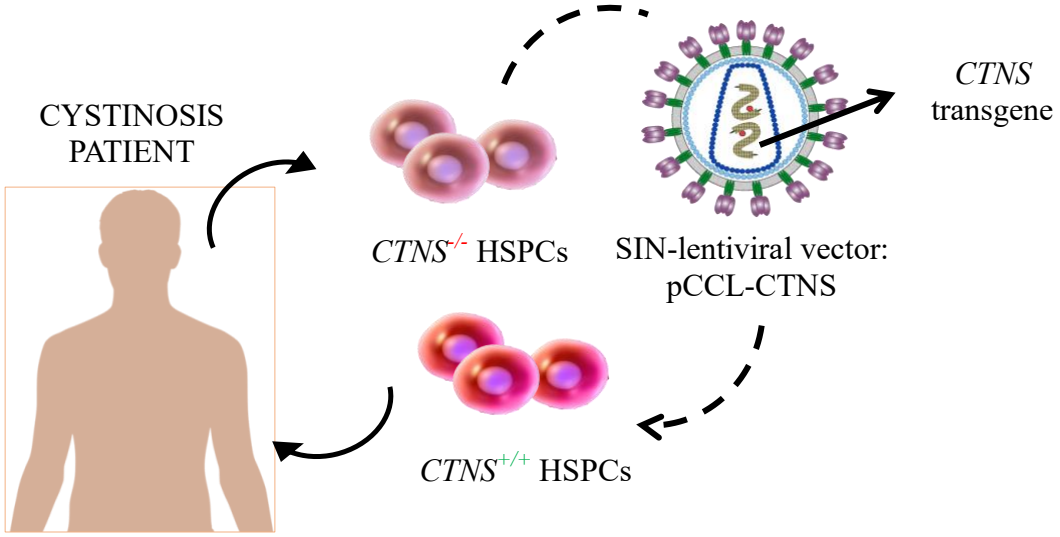

Figure 1.2: Schematic of Phase I/II human cystinosis trials. Patient cells are gene-corrected via lentiviral delivery of *CTNS* gene *ex vivo* and transplanted back into respective myeloablated patients. Patients will then be carefully monitored for disease recovery.

1.5.1: Mechanism of Action of HSPC-derived Macrophage-Mediated TNT Delivery. The last step in investigating the advent of HSPC gene therapy for cystinosis was to elucidate the mechanism of functional protein delivery. The Cherqui lab discovered that engrafted HSPCs gave rise to tissue-resident macrophages capable of extending membranous protrusions known as tunneling nanotubules (TNTs) to diseased cells (Naphade et al., 2015). TNTs are membranous protrusions that facilitate long-distance communication, exchange, and transport of materials between different cell types (Dupont et al., 2018). TNT cell-to-cell pathways facilitated the bidirectional transfer of functional cystinosin protein to *Ctns*$^{-/-}$ cells of the thyroid and kidney (Rocca and Cherqui 2019; Harrison et al., 2013). This project was the first to report this macrophage-mediated TNT delivery of functional protein underlying the mechanisms involved in cystinosis cross correction (Naphade et al., 2015).

HSPC-mediated intracellular trafficking occurs through the inducible dynamic plasticity of monocytic macrophages driving innate immunity (Das et al., 2015). Macrophages modulate induction and suppression of inflammation in response to environmental factors via differentiation into dichotomic phenotypes: pro-inflammatory type 1 macrophage (M1) and anti-inflammatory type 2 macrophage (M2) (Das et al., 2015). Although *in vitro* macrophage phenotypic oversimplification does not account for the dynamic environmental factors governing *in vivo* macrophage complexity (Murray et al., 2014; Martinez et al., 2014), both systems have been useful in elucidating mechanisms for cystinosis cross correction (Goodman et al., 2019). That said, while macrophage morphology affects polarization (McWhorter et al., 2013), it is unknown whether inflammatory plasticity impacts TNT development for HSPC gene therapy.

1.5.2: Project Design I. In chapter 1 of this thesis, we investigated the effects of macrophage polarization on disease rescue via TNT development and trafficking within i*n vitro* and *in vivo* systems. We demonstrated that pro-inflammatory M1-like stimulation suppresses macrophage-mediated TNT formation and intracellular trafficking of cystinosin-bearing lysosomes from WT IC21 peritoneal macrophages to *Ctns*$^{-/-}$ fibroblasts *in vitro* (Goodman et al., 2019). Alternatively, *in vivo* experiments of WT HSPC transplantation into *Ctns*$^{-/-}$ mice resulted in enrichment of pro-inflammatory M1-like macrophages localized

to diseased kidney, leading tissue preservation as indicated by restored *Ctns* mRNA expression and reduced cystine levels (Goodman et al., 2019). Curiously, increased macrophage-derived thicker TNT formation and trafficking activity seen in unstimulated cystinotic co-cultures effectively models *in vivo* observations of enhanced macrophage recruitment and intercellular lysosomal delivery after HSPC transplantation (Naphade et al., 2015). Since the exact mechanism of macrophage mobilization to diseased tissue is unknown, the oversimplification of in vitro systems lacking holistic environmental signaling factors can explain the discrepancy between effects of M1 polarization on *in vitro* and *in vivo* cystinosis models (Goodman et al., 2019). Regardless, these data implicate the modulation of macrophage polarization (with emphasis on M1-like activity) as an integral component to enhancing the therapeutic efficacy of our novel HSPC transplantation remedial mechanism. Ultimately, a detailed understanding of these processes could ultimately better explain and enhance the effective delivery of non-secreted genetic products.

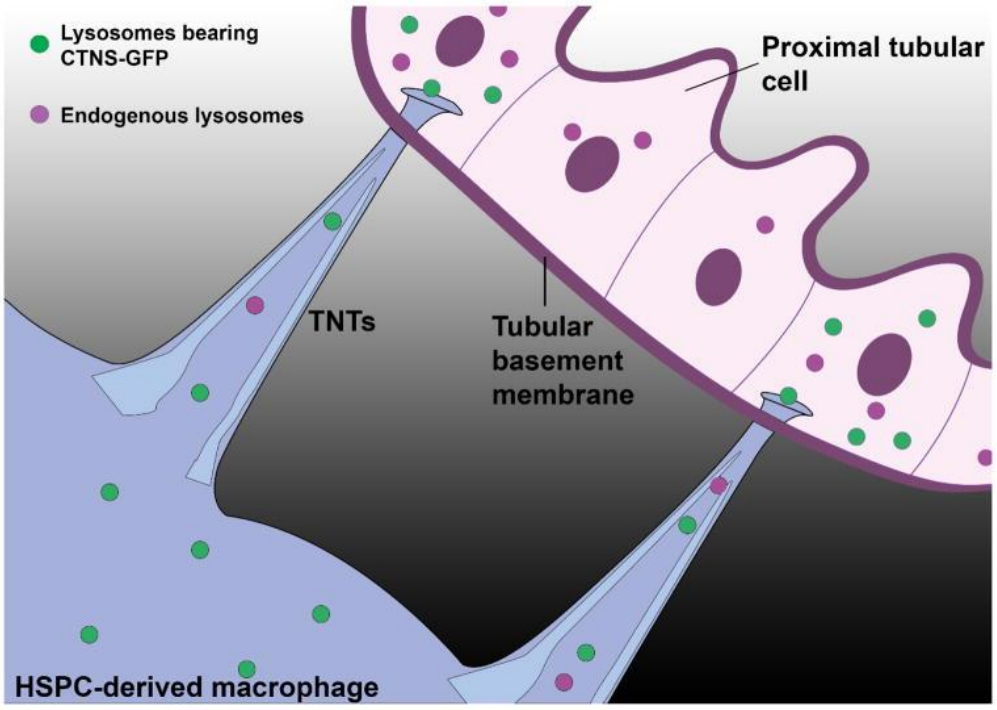

Figure 1.4: Schematic of WT HSPC transplantation mechanism. Illustration of *in vivo* TNT mechanism of functional CTNS-GFP transfer to diseased proximal tubular cell. Adapted from Rocca and Cherqui 2019.

1.6.1: Sedoheptulokinase Relevance to Cystinosis. Sedoheptulokinase (*SHPK*), also known as carbohydrate-like kinase (*CARKL*), is metabolic regulatory enzyme found in the non-oxidative arm of the pentose phosphate pathway (PPP) that supplies carbon substrates for glycolysis (Nagy and Hashemi 2013). In the most common mutation of cystinosis, a 57 kilo-base pair homozygous deletion removes the *CTNS* gene, as well as neighboring *SHPK* and *TRPV-1* genes (Buntix et al., 2016); this mutation prevents *TRPV-1*-mediated pain and heat sensitivity and causes *SHPK*-deficiency (SHPKD) in patients (Wamelink et al., 2008). *SHPK* mRNA expression is commonly localized to tissues with high biochemical activity, such as liver, kidney, pancreas, and heart (Wamelink et al., 2008). The translated ~51 kilo-Dalton enzymatic protein *SHPK* co-localizes with glucose-6-phosphate (G6P) dehydrogenase in the cytoplasm (Nagy and Hashemi 2013). *SHPK* metabolizes the conversion of a biomolecule found in fruits called sedoheptulose into sedoheptulose-7-phosphate (S7P), a key intermediate directly regulating carbon effluxes in primary glucose metabolism (Wamelink et al., 2008).

Downstream metabolic consequences of SHPKD include elevated S7P concentrations in urine and bloodspots, as well as increased levels of urinary erythritol, a reduced product derived from S7P and G3P transaldolase-conversion (Kardon et al., 2008). SHPKD metabolic perturbations were exclusively found in patients with cystinosis carrying homozygous SHPK elimination in the 57-kb deletion (Wamelink et al., 2015); the exact mechanism for these molecular events remain unknown. To further explore correlations between enzymatic activity of sedoheptulokinase and PPP metabolism in immune cells, modified *SHPK* expression was induced in RAW264.7 macrophages (Haschemi et al., 2012). *SHPK* overexpression in RAW264.7 macrophages caused increased in PPP metabolites G3P, X5P, and R5P abundance, while S7P was significantly reduced; conversely, *SHPK* knocked-down cells showed decreased PPP intermediate abundance, with no particular changes in S7P levels (Haschemi et al., 2012). Thus, metabolic dysregulation as a consequence of homozygous disruption in *SHPK* expression indicates the need to evaluate the clinical relevance of *SHPK* to the metabolic pathogenic presentation of cystinosis.

In addition to the metabolic phenotype, *SHPK* has also been identified as a critical regulator of macrophage polarization (Haschemi et al., 2012). RAW264.7 macrophages treated with immune stimulator liposaccharide (LPS) adopt a pro-inflammatory polarization phenotype, secreting associated cytokines such as tumor necrosis factor alpha (TNF-a), interleukin 6 (IL-6), and interleukin 1-beta (IL1-b) that promote inflammation to compromised sites (Artri et al., 2018). LPS-induced activation towards M1 polarization of RAW264.7 macrophages induced *SHPK* mRNA repression; reciprocally, macrophages overexpressing *SHPK* repressed LPS-stimulated M1 polarization (Haschemi et al., 2012). Coupling the knowledge of the inverse relationship between *SHPK* expression and pro-inflammatory M1 macrophage polarization (Haschemi et al., 2012) with the gene therapy mechanism of HSPC-derived M1-like macrophages as an intracellular transport mechanism (Goodman et al., 2019), it becomes apparent that the stem cell gene therapy may not extend to 60% of patients harboring compromised *SHPK* induced by the 57-kb deletion in the cystinosis clinical trials. Thus, we aim to characterize the consequences of *SHPK*-deficiency on the efficacy of HSPC-derived macrophage intracellular trafficking following transplantation into cystinotic mice to elucidate if patients carrying the homozygous 57-kb deletion inducing *SHPK*-deficiency will still benefit from the macrophage-mediated gene therapy. Before this study was conducted, these patients could not be enrolled in the current clinical trial.

1.6.2: Project Design II. In chapter 2 of this thesis, we sought to investigate the impact of *SHPK* in the progression of cystinosis and on the therapeutic efficacy of HSPC gene therapy. In this pursuit, we generated and characterized novel *Shpk*-deficient mouse models with normal *Ctns* function (*Shpk*$^{-/-}$/*Ctns*$^{+/+}$) to trace potential metabolic phenotypes caused by induced *Shpk* genomic dysfunction. We then evaluated the therapeutic efficacy of *Shpk*-deficient (*Shpk*$^{-/-}$/*Ctns*$^{+/+}$) HSPC transplantation isolated from the *Shpk*$^{-/-}$ mice into cystinotic (*Ctns*$^{-/-}$/*Shpk*$^{+/+}$) mice; this stem cell therapy model mimics the genotypes of gene-corrected HSPCs transplanted into patients harboring the 57-kb deletion with mutated *SHPK* for projected clinical trials. We generated the first *Shpk* knockout mice models, *Shpk*$^{\Delta ATG}$ and *Shpk*$^{\Delta E2}$, harboring CRISPR-Cas9 genomic deletions at two different loci of the gene. Characterization of these mice demonstrated that

Shpk-deficiency contributes to a mild metabolic phenotype in cystinosis in the form of PPP metabolite perturbation. Following transplantation of *Shpk*$^{-/-}$ HSPCs into lethally irradiated *Ctns*$^{-/-}$ mice, we found effective restoration of *Ctns* mRNA expression and reduction of cystine levels across multiple *Ctns*$^{-/-}$ tissues as compared to *Ctns*$^{-/-}$ HSPC and non-transplanted controls. Therefore, *SHPK*-deficient (with functional CTNS) HSPC transplantation may still provide therapeutic benefit to all patients, regardless of *SHPK* genotype. Our studies sanctioned the enrollment of patients carrying the 57-kb-deletion at the homozygote state in the gene-corrected stem cell transplantation for cystinosis, and expanded the therapeutic application of stem cell gene therapies for cystinosis and other similar disorders.

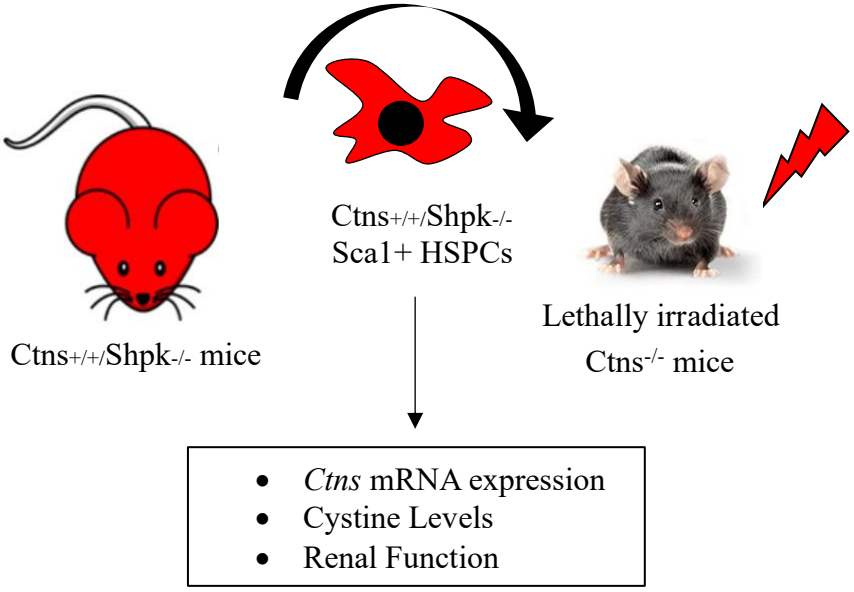

Figure 1.4: Schematic of Shpk*$^{-/-}$ *HSPC transplantation for cystinosis gene therapy evaluation. Isolated *Shpk*$^{-/-}$ Sca1+ HSPCs were transplanted into lethally-irradiated cystinotic mice and evaluated for improvements in *Ctns* mRNA levels, cystine content, and renal function.

1.7: Acknowledgements

Chapter 1, in part, is currently being prepared for submission for publication of the material, *Goodman S., **Khan M.**, Sharma J., Cano J., Zi, L., Estrada, V., Gertsman, I., Cherqui, S. "Shpk-deficient hematopoietic stem cell therapy remains effective to rescue cystinosis."* The master's thesis author was a key investigator and author of this paper.

1.8: References

Ariceta, G., Giordano, V., & Santos, F. (2019). Effects of long-term cysteamine treatment in patients with cystinosis. *Pediatric Nephrology*, *34*(4), 571–578. https://doi.org/10.1007/s00467-017-3856-4

Atri, C., Guerfali, F. Z., & Laouini, D. (2018). Role of human macrophage polarization in inflammation during infectious diseases. *International Journal of Molecular Sciences*, *19*(6). https://doi.org/10.3390/ijms19061801

Bäumner, S., & Weber, L. T. (2018). Nephropathic cystinosis: Symptoms, treatment, and perspectives of a systemic disease. *Frontiers in Pediatrics*, *6*(March), 1–8. https://doi.org/10.3389/fped.2018.00058

Biffi, A. (2017). Hematopoietic Stem Cell Gene Therapy for Storage Disease: Current and New Indications. *Molecular Therapy*, *25*(5), 1155–1162. https://doi.org/10.1016/j.ymthe.2017.03.025

Buntinx, L., Voets, T., Morlion, B., Vangeel, L., Janssen, M., Cornelissen, E., Vriens, J., De Hoon, J., & Levtchenko, E. (2016). TRPV1 dysfunction in cystinosis patients harboring the homozygous 57 kb deletion. *Scientific Reports*, *6*(September), 1–9. https://doi.org/10.1038/srep35395

Canté-Barrett, K., Mendes, R. D., Smits, W. K., Van Helsdingen-Van Wijk, Y. M., Pieters, R., & Meijerink, J. P. P. (2016). Lentiviral gene transfer into human and murine hematopoietic stem cells: Size matters. *BMC Research Notes*, *9*(1), 1–6. https://doi.org/10.1186/s13104-016-2118-z

Cherqui, S. (2014). Is genetic rescue of cystinosis an achievable treatment goal? *Nephrology Dialysis Transplantation*, *29*(3), 522–528. https://doi.org/10.1093/ndt/gft270

Cherqui, S., Sevin, C., Hamard, G., Kalatzis, V., Sich, M., Pequignot, M. O., Gogat, K., Abitbol, M., Broyer, M., Gubler, M.-C., & Antignac, C. (2002). Intralysosomal Cystine Accumulation in Mice Lacking Cystinosin, the Protein Defective in Cystinosis. *Molecular and Cellular Biology*, *22*(21), 7622–7632. https://doi.org/10.1128/mcb.22.21.7622-7632.2002

Cohen, C., Charbit, M., Chadefaux-Vekemans, B., Giral, M., Garrigue, V., Kessler, M., Antoine, C., Snanoudj, R., Niaudet, P., Kreis, H., Legendre, C., & Servais, A. (2015). Excellent long-term outcome of renal transplantation in cystinosis patients. *Orphanet Journal of Rare Diseases*, *10*(1), 4–11. https://doi.org/10.1186/s13023-015-0307-9

Das, A., Sinha, M., Datta, S., Abas, M., Chaffee, S., Sen, C. K., & Roy, S. (2015). Monocyte and Macrophage Plasticity in Tissue Repair and Regeneration. *American Journal of Pathology*, *185*(10), 2596–2606. https://doi.org/10.1016/j.ajpath.2015.06.001

Dupont, M., Souriant, S., Lugo-Villarino, G., Maridonneau-Parini, I., & Vérollet, C. (2018). Tunneling nanotubes: Intimate communication between myeloid cells. *Frontiers in Immunology*, *9*(JAN), 1–6. https://doi.org/10.3389/fimmu.2018.00043

Elmonem, M. A., Veys, K. R., Soliman, N. A., Van Dyck, M., Van Den Heuvel, L. P., & Levtchenko, E. (2016). Cystinosis: A review. *Orphanet Journal of Rare Diseases*, *11*(1), 1–17. https://doi.org/10.1186/s13023-016-0426-y

Emma, F., Nesterova, G., Langman, C., Labbé, A., Cherqui, S., Goodyer, P., Janssen, M. C., Greco, M., Topaloglu, R., Elenberg, E., Dohil, R., Trauner, D., Antignac, C., Cochat, P., Kaskel, F., Servais, A., Wühl, E., Niaudet, P., Van't Hoff, W., … Levtchenko, E. (2014). Nephropathic cystinosis: An international consensus document. *Nephrology Dialysis Transplantation*, *29*, iv87–iv94. https://doi.org/10.1093/ndt/gfu090

Gaide Chevronnay, H. P., Janssens, V., Van Der Smissen, P., N'Kuli, F., Nevo, N., Guiot, Y., Levtchenko, E., Marbaix, E., Pierreux, C. E., Cherqui, S., Antignac, C., & Courtoy, P. J. (2014). Time course of pathogenic and adaptation mechanisms in cystinotic mouse kidneys. *Journal of the American Society of Nephrology*, *25*(6), 1256–1269. https://doi.org/10.1681/ASN.2013060598

Goodman, S., Naphade, S., Khan, M., Sharma, J., & Cherqui, S. (2019). Macrophage polarization impacts tunneling nanotube formation and intercellular organelle trafficking. *Scientific Reports*, *9*(1). https://doi.org/10.1038/s41598-019-50971-x

Haschemi, A., Kosma, P., Gille, L., Evans, C. R., Burant, C. F., Starkl, P., Knapp, B., Haas, R., Schmid, J. A., Jandl, C., Amir, S., Lubec, G., Park, J., Esterbauer, H., Bilban, M., Brizuela, L., Pospisilik, J. A., Otterbein, L. E., & Wagner, O. (2012). The sedoheptulose kinase CARKL directs macrophage polarization through control of glucose metabolism. *Cell Metabolism*. https://doi.org/10.1016/j.cmet.2012.04.023

Hasilik, A., Klein, U., Waheed, A., Strecker, G., & von Figura, K. (1980). Phosphorylated oligosaccharides in lysosomal enzymes: Identification of α-N-acetylglucosamine (1)phospho(6)mannose diester groups. *Proceedings of the National Academy of Sciences of the United States of America*, *77*(12 II), 7074–7078. https://doi.org/10.1073/pnas.77.12.7074

Harrison, F., Yeagy, B. A., Rocca, C. J., Kohn, D. B., Salomon, D. R., & Cherqui, S. (2013). Hematopoietic stem cell gene therapy for the multisystemic lysosomal storage disorder cystinosis. *Molecular Therapy*, *21*(2), 433–444. https://doi.org/10.1038/mt.2012.214

Kalatzis, V., Nevo, N., Cherqui, S., Gasnier, B., & Antignac, C. (2004). Molecular pathogenesis of cystinosis: Effect of CTNS mutations on the transport activity and subcellular localization of cystinosin. *Human Molecular Genetics*, *13*(13), 1361–1371. https://doi.org/10.1093/hmg/ddh152

Penati, R., Fumagalli, F., Calbi, V., Bernardo, M. E., & Aiuti, A. (2017). Gene therapy for lysosomal storage disorders: recent advances for metachromatic leukodystrophy and mucopolysaccaridosis I. *Journal of Inherited Metabolic Disease*, *40*(4), 543–554. https://doi.org/10.1007/s10545-017-0052-4

Pu, J., Guardia, C. M., Keren-Kaplan, T., & Bonifacino, J. S. (2016). Mechanisms and functions of lysosome positioning. *Journal of Cell Science*, *129*(23), 4329–4339. https://doi.org/10.1242/jcs.196287

Rastall, D. P. W., & Amalfitano, A. (2015). Recent advances in gene therapy for lysosomal storage disorders. *Application of Clinical Genetics*, *8*, 157–169. https://doi.org/10.2147/TACG.S57682

Rocca, C. J., & Cherqui, S. (2019). Potential use of stem cells as a therapy for cystinosis. *Pediatric Nephrology*, *34*(6), 965–973. https://doi.org/10.1007/s00467-018-3974-7

Syres, K., Harrison, F., Tadlock, M., Jester, J. V., Simpson, J., Roy, S., Salomon, D. R., & Cherqui, S. (2009). Successful treatment of the murine model of cystinosis using bone marrow cell transplantation. *Blood*, *114*(12), 2542–2552. https://doi.org/10.1182/blood-2009-03-213934

Touchman, J. W., Anikster, Y., Dietrich, N. L., Braden Maduro, V. V., McDowell, G., Shotelersuk, V., Bouffard, G. G., Beckstrom-Sternberg, S. M., Gahl, W. A., & Green, E. D. (2000). The genomic region encompassing the nephropathic cystinosis gene (CTNS): Complete sequencing of a 200-kb segment and discovery of a novel gene within the common cystinosis-causing deletion. *Genome Research*, *10*(2), 165–173. https://doi.org/10.1101/gr.10.2.165

Thoene, J. G., Oshima, R. G., & Crawhall, J. C. (1976). Intracellular cystine depletion by aminothiols in vitro and in vivo. *Journal of Clinical Investigation*, *58*(1), 180–189. https://doi.org/10.1172/JCI108448

Wamelink, M. M. C., Ramos, R. J. J. F., van den Elzen, A. P. M., Ruijter, G. J. G., Bonte, R., Diogo, L., Garcia, P., Neves, N., Nota, B., Haschemi, A., Tavares de Almeida, I., & Salomons, G. S. (2015). First two unrelated cases of isolated sedoheptulokinase deficiency: A benign disorder? *Journal of Inherited Metabolic Disease*, *38*(5), 889–894. https://doi.org/10.1007/s10545-014-9809-1

Chapter 2: Macrophage Polarization Impacts TNT-mediated Intracellular Trafficking for Disease Therapy

The following section 2, in whole, is a reprint of material that appears in *Scientific Reports* on October 10, 2019.

2.1: Introduction

Intercellular communication is essential to maintain and potentially restore homeostasis in multicellular organisms. Tunneling nanotubes (TNTs) are one interaction pathway consisting of long actin-rich membranous extensions capable of forming cytosolic connections between distant cells (Ariazi et al., 2017; Rustom et al., 2004; Wang et al., 2010). TNTs have been observed in vitro and in vivo facilitating transfer of molecular cargos ranging from electrical signals to organelles to pathogens (Gousset et al., 2013; Chinnery et al., 2008; Gurke et. al., 2008). Mechanistic investigations of hematopoietic stem and progenitor cell (HSPC) transplantation therapy for the lysosomal storage disorder cystinosis revealed HSPC-derived macrophages deliver functional lysosomal protein cystinosin through TNTs to diseased tissue, resulting in lifelong prevention of disease progression in the mouse model (Naphade et al., 2015; Rocca et al., 2015; Gaide Chevronnay et al., 2016).

Cystinosin is ubiquitously expressed within the lysosomal membrane to export cystine into the cytosol (Kalatzis et al., 2001). However, loss-of-function mutations in the *CTNS* gene cause lysosomal cystine accumulation and crystallization leading to multi-organ failure (Emma et al., 2014; Cherqui et al., 2002). Current therapies merely ameliorate symptoms and delay disease progression (Medic et al., 2017). Our group has pioneered the use of HSPC transplantation as a promising new therapy for cystinosis with translation of this approach into an autologous gene-corrected HSPC transplantation clinical trial for human cystinosis patients underway (Syres et al., 2009; Yeagy et al., 2011; Harrison et al., 2013).

Due to cystinosin being a non-secreted transmembrane protein, the ubiquitous prevention of pathogenic cell damage using HSPCs was unexpected until the mechanism of trafficking was shown to involve TNT-mediated delivery of healthy lysosomes from HSPC-derived macrophages to diseased tissue (Naphade et al., 2015). While many studies have demonstrated how pathogens like HIV (Eugenin et al.,

2009) or malignancies like gliomas (Osswald et al., 2016) can hijack TNTs, the structures also present an intriguing potential delivery system of therapeutic proteins to treat genetic diseases (Bruzauskaite et al., 2016). Following HSPC transplantation, kidney macrophages formed TNTs that crossed the basement membrane and rescued proximal tubule cells by delivering cystinosin-bearing lysosomes (Naphade et al., 2015). The same mechanism has also been observed in the cornea and thyroid of transplanted cystinotic mice (Rocca et al., 2015; Gaide Chevronnay et al., 2016), as well as in the X-linked tubulopathy Dent disease (Gabriel et al., 2017). In addition, studies of HSPC transplantation as treatment for the mitochondrial neurodegenerative disorder Friedreich's Ataxia reveal microglial correction of neurons, potentially through TNTs (Rocca et al., 2017). Taken together, these data indicate a prolific ability of phagocytic cells to widely disseminate therapeutic molecules via TNT trafficking.

The plasticity of macrophages allows them to fulfill numerous biological functions ranging from proinflammatory roles in both arms of the immune system to immunomodulatory activities vis-à-vis tissue repair, homeostasis and resolution of inflammation. Traditionally, these distinct phenotypic behaviors have been classified as either proinflammatory mediators of a type I immune response (M1 or classical activation) versus. immunomodulatory tissue-remodelers (M2 or alternative) (Mills et al., 2000; Ying et al., 2013). However, this model risks oversimplification of a seamless phenotypic spectrum into a false dichotomy masking in vivo macrophage complexity, where these subtypes are dynamically changing in response to the cues received from the microenvironment, and thus never cleanly delineated (Murray et al., 2014; Martinez et al., 2014).

In the current study, we investigated macrophage-mediated TNT formation and intercellular trafficking. Using novel image analysis platforms, we report that in vitro proinflammatory macrophage stimulation suppressed both TNT-like protrusion formation as well as intercellular organelle trafficking. In contrast, macrophages co-cultured with diseased *Ctns*$^{-/-}$ fibroblasts exhibited increased lysosomal and mitochondrial intercellular trafficking along with more frequent formation of larger protrusions. These data suggest that diseased cells stimulate TNT formation towards a thicker phenotype, which has been shown to more effectively transport organelles such as macrophages and intracellular vesicles (Onfelt et al., 2006).

Unexpectedly, in vivo enrichment of proinflammatory macrophages showed similar disease rescue following *Rac2*$^{-/-}$ HSPC transplantation in *Ctns*$^{-/-}$ mice compared to wild-type (WT) mice. This discrepancy between mice and co-cultures highlights the well-known dangers of relying solely on in vitro polarization models where cytokine stimulation pushes macrophages to non-physiological polarization phenotypes. That said, increased macrophage-derived thicker TNT formation and trafficking activity seen in unstimulated cystinotic co-cultures effectively models in vivo observations of enhanced macrophage recruitment and intercellular lysosomal delivery after HSPC transplantation (Naphade et al., 2015). Using both cells and transplanted mice, we can therefore probe aspects of TNTs induced when stress on a separate cellular population is stimulating macrophage TNT formation in a paracrine fashion. Ultimately, a detailed understanding of these processes could ultimately better explain and enhance the effective delivery of non-secreted genetic products.

2.2: Results

Macrophage membrane protrusions are suppressed by proinflammatory stimulation but enhanced by co-culture with diseased cells. Previous work has uncovered that proinflammatory bone marrow derived macrophages (BMDMs) display a more rounded ameboid morphology compared to unstimulated or anti-inflammatory cells (McWhorter et al., 2013). To investigate tunneling nanotube (TNT) formation in this context, we treated primary murine BMDMs and the immortalized IC-21 peritoneal macrophage cell line with either LPS/IFNγ, directing differentiation towards proinflammatory M1-like cells, M(LPS/IFNγ), or with IL-4/IL-10 for differentiation towards immunomodulatory M2-like macrophages, M(IL-4/IL-10). Using a variety of assays to characterize expression of well-established macrophage polarization markers, we rigorously validated our in vitro polarization experimental system. First, we analyzed differentially expressed mRNAs and proteins, observing increased expression of numerous proinflammatory markers such as inducible nitric oxide synthase (iNos), interleukin-6 (Il-6) and interleukin-1β (Il-1β) following LPS/IFNγ treatment, as well as upregulation of anti-inflammatory markers such as Cd206, Ym1 and Fizz1 after IL-4/IL-10 stimulation (Fig. 2.1a,b; Supplementary File 1, Fig. S1) (Wang et al., 2014; Tatano et al., 2014). Furthermore, M(IL-4/IL-10) displayed greater enzymatic activity of arginase-1 (ARG1), an important biosynthetic regulator of tissue repair, while M(LPS/IFNγ) increased extracellular secretion of monocyte chemoattractant protein 1 (MCP1) (Fig. 2.1c,d), a potent proinflammatory chemokine that regulates migration and infiltration of macrophages (Van den Bossche et al., 2012). Finally, polarized BMDMs were analyzed by flow cytometry where we observed expected changes in expression of proinflammatory markers CD80 and CD126 or anti-inflammatory CD206 (Fig. 2.1e) (Van de Bossche et al., 2012). To assess macrophage viability following polarization, we also measured cell proliferation using WST-1, which decreased following LPS/IFNγ but not IL-4/IL-10 stimulation in both BMDMs ($P = 0.0015$) and IC-21 macrophages ($P < 0.0001$) compared to non-treated controls (Fig. 2.1f). In contrast, apoptosis measured by Annexin V and Propidium Iodide-stained cells did not vary between treatment groups (data

not shown). Taken together, in vitro treatment yields the anticipated changes in marker expression at both the mRNA and protein levels, confirming that our system replicates the expected polarization findings.

Upon imaging of treated cells, we also observed the expected shift of M(LPS/IFNγ) morphology to a more rounded phenotype in both BMDMs and IC-21 (Fig. 2.1g). We developed an image analysis workflow using ImagePro Premier to automatically detect and quantify fluorescent membrane protrusions using customizable morphological filtration based on characteristics such as length, width and circularity (Supplementary File 1, Fig. S2). By analyzing larger stitched images acquired using the wide-field Keyence fluorescence microscope, our high-throughput method enables automated, rapid and unbiased analysis of fluorescent cellular protrusions from dozens to hundreds of cells at once. Using this algorithm, we observed a significant reduction of approximately 50% in the protrusion frequency of BMDMs and IC-21 macrophages following LPS/IFNγ stimulation compared to non-treated macrophages ($P < 0.001$) (Fig. 2.1h). In contrast, M(IL-4/IL-10) BMDM protrusion frequency was statistically indistinguishable from control, while IC-21 displayed a modest decrease.

We sought to extend on our protrusion frequency findings by stimulating BMDMs with each cytokine or stimulant individually. We observe that either LPS or IFNγ by themselves are equally effective as when combined to reduce protrusion formation compared to untreated or M(IL-4/IL-10) (Supplementary File 1, Fig. S3). Furthermore, just as M(IL-4/IL-10) BMDMs, we again detected no difference in protrusion frequency for either M(IL-4) or M(IL-10) BMDM relative to untreated controls. Recent evidence suggests that tuberculosis infection triggers an increase in M(IL-10) macrophage TNT formation, but direct stimulation of BMDMs with IL-10 does not seem to recapitulate this phenotype (Souriant et al., 2019).

We previously reported that co-culture of IC-21 macrophages with murine cystinotic fibroblasts appeared to increase the formation of TNTs (Naphade et al., 2015). We replicated these experiments using our new automated imaging system and observed an increase in membrane protrusion formation in IC-21 macrophages co-cultured with diseased murine Ctns$^{-/-}$ fibroblasts compared to wildtype fibroblasts ($P = 0.007$) (Fig. 2.1i). Proinflammatory stimulation of these co-cultures yielded a reduction in macrophage-derived protrusion formation with no obvious morphological changes in fibroblasts (Fig. 2.1j), confirming

our previous data (Fig. 2.1h). Taken together, these data indicate proinflammatory M(LPS/IFNγ) macrophages generate fewer membrane protrusions than the immunomodulatory M(IL-4/IL-10) cells, and that diseased cystinotic cells enhanced protrusion formation in macrophages upon co-culture.

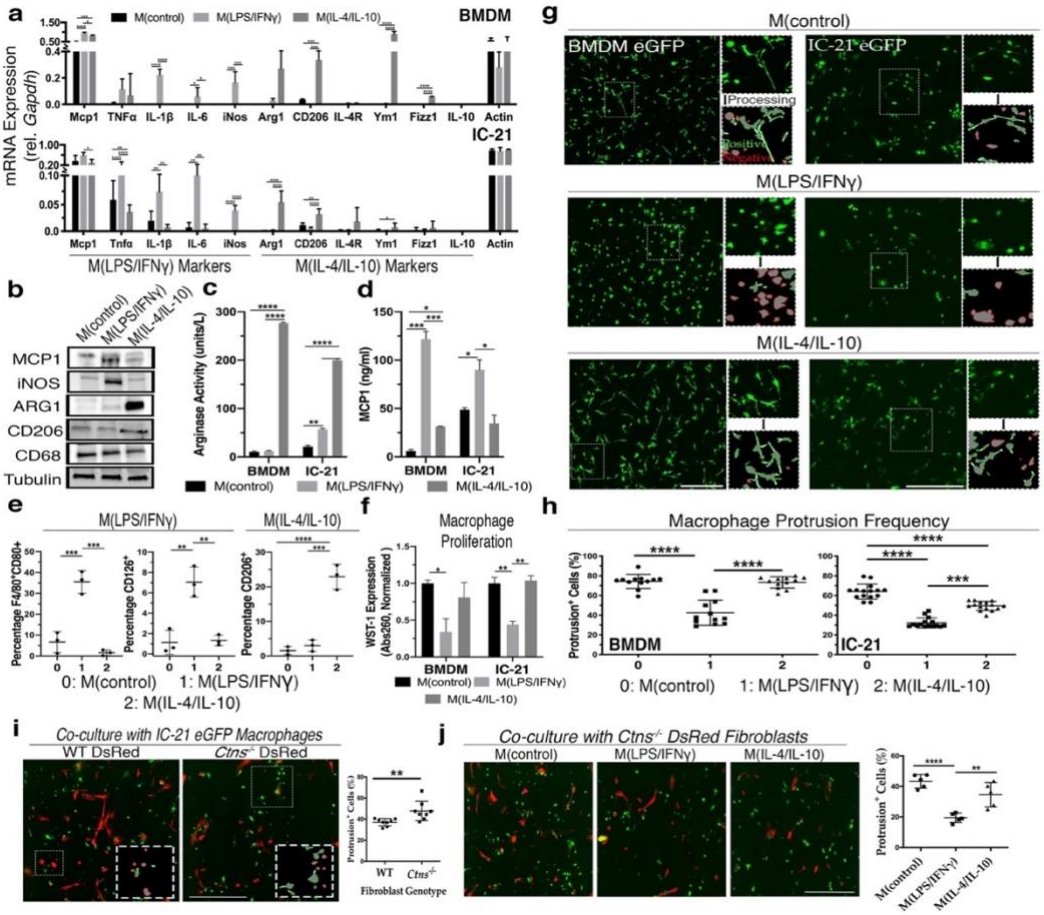

Figure 2.1: LPS/IFNγ polarization suppresses protrusion formation in BMDMs and IC-21 macrophages. (a) Bar graph representing mRNA expression of M(LPS/IFNγ) and M(IL4/IL10) markers relative to housekeeping control Gapdh in BMDMs and IC-21 macrophages after 48-hour pro- and anti-inflammatory macrophage polarization compared to non-treated cells (n = 5). (b) Representative immunoblots depicting polarization-associated signature protein expression in pro- and anti-inflammatory IC-21 macrophages and untreated controls. MCP1 and iNOS are M(LPS/IFNγ) markers, while ARG1 and CD206 are M(IL-4/IL-10) markers. CD68 is a pan-macrophage marker, and tubulin serves as the loading control (n = 2–4). (c) Graph depicts normalized colorimetric measurements of the M(IL-4/IL-10) marker ARG1 enzymatic activity from cell lysate following independent polarization treatments (n = 3). (d) Bar graph depicting normalized MCP1 cytokine secretion into media following polarization as measured by ELISA (n = 3). (e) Bar graphs representing flow cytometry analysis showing frequency of expression of M(LPS/IFNγ) markers CD80 and CD126 or M(IL-4/IL-10) marker CD206 following BMDM polarization (n = 3). (f) Bar graphs presenting normalized colorimetric absorbance values measuring cell proliferation using WST-1 cell proliferation reagent in BMDMs and IC-21 macrophages acquired three days post polarization treatment (n = 3). (g) Representative wide-field fluorescent images of control vs. M(LPS/IFNγ)- or M(IL4/IL10)-polarized BMDMs and IC-21 macrophages. Larger micrographs are stitched images of 5 × 5 individual tile. Zoomed inserts demonstrate automated image processing selecting for protrusion-positive (green) or negative (red) cells. See Supplementary File 2, Fig. S1 for method description and examples. (h) Percentile quantification of protrusion-positive cells in polarized BMDMs and IC-21 macrophages. Each data point in the box-and-whisker histogram is one stitched region with five regions analyzed per experiment (n = 3). (i) Representative fluorescent images of eGFP+ IC-21 co-cultures grown for three days with either WT (left) or Ctns−/− (right) DsRed+ fibroblasts. Boxed insert shows automated protrusion detection analysis with percentage of eGFP+ protrusion-positive cells shown in histogram (n = 3). (j) Representative fluorescent images of polarized eGFP+ IC-21 macrophage and Ctns−/− DsRed+ fibroblast co-cultures. Histogram illustrates percentage of control or M(LPS/IFNγ) and M(IL4/IL10) macrophages with protrusions (n = 3). All scale bars: 500 μM. All bar graphs shown as mean ± standard deviation (SD). P values were determined by either one-way ANOVA or student's t-tests. *P < 0.05, **P < 0.01, ***P < 0.001, ****P < 0.0001.

Macrophage-derived membrane protrusions resemble tunneling nanotubes. As no TNT-specific markers have been identified, we investigated the identity of macrophage-derived membrane protrusions based primarily on their morphology; TNTs are long, highly dynamic actin-rich tubes extending out from the plasma membrane without contacting the underlying substratum (Souriant et al., 2019; Sowinski et al., 2011). Cytoskeletal immunostaining of macrophage co-cultures revealed that all protrusions were actin-rich, while some also contained a tubulin core (Fig. 2.2a), a unique feature of thicker TNTs generated by macrophages mediating organelle transfer (Onfelt et al., 2006). Protrusions were visualized in three dimensions via high-resolution imaging of Z-stacks and generation of 3D-reconstructions using ImagePro (Fig. 2.2b, Supplementary Videos 2.1 and 2.2). Both BMDMs and IC21 macrophages were found to have eGFP-positive protrusions extending above the substratum. Termini of the eGFP protrusions were observed directly adjacent to DsRed fibroblast cell bodies potentially indicating membrane fusion and facilitation of TNT stabilization through intercellular membrane connections. In addition, we treated BMDMs co-cultured with *Ctns*$^{-/-}$ fibroblasts with cytochalasin B (cytoB), an actin destabilizing agent reported to prevent TNT formation and to inhibit organelle trafficking (Bukoreshtliey et al., 2009; Wang and Gerdes et al., 2015). Treatment with cytoB for 24 hours eliminated membrane protrusions from BMDMs with the extensions being restored several days following removal of cytoB (Fig. 2.2c).

In order to further characterize protrusions, we analyzed the shape and size of the automatically detected regions. We seeded and imaged equal numbers of eGFP BMDMs either alone or in co-culture with DsRed *Ctns*$^{-/-}$ fibroblasts. We first used our image analysis workflow to determine that co-cultures had a higher percentage of cells with protrusions than BMDMs alone ($P = 0.046$) (Fig. 2.2d). Using the automatically detected regions as guides, we blindly separated complete protrusions from the cell body, then used ImagePro to measure the resultant regions. From both conditions combined, we measured 242 individual protrusions and found that the mean protrusion area was 380.5 ± 145.4 μm2 and mean length was 45.00 ± 15.41 μm. As TNTs are extremely diverse, there is considerable variation on what "standard" dimensions between cell types (Austefiord et al., 2014). That said, most authors report an average TNT length between 17.7 μm (Jurkat T cells) and 44 μm (ARPE-19 retinal pigment epithelial cells), while the

longest protrusions can reach up to 120 μm, confirming our measurements are compatible with TNTs (Abounit and Zurzolo et al., 2012; Wittig et al., 2012). Unexpectedly, we also determined that protrusions generated from co-cultured macrophages were larger, longer and more elongated, meaning that they were less circular and had a larger ratio of the major to minor axis (Fig. 2.2e). These data not only confirm that a sizable fraction of protrusions appear to be of appropriate size to be considered TNTs but also highlights how the presence of diseased cystinotic cells affects protrusion morphology, as well as frequency. This is particularly interesting considering that previous work has shown that thicker macrophage TNTs preferentially transport organelles (Onfelt et al., 2006).

Finally, we analyzed expression of several genes involved in TNT formation following macrophage polarization to assess any differential expression of TNT-associated genes (Supplementary File 1, Fig. S4). In M(LPS/IFNγ) BMDMs, we observe increased mRNA expression of the MHC class II protein leukocyte specific transcript 1 (Lst1). In contrast, M(LPS/IFNγ) BMDMs displayed decreased expression of the Rho-family GTPase cell division control protein 42 homolog (Cdc42). We did not detect any changes in other TNT-linked genes such as M-Sec, a component of the exocyst complex that directly promotes TNT formation nor did we detect any changes in protein expression (data not shown) (Hase et al., 2009). Such changes in TNT marker expression after polarization are intriguing but thorough study of protein activity and localization would be required to uncover any mechanistic links between polarization and TNT formation. As such, in terms of protrusion characterization, a focus on structure, behavior and morphology is the more reliable method to indicate that a good fraction of the macrophage-derived protrusions automatically observed in our co-culture conditions represent bona fide TNTs.

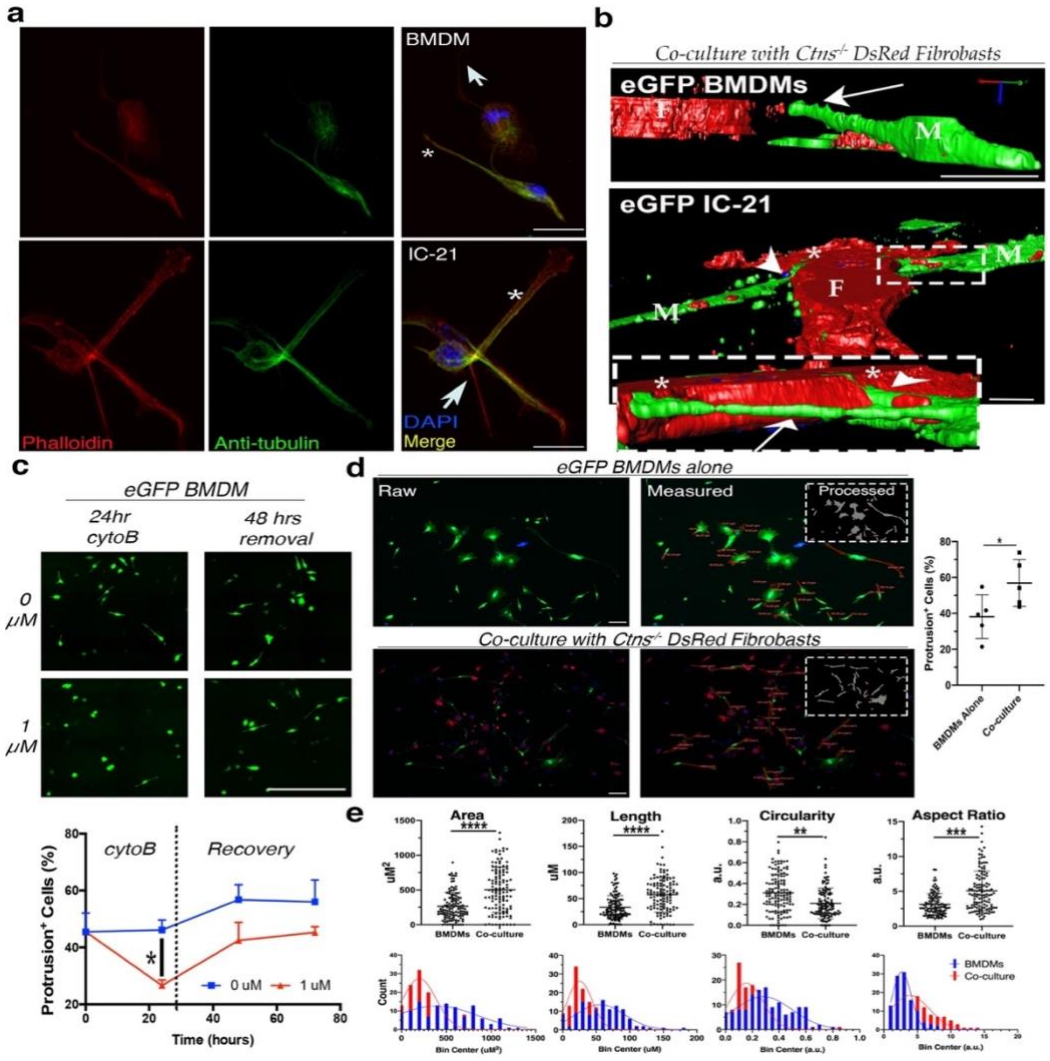

Figure 2.2: Some macrophage protrusions resemble TNT structure, behavior, and morphology. (a) Confocal micrographs of BMDMs and IC-21 cells after immunostaining for cytoskeletal components - actin (red) and tubulin (green). Thinner (arrows) and thicker (stars) protrusions indicated in both cell types. Scale bars: 10 μM. (b) 3D Z-stack reconstructions of eGFP+ BMDM or IC-21 cells (labeled M) co-cultured with Ctns−/− DsRed+ fibroblasts (labeled F). Boxed insert highlights protrusions extending above dish surface (arrows) and resting along the substratum (arrowhead). See Supplementary Videos 1 and 2. Scale bars: 10 μM. (c) Representative stitched micrographs depicting eGFP+ BMDMs following treatment and removal of cytochalsin B (cytoB) compared to untreated controls. XY graph shows percentage of protrusion-positive cells in each condition over time (n = 3 regions per treatment). Scale bar: 500 μM. (d) Representative raw confocal micrographs and measured images for eGFP BMDMs alone and in co-culture with Ctns−/− DsRed+ fibroblasts. Raw images were first processed for automated protrusion detection (insert) and the box-and-whisker plot (right) displays percentile quantification of protrusion-positive cells for BMDMs alone and in co-culture. Protrusion detection software rarely captures complete shape, so results were used as a guide in order to blindly manually separate protrusions from cell bodies by cutting along the estimation of normal membrane curvature. ImagePro was then used to measure protrusions; area measurements shown on top image and length on bottom. Scale bar: 100 μM. (e) Box-and-whisker plot (top) and frequency histogram (bottom) depicting area, length, circularity and aspect ratio protrusion measurements for BMDMs alone vs. in co-culture. Circularity is calculated as the ratio of the object compared to a circle with diameter equal to object's maximum Feret diameter, and represented on a scale from 0–1.0, with 1.0 being a perfect circle. Aspect ratio is the ratio of the major and minor axis of an eclipse equivalent to the object, with a higher value meaning a more elongated object. Outliers identified and excluded by ROUT test. Curves fit to histograms by Gaussian linear regression. P values determined by one-way ANOVA or student's t-tests. *P < 0.05, **P < 0.01, ***P < 0.001, ****P < 0.0001.

Co-culture of macrophages with cystinotic cells increased not only lysosomal but mitochondrial intercellular transfer as well. To investigate the potential impact of macrophage polarization on TNT-mediated intercellular organelle trafficking, *Ctns*$^{-/-}$ and WT DsRed^{+} fibroblasts were co-cultured with IC-21 macrophages stably transduced with the fusion proteins cystinosin-eGFP or frataxin-eGFP, a mitochondrial iron chelator defective in Friedreich's ataxia (Busi et al., 2012). In vitro live imaging previously revealed transfer of cystinosin-eGFP-bearing lysosomes or frataxin-eGFP-bearing mitochondria from macrophages to diseased murine *Ctns*$^{-/-}$ or *Fxn*$^{-/-}$ fibroblasts, respectively (Naphade et al., 2015; Rocca et al., 2015). High-magnification 3D-reconstructions confirmed the presence of eGFP-positive organelles within the cytoplasm of DsRed^{+} fibroblasts, as demonstrated by 3D renderings and orthogonal projections (Supplementary File 1, Fig. S5a,b, Supplementary Videos 2.3 and 2.4). Lysosomal transfer was confirmed to occur through TNT-like structures (Supplementary File 1, Fig. 5c, Supplementary Video 2.5).

We quantified the efficiency of lysosomal and mitochondrial transfer from the macrophages to the fibroblasts using another image analysis algorithm similar to the one we developed for TNT quantification, which measures the frequency of eGFP puncta ("donor") within a region of interest (ROI) defined by DsRed+ "recipient" cell (Supplementary File 1, Fig. S6). Co-cultures of 75,000 cystinosin-eGFP or frataxin-eGFP-expressing IC-21 macrophages and 50,000 DsRed+ WT or *Ctns*$^{-/-}$ fibroblasts were grown for three days and then fixed; fibroblasts cultured alone were used as controls (Fig. 2.3a). Fluorescent imaging revealed significantly higher numbers of both cystinosin-eGFP lysosomes ($P = 0.042$) and frataxin-eGFP mitochondria ($P = 0.019$) in *Ctns*$^{-/-}$ fibroblasts compared to WT fibroblasts (Fig. 2.3b,c, Supplementary File 1, Fig. S6c). Further, we treated macrophages for co-culture experiments to determine if either macrophage subtype impacts the efficacy of intercellular trafficking. We observed a significantly decreased presence of cystinosin-eGFP-positive lysosomes within fibroblasts co-cultured with M(LPS/IFNγ) macrophages ($P = 0.045$) (Fig. 2.3d).

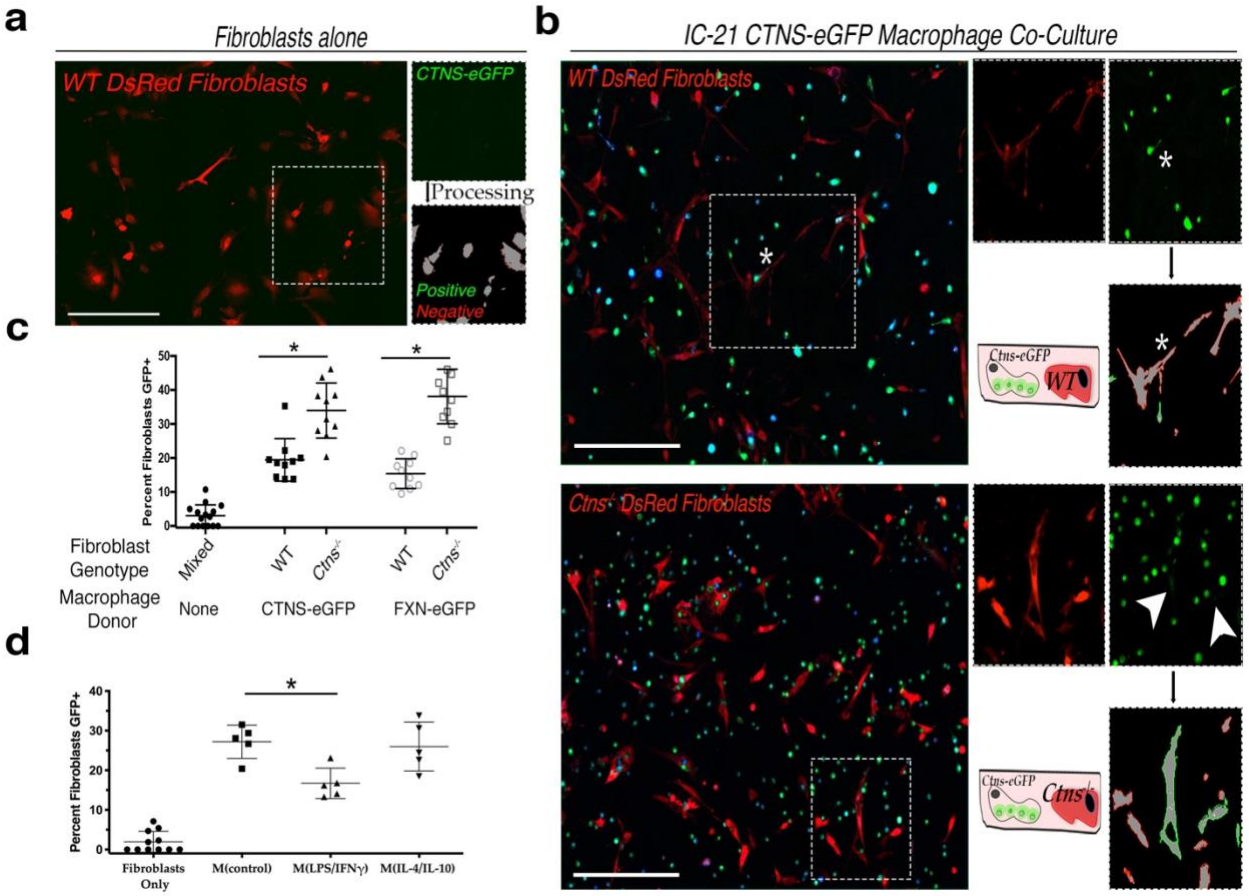

Figure 2.3: Intercellular trafficking of cystinosin-eGFP lysosomes and frataxin-eGFP mitochondria is increased to diseased Ctns−/− fibroblasts and diminished following proinflammatory polarization of co-cultured macrophages. (a) Representative stitched fluorescent micrograph of essential co-culture background control with only recipient DsRed+ fibroblasts. Boxed insert depicts automated image processing showing donor-positive (green) and donor-negative cells (red). See Supplementary File 2, Fig. S3 for automation methodology. (b) Representative fluorescent images of IC-21 cystinosin-eGFP co-cultures with either WT or Ctns−/− DsRed+ fibroblasts. Zoomed inserts highlight automated transfer quantification. Arrowheads indicate eGFP signal within DsRed+ fibroblasts. Stars indicate excluded signal due to cellular overlap. (c) Percentile quantitation of cystinosin- or frataxin-eGFP+ fibroblasts via automated image analysis. Each data point represents percent of donor-positive recipient cells in one stitched image ($n = 3$). All co-culture conditions have significantly more donor eGFP signal than background control with only fibroblasts ($P < 0.05$). (d) Frequency of cystinosin-eGFP trafficking in macrophage and fibroblast co-cultures following polarization with comparison to fibroblasts alone control. Histogram showing percentage of fibroblasts automatically determined positive for eGFP signal ($n = 5$). All scale bars are 500 µM. All graphs shown as mean ± SD. P values determined by one-way ANOVA or student's t-tests. *$P < 0.05$, **$P < 0.01$.

To corroborate our findings using another robust assay, we performed flow cytometry on co-cultures to analyze dual eGFP- and DsRed-positive cells; both cell types cultured alone were used as gating controls (Fig. 2.4a and Supplementary File 1, Fig. S7a). Consistent with our fluorescent imaging results, a significant increase of approximately 70–90% of the dual-positive population was observed in co-cultures of *Ctns*$^{-/-}$ fibroblasts with both cystinosin-eGFP ($P = 0.0168$) or frataxin-eGFP ($P = 0.0371$) macrophages as compared to WT fibroblast co-cultures (Fig. 2.4b). Another control of eGFP^{+} and DsRed^{+} cells mixed immediately prior to sorting did not yield dual-positive cells, indicating that prolonged co-culture is necessary to facilitate cellular interaction resulting in the generation of an eGFP^{+}DsRed^{+} population (Supplementary File 1, Fig. S7b). Furthermore, proinflammatory macrophage polarization also dramatically decreased the transfer of cystinosin-eGFP and frataxin-eGFP (Fig. 2.4c). Altogether, these data show that diseased cells enhance transfer of lysosomes and mitochondria from macrophages to the fibroblasts, while proinflammatory polarization inhibits this process.

HSPC-derived macrophages within the kidney of transplanted *Ctns*$^{-/-}$ mice appear to preferentially express M(LPS/IFNγ) markers. As in vitro polarization indicates that proinflammatory M(LPS/IFNγ) macrophages have impaired TNT formation and organelle transfer, we assessed the in vivo macrophage phenotype following HSPC transplantation in *Ctns*$^{-/-}$ mice. We transplanted WT eGFP HSPCs into *Ctns*$^{-/-}$ recipient mice via tail vein injection as previously described (Syres et al., 2009) and analyzed macrophage polarization markers by performing immunostaining on kidney sections (Supplementary File 1, Fig. S8). We observed robust colocalization between the eGFP^{+} HSPC progeny and the pan-macrophage marker CD68 (Supplementary File 1, Fig S8a). Unexpectedly, more abundant co-localization was detected between the stem cell progeny and markers for M(LPS/IFNγ) such as CD16/32 or MHCII, than with anti-inflammatory markers ARG1, CD206 or CD163 (Supplementary File 1, Fig. S8b). Antibodies were tested on other tissues such as tumors to ascertain positive immunoreactivity (Supplementary File 1, Fig. S8c). These data suggest that in vivo proinflammatory macrophages are responsible for tissue preservation after WT HSPC transplantation in cystinosis.

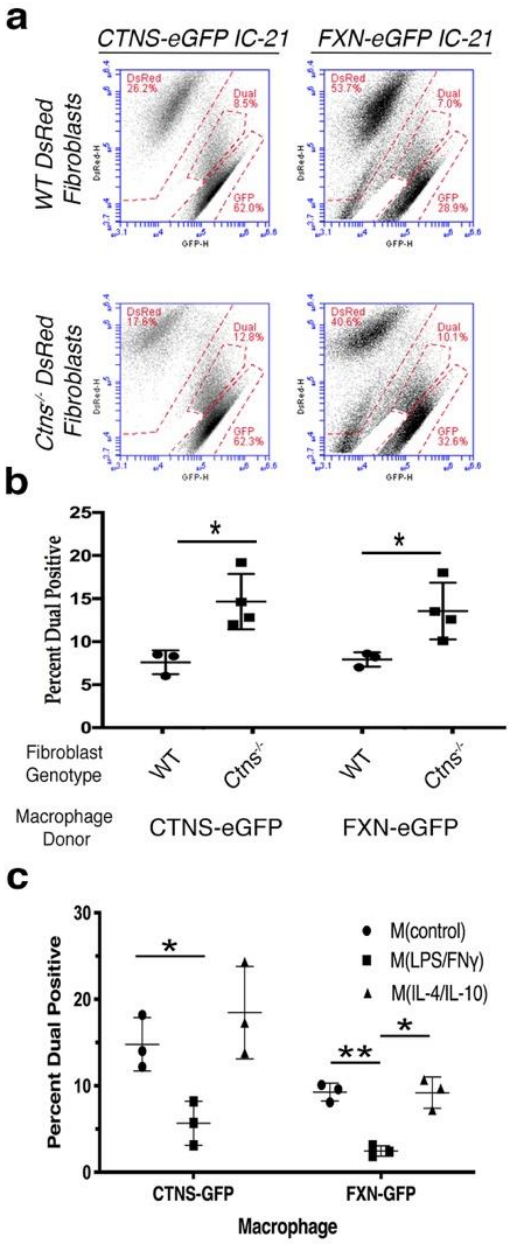

Figure 2.4: Flow cytometry confirms that intercellular trafficking is increased to diseased Ctns−/− fibroblasts and suppressed by proinflammatory polarization. (a) Representative FACS plots of DsRed (y-axis) and eGFP (x-axis) for 50,000 cells following co-culture of either cystinosin- or frataxin-eGFP and WT or Ctns−/− DsRed+ fibroblasts. Signal between eGFP and DsRed gates classified as a "dual-positive" eGFP+DsRed+ population. See Supplementary File 2, Fig. S4 for sorting and gating strategy. (b) Percentage quantification of eGFP+DsRed+ dual-positive cells in cystinosin- or frataxin-eGFP macrophage co-cultures with WT or Ctns−/− DsRed+ fibroblasts. Replicates consisted of co-cultures with fibroblasts derived from multiple mice (n = 4). (c) Quantification of dual-positive cell frequency after polarization treatment of co-cultures with cystinosin- or frataxin-eGFP and Ctns−/− DsRed+ fibroblasts (n = 3). All graphs shown as mean ± SD. P values determined by one-way ANOVA or student's t-tests. *P < 0.05, **P < 0.01.

Disruption of anti-inflammatory macrophage polarization with *Rac2*$^{-/-}$ HSPCs has no effect on HSPC transplantation efficacy or TNT formation. To determine if proinflammatory macrophages are responsible for tissue preservation in cystinosis following HSPC transplantation, we genetically perturbed macrophage polarization to assess if deficiencies prevented rescue of the cystinosis phenotype following HSPC transplantation. The *Rac2*$^{-/-}$ mouse model, disrupting the hematopoietic-specific Rho family GTPase Rac2, was chosen due to its functions in actin cytoskeletal reorganization and macrophage polarization (Roberts et al., 1999; Aflaki et al., 2011). Since RAC2 was shown to drive M(IL-4/IL-10) macrophage differentiation, the proinflammatory M(LPS/IFNγ) macrophage population was enriched in knockout *Rac2*$^{-/-}$ mice (Joshi et al., 2014; 2017). A very similar family member, *RAC1*, also has a role in the biogenesis of macrophage protrusions including invadopodia, lamellipodia and TNTs (Aflaki et al., 2011; Symons et al., 1996).

To test if *Rac2* elimination has any effect on HSPC transplantation efficacy, HSPCs isolated from *Rac2*$^{-/-}$ eGFP-transgenic mice were transplanted into 2-month-old *Ctns*$^{-/-}$ recipient mice. *Ctns*$^{-/-}$ mice transplanted with WT eGFP^{+} or *Ctns*$^{-/-}$ eGFP^{+} HSPCs proven effective or ineffective at prevention of cystinosis, respectively, were used as controls (Syres et al., 2009). HSPCs engraftment was measured by quantifying eGFP^{+} peripheral blood cells, which did not significantly differ between the three transplanted groups (average for WT −71.5%, *Ctns*$^{-/-}$ −75.6% and *Rac2*$^{-/-}$ −65.9%). Mice were sacrificed six months post-transplantation, and samples were collected for biochemical and phenotypic characterization. Assessment of tissue cystine content in WT HSPC recipients resulted in a dramatic reduction in cystine load in the liver, spleen, and kidneys relative to *Ctns*$^{-/-}$ HSPC-transplanted animals, as expected (Fig. 2.5a). Surprisingly, transplanted *Rac2*$^{-/-}$ HSPCs resulted in a decrease of cystine content to the same magnitude as WT HSPC controls. In addition, rescue of *Ctns* expression in tissues was similar in WT and *Rac2*$^{-/-}$ HSPC-transplanted *Ctns*$^{-/-}$ mice (Fig. 2.5b). Taken together, these data indicate that *Rac2*$^{-/-}$ HSPC transplantation is fully capable of restoring functional cystinosin to diseased tissue.

We then analyzed kidney sections by immunofluorescence for immune cell infiltration and observed co-localization between *Rac2*$^{-/-}$ eGFP HSPC progeny and macrophage markers such as F4/80 or

CD68 (Fig. 2.5c), indicating that typical macrophage differentiation remained unaltered. We also detected eGFP TNT-like protrusions within kidneys of both *Rac2*$^{-/-}$ and WT HSPC recipients that stained positive for actin, another hallmark of TNTs (Fig. 2.5d). These data confirm that knockout HSPC-derived cells retain the ability to form TNT-like protrusions in vivo.

Finally, we investigated the protrusive behavior and polarization phenotype of BMDMs isolated from *Rac2*$^{-/-}$ eGFP mice in vitro. We quantified co-cultures of freshly isolated WT eGFP+ and *Rac2*$^{-/-}$ eGFP+ BMDMs with *Ctns*$^{-/-}$ fibroblasts using our protrusion detection imaging algorithm (Supplementary File 1, Fig. S1) and observed no significant differences in protrusion frequency between WT- and *Rac2*$^{-/-}$-BMDMs ($P = 0.0472$; Fig. 2.5e). We then analyzed polarization markers and confirmed that in contrast with WT BMDMs, *Rac2*$^{-/-}$ BMDMs skew towards M(LPS/IFNγ) without any extrinsic stimulation (Fig. 2.5f–h). However, we note that the magnitude of change in mRNA expression of genes was overall either less dramatic (Tnfα, Il-10 or Fizz1) than the M(LPS/IFNγ) macrophages treatment in vitro (Fig. 2.1a) or were not significantly different between genotypes (iNos, Arg1 or Il-6) (Fig. 2.5f). Even so, a robust increase in MCP1 secretion and significantly decreased ARG1 enzymatic activity compared to WT BMDMs further confirmed the proinflammatory phenotype of the *Rac2*$^{-/-}$ macrophages (Fig. 2.5g,h). However, *Rac2*$^{-/-}$ eGFP BMDMs still formed tubes resembling TNTs consisting of actin and tubulin cytoskeletons (Fig. 2.5i) found lying above the substratum surface (data not shown). Taken together, these results indicate that while the polarization phenotype of *Rac2*$^{-/-}$ eGFP^{+} BMDMs is skewed towards a M(LPS/IFNγ) phenotype, both formation of TNT-like protrusions and *Rac2*$^{-/-}$ HSPCs transplantation efficacy remain unaffected.

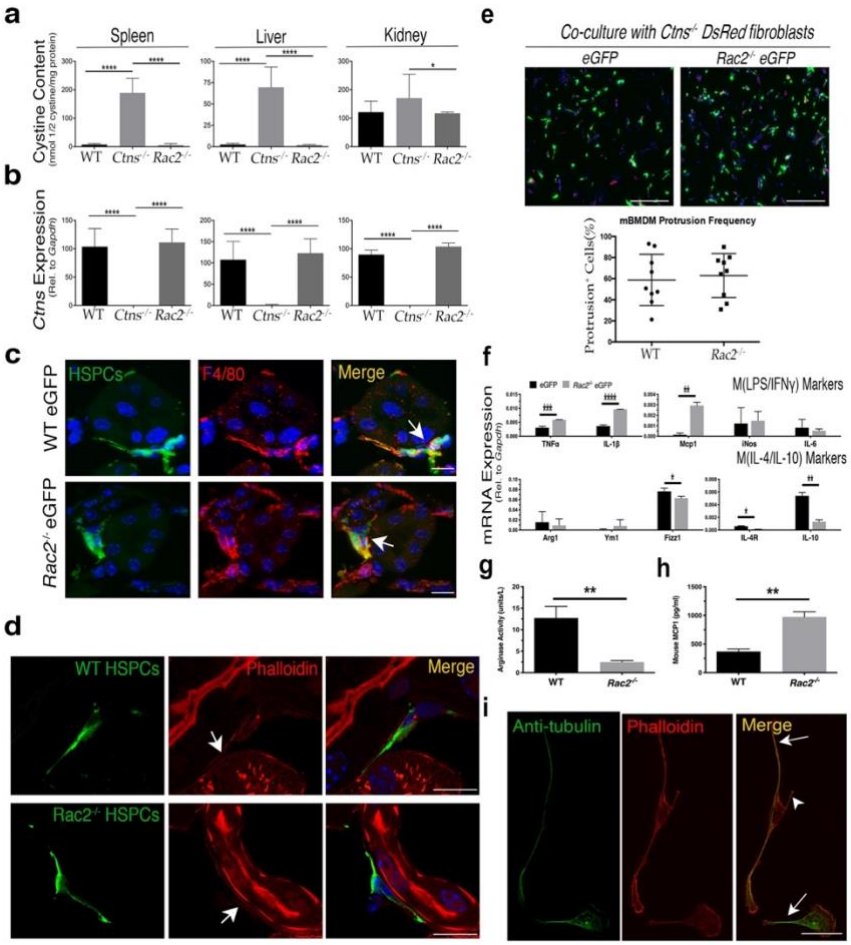

Figure 2.5: Enrichment of proinflammatory macrophages in vivo by transplantation of Rac2−/− HSPCs has no effect on efficacy in Ctns−/− mice or on BMDM TNT formation in vitro. (a) Histograms representing cystine content in spleens, livers and female kidneys as measured by mass spectrometry in Ctns−/− mice transplanted with WT HSPCs (n = 5), Ctns−/− HSPCs (n = 4), and Rac2−/− HSPCs (n = 4). Only female kidneys are shown, as previous observations indicate that kidneys need to be analyzed by sex16, and only 2 males were in the smallest recipient group. (b) mRNA quantitation of murine Ctns expression of transplanted Ctns−/− mice in spleen, liver and kidney. Histograms represent changes in Ctns expression relative to housekeeping control Gapdh. (c) Representative confocal micrograph of kidney sections of Ctns−/− mice transplanted with either WT or Rac2−/− HSPCs (green), probed with the macrophage marker F4/80 (red) and the nuclear stain DAPI (blue). Arrows indicate colocalization between eGFP HSPC progeny and F4/80 expression. (d) Confocal micrograph depicting kidney sections of a Ctns−/− mouse transplanted with WT (top) or Rac2−/− (bottom) eGFP HSPCs reveals thin eGFP TNT-like protrusions extending away from the cell body. Frozen sections were stained with anti-GFP to enhance visibility of HSPC progeny, and then probed with rhodamine phallodin to highlight actin within TNT-like structures (arrows). Scale bars: 10 μM. (e) BMDMs isolated from WT or Rac2−/− bone marrow were co-cultured with Ctns−/− DsRed+ fibroblasts and assesed for frequency of protrusions using automated analysis software (see Supplementary Fig. S1). Histogram displays quantification of percentage of BMDMs positive for protrusions (n = 3). Scale bar: 500 μM. (f) Bar graph displays mRNA expression of each individual pro- and anti-inflammatory macrophage polarization gene relative to housekeeping control Gapdh in WT or Rac2−/− BMDMs (n = 3). (g) Bar graph shows measurement of proinflammatory MCP1 cytokine secretion in conditioned media derived from WT or Rac2−/− BMDMs assessed using ELISA (n = 3). (h) Bar graph represents colorimetric measurements of M(IL-4/IL-10) marker ARG1 enzymatic activity in WT or Rac2−/− BMDMs normalized by comparison to blank with a standard curve (n = 3). (i) Confocal micrograph of Rac2−/− BMDM cytoskeletal immunostaining of tubulin (green) and actin (red) reveals some Rac2−/− BMDM protrusions only have actin (arrowhead) with others also containing tubulin (arrows). All scale bars are 10 μM except otherwise noted. All graphs shown as mean ± SD. P values were determined by one-way ANOVA or students t-tests. *P < 0.05, **P < 0.01, ***P < 0.001, ****P < 0.0001.

2.3: Discussion

Summary of Findings. In the present study, we investigated the phenotype of the HSPC-derived macrophages responsible for intercellular trafficking through TNTs. Several decades of research into macrophage subpopulations has elucidated differences in cytokine production, glucose metabolism, secondary messengers, stimulatory conditions, cellular morphology and numerous other factors which collectively lead to differences in macrophage biological activity, potentially including TNT-mediated trafficking (McWhorter et al., 2013; Wang et al., 2014). Using established assays in conjunction with novel imaging workflows, we observed a reduction in TNT formation and organelle transfer following LPS/IFNγ polarization, suggesting optimal TNT trafficking is impaired with increased proinflammatory stimulation. Unlike other imaging analysis platforms, our protrusion detection methodology requires no antibody staining or fixation and can function at relatively low magnification (40x), enabling large numbers of cells to be quickly and automatically analyzed without bias (Rostam et al., 2017; Alfonso-Garcia et al., 2016). Development of these tools not only increased our understanding of the morphological dynamics of macrophage polarization but also highlighted the potential for further study of cellular protrusion dynamics. This ImagePro Premier workflow could potentially allow quantitative analysis of other fluorescently-labeled cellular extensions such as filopodia, neuronal axons, or invadopodia in cancer.

Analyses of Findings. Following HSPC transplantation in vivo, tissue-integrated macrophages appeared to adopt a predominantly proinflammatory phenotype (Supplementary Fig. S8). In addition, HSPCs isolated from the *Rac2*$^{-/-}$ mouse model were enriched for a M(LPS/IFNγ) macrophage population but appeared to be as efficient in rescuing cystine build-up in the *Ctns*$^{-/-}$ mice as WT HSPCs. Our findings correlate with a recent study that demonstrated increased recruitment of proinflammatory immune cells in cystinosis, further highlighting the crucial role that inflammation plays in this disorder (Lobry et al., 2019). In addition, the dissonance between our in vitro and in vivo results reflects mounting evidence that the in vitro paradigm of macrophage activity can be a potentially misleading oversimplification (Martinez et al., 2014). Further

studies applying similar methodology to more complex in vitro models such as 3D culturing or iPSC-derived organoids or spheroids may help to bridge the gap between findings from cell culture and mouse models. That said, in vitro polarization can easily push cells beyond physiological levels of polarization. For example, the mRNA expression of important inflammatory mediators, including the master cytokine regulator TNFα, increased in M(LPS/IFNγ) IC-21 macrophages by over an order of magnitude; however, the magnitude of increase between *Rac2*$^{-/-}$ and WT BMDMs was far more modest. In terms of TNT-like protrusion formation, the reduced disruption of polarization induced by lack of *RAC2* might be mitigated by redundant pathways or signaling. Alternatively, these results could show that *RAC2* itself has no role in TNT formation. In contrast, siRNA-mediated knockdown of *RAC1* results in a reduction of TNTs (Hanna et al., 2017). Although the two proteins are quite similar (92%), Miskolci et al. report substantial differences in their subcellular localization – upon stimulation, *RAC1* is primarily localized to the periphery, while *RAC2* was distributed throughout the cell (Delage et al., 2016; Miskolci et al., 2016). Altogether, these data reveal that induction and function of TNT-like protrusions can be achieved by macrophages across the physiological spectrum of polarization, but is impaired when exogenous stimulation pushes cells to an extreme physiological state.

Like all cellular protrusions, TNTs require extensive modification and reorganization of the cytoskeleton to distort the plasma membrane and generate the protrusive force necessary to reshape the cell, elongate, and dynamically maintain the protrusion once formed1. Evidence also strongly implicates macrophage polarization in differentially modulating cytoskeletal dynamics and reorganization (Pergola et al., 2017; Jonsson et al., 2012). These shared pathways suggest polarization-induced alterations in expression and/or activity of TNT-regulator proteins could be responsible for the reduction in TNT-like protrusion formation following proinflammatory stimulation. We observed a reduction in M(LPS/IFNγ) BMDM mRNA expression of the known TNT inducer Lst1 which acts as a scaffold to recruit many proteins including filamin and the small GTPase RalA to the plasma membrane in order to generate and maintain TNTs (Schiller et al., 2013) (Supplementary Fig. S4). We also observed that proinflammatory BMDMs have decreased mRNA expression of Cdc42, a Rho-family GTPase involved in macrophage polarization

which binds N-WASP to control actin branching through Arp2/3 (Aflaki et al., 2011; Higgs et al., 1999). In macrophages along with Jurkat and HeLa cells, inhibition of Cdc42 reduces TNT formation and intercellular trafficking (Hase et al., 2009; Hanna et al., 2017; Arkwright et al., 2010). Interestingly, in neurons Cdc42 actually negatively regulates TNTs and trafficking while promoting filopodial formation (Delage et al., 2016). While one can speculate that the reduction of M(LPS/IFNγ) protrusion formation could be due to the increase of Lst1 disrupting normal formation of membrane focal points and/or because of the decrease of Cdc42 actin branching activity, drawing such mechanistic conclusions requires far more evidence than mRNA marker expression. That said, even though a direct connection between these expression changes and TNTs remain unclear, our data does support the central role of actin regulating Rho-family GTPases in TNT formation and provides further evidence of their involvement in macrophage polarization.

A major functional consequence of proinflammatory macrophage polarization was also a clear reduction in intercellular trafficking following induction of this phenotype (Fig. 2.3). Macrophages specifically are known to frequently form TNTs that are "thicker" and contain a tubulin core in addition to actin, which are known to be responsible for organelle trafficking (Naphade et al., 2015; Onfelt et al., 2006). Correspondingly, we observed an increase in protrusion frequency, size, length and elongated shape when BMDMs were cultured with cystinotic cells compared to macrophages alone (Fig. 2.2d,e). This observation combined with the shared reduction of trafficking and TNT-like protrusion formation following in vitro LPS/IFNγ polarization strongly supports the idea that TNTs form a major artery of intercellular delivery of lysosomes and mitochondria. Interestingly, not only were more cystinosin-eGFP-bearing lysosomes delivered to the diseased cells, which lack the lysosomal transmembrane protein cystinosin, but an increase in transfer of frataxin-eGFP-bearing mitochondria was also observed to cystinotic cells. Two hypotheses could explain these findings: (i) TNTs facilitate widespread delivery of cellular organelles to diseased cells so the fact that there are more thick TNTs inevitably leads to more trafficking of all cargos. No known TNT "gating" mechanisms have been identified to disprove this hypothesis, although overall protrusion structure has been shown to affect the types of molecular cargos transferred (Rustom et al., 2004); (ii) Cystinosis

also causes mitochondrial dysfunction characterized by dysregulation of the cyclic AMP cycle and impaired autophagy (Sansanwal et al., 2010; Bellomo et al., 2018). Therefore, it is also possible that whatever unknown media-soluble factor(s) causing increased TNT-like protrusion formation and thicker morphology also stimulates transfer of mitochondria as well as lysosomes. Whatever the cause may ultimately be, the finding that diseased cells increased macrophage-derived thick TNT formation and intercellular trafficking activity represents exciting new possibilities for the study of TNTs. A major thread of research from numerous groups has focused on how TNTs are involved in the transfer of harmful pathogenic molecules – ranging from HIV infection in T cells to cancer cell invasion to spreading misfolded tau protein aggregates (Eugenin et al., 2009; Abounit and Zurzolo 2012; Hanna et al., 2019). Thus, our findings that diseased cystinotic cells cause macrophages to increase TNT-mediated trafficking highlights the idea of TNTs as delivery system for regenerative medicine as opposed to mediating the spread of deleterious agents.

Conclusory Remarks. In this study, we investigated the phenotype of macrophages responsible for the widespread dissemination of molecular cargo via TNTs both in vitro and in vivo. We developed novel imaging tools allowing for automatic and unbiased quantification of cellular protrusions as well as intercellular trafficking efficacy in order to investigate these behaviors in the context of polarized macrophages. Given the apparent widespread and versatile nature of macrophage TNT transport, it is likely that many molecular products beyond functional lysosomes or mitochondrial proteins are transferred via TNTs; cargos that may not be readily secreted and thus be more difficult to deliver widely. Thus, understanding the mechanisms and cellular type that are responsible for TNT-mediated delivery will enhance the efficacy of numerous potential ex vivo therapeutic approaches targeting a wide variety of loss-of-function organelle disorders.

2.4: Methods

Mice and ethics statement. C57BL/6 *Rac2*$^{-/-}$ mice were provided by Dr. Durden (Moores Cancer Center, University of California, San Diego) and C57BL/6 *Ctns*$^{-/-}$ mice were provided by Dr. Antignac (Inserm U983, Paris, France). Enhanced green fluorescent protein (eGFP; C57BL/6-Tg(ACTB-EGFP)1Osb/j) and DsRed (B6.Cg-Tg(CAG-DsRed*MST)1Nagy/J) transgenic mice were purchased from The Jackson Laboratory (Bar Harbor, ME). *Ctns*$^{-/-}$ mice were cross-bred to both DsRed and GFP to produce *Ctns*$^{-/-}$ strains constitutively expressing either DsRed or GFP reporter genes as previously described (Syres et al., 2009; Harrison et al., 2011). All strains and mouse procedures were approved by the University of California, San Diego (UCSD) in accordance with the guidelines set forth by the Institutional Animal Care and Use Committee (Protocol ID S12288).

Macrophage and fibroblast isolation and culture. BMDMs were isolated from C57BL/6 mice according to standard protocols as described previously (Zhang et al., 2008). Briefly, mice were sacrificed using isoflurane, femurs and tibias were removed, and bone marrow was flushed using PBS with 1% fetal bovine serum (FBS). Cells were cultured at 37 °C and 5% CO2 in complete RPMI-1640 media (10% FBS, 2% penicillin/streptomycin) supplemented with 20% mCSF-containing L929-conditioned medium for seven days on tissue-culture (TC) treated plastic, with a media change at day 3. BMDMs were grown for no more than three passages and subcultured by scraping. For in vitro polarization experiments, BMDMs or IC-21 were cultured for at least 48 hours in complete media with either 100 ng/mL LPS and 50 ng/mL IFNγ or 10 ng/mL IL-4 and IL-10 (BioLegend) for M(LPS/IFNγ) and M(IL-4/IL-10) polarization, respectively. Primary fibroblasts were isolated from neonatal mouse skin biopsies by allowing them to grow out of small skin pieces (~0.5 cm2) attached to the culture dishes for several days prior to skin removal and subculture in complete DMEM media (10% FBS, 2% penicillin/streptomycin).

Co-culture growth and imaging. 75,000 macrophages and 50,000 fibroblasts were cultured together in 6-well dishes under polarization conditions for two days. Cells were washed with warm PBS and fixed for 10 mins at 37 °C in 4% paraformaldehyde (PFA). Cells were washed in PBS again and imaged at 40X on the BZX-700 Fluorescent Microscope (Keyence). Five large image stitches (5 × 5) were generated per experimental condition, with acquisition settings held constant within experimental runs.

Imaging analysis: protrusion quantification. Stitched images were calibrated in ImagePro Premier (Media Cybernetics) for automated quantification of protrusion frequency. eGFP+ macrophages were size-selected by filtration of objects with an area 100 μm2 or larger and then masked to reduce noise artifacts (Supplementary Fig. S1a, Step I). Protrusions were isolated by repeatedly passing a morphological erosion filter (2 × 2 square, 7 passes) over the image which erased peripheral cellular signal, followed by applying a dilation that restored signal to the central cell body (Step II). Subtracting the processed image from the original mask resulted in selection of regions protruding from the main cell body, which can be filtered by a highly variable set of size parameters to yield either thin TNT-like structures or other thicker protrusions (Supplementary Fig. S1b) (filters for TNTs: 20 μm2 minimum area, 10 μm2 minimum longest axis, 0.6 maximum circularity, 1.9 box area minimum). Finally, the selected protrusion area was overlaid with the original image and cells were classified as either protrusion-positive or -negative based on signal intensity; overlap of protrusion and cell body yielded a positive result (Step III - IV). All segmentation, adjustment and filtration factors were trained and optimized blind to condition and applied automatically to batch images using ImagePro Premier macros.

Imaging analysis: transfer quantification. Stitched images were imported as above and split into "donor" and "recipient" (DsRed) channels. Donors included genetically-encoded, fluorescently-labeled organelles like cystinosin-eGFP lysosomes and frataxin-eGFP mitochondrial protein, as well as transient stains (for example, Wheat Germ Agglutin (WGA) labels of the plasma membrane). Recipient cell outline was selected (minimum area 100 μm2) and applied as a region of interest (ROI) to the donor channel. Any signal

within this ROI was adjusted and selected, taking caution to use controls lacking any donor signal to establish fluorescent background (Supplementary Fig. S3b, top). Filtered donor signal was combined with original recipient outline and signal overlap was used again to classify recipients as donor-positive or -negative. Exclusion of any signal at the boundary of recipient cells, as well as size filtration of donor molecules (maximum area 25 μm2), helped reduce false-positive imaging artifacts.

Flow cytometry. Co-cultures were seeded as described previously, but onto non-tissue culture-treated plastics to enable trypsinization of macrophages. Co-cultures were washed in ice-cold PBS, trypsinized at room temperature (RT) and rapidly rinsed in cold media before centrifugation at 4 °C. Cells were resuspended in cold PBS and vortexed, then run through the BD Accuri C6 cytometer (BD Biosciences). Debris was filtered by SSC/FSC gating with 50,000 cellular events collected. Macrophages and fibroblasts without any fluorescent tags were used to establish an exclusion region from final co-culture sort, while eGFP+, DsRed+ and dual-positive gates were drawn with each cell type seeded alone. For macrophage polarization markers, BMDMs were polarized as described, then scraped and resuspended in ice cold FACS buffer (1% FBS, 0.1% sodium azide in PBS). Cells were treated with Fc block (BD Biosciences) for 10 mins before incubation for 1 hr on ice in the dark with appropriate antibodies. Cells were washed three times in FACS buffer before immediately reading on the cytometer. Antibodies are as follows: F4/80 PE (Biolegend 565410), CD80 FITC (Biolegend 104706), CD126/IL6Rα APC (115811), CD206 PE (Biolegend 141795).

Quantitative PCR. To measure gene expression in BMDMs/IC-21 and explanted tissues, total RNA was extracted with TRIzol Reagent (Invitrogen) per manufacturer's recommendations. A total of 1 μg isolated RNA was reverse transcribed into cDNA with the iScript cDNA synthesis kit (Bio-Rad). Real-time PCR was performed using iTaq Universal SYBR Green on a CFX96 thermocycler (Bio-Rad) under the following conditions: 95 °C (30 s), 40 cycles of 95 °C (5 s) and 60 °C (30 s), then 65 °C (5 s) and finally 95 °C (5 s). Reaction mixture consisted of 3 μL cDNA (5 ng/ul), 0.6 μL forward and reverse primer (10 μM), 1.8 μL H20 and 5 μL SYBR green. Samples were normalized to Glyceraldehyde 3-phosphate dehydrogenase

(Gapdh) and analyzed according to the delta/delta Ct method. All primer sequences are shown in Supplementary Table S1.

Immunoblotting. Total protein was harvested and resuspended in 1% SDS from cultures of 1 × 106 BMDMs and IC-21 using TRIzol Reagent (Invitrogen) per manufacturers protocol and quantified using the Pierce BCA Protein Assay kit (Thermo Fisher Scientific). 10–20 μg of protein was subjected to SDS-PAGE, transferred to a PVDF membrane, blocked in 5% Protein Blocking Reagent (Azure) for 1 hr at RT and then probed overnight with primary antibodies at 4 °C. Antibodies included M(LPS/IFNγ) markers iNOS (abcam ab3523; 1:1,000) and MCP1(CST 2029S; 1:500), M(IL-4/IL-10) markers ARG1 (Santa Cruz sc-20150; 1:200), CD206 (abcam ab64693; 1:500), macrophage marker CD68 (abcam ab53444; 1:500) and loading control Gapdh (abcam ab8245; 1:1,000). The following day, blots were washed three times in Protein Wash Buffer (Azure) and probed with HRP-conjugated secondary antibody of the appropriate species at 1:2,500 for one hour at room temperature. Blots were then washed three times in Protein Wash Buffer and once with TBS, developed with Radiance Plus ECL Reagent (Azure), and imaged on the c600 Imager (Azure).

ELISA and arginase activity assays. Conditioned media for ELISA experiments were generated by culture of 200,000 IC-21 or BMDM in polarization media for two days and then centrifuged at 2,000 g for 10 mins to remove cell debris. MCP1 SimpleStep ELISA (abcam ab208979) was performed on 1:2,000 diluted media in duplicate per manufactures recommendation. Arginase enzymatic activity was quantitated using 1 × 106 polarized macrophages using a colorimetric assay according to manufactures protocol (Sigma-Aldrich).

Cell proliferation and apoptosis. Metabolically active cells were measured using the Cell Proliferation Reagent WST-1 (Roche) by seeding 5,000 IC-21 or BMDMs in 100 μL per well in triplicate in two identical 96 well plates. After treatment, 10 μL of WST-1 was added to all cell and blank wells of one plate, while the other was changed back into normal macrophage media. Absorbance was measured at 260 nm,

following one hour of incubation and a corresponding standard curve was generated with blank-subtracted values normalized to untreated controls. The other plate was processed identically several days later.

Cytochalasin B. Cytochalasin B (Sigma) was diluted from stock to form 1,000X solution in DMSO and seeded with 100,000 macrophages. Treated and control cells were imaged as above at 24 hours post-seeding, followed by a drug washout with fresh media. At 24- and 48-hour post-removal, cells were again imaged at the same locations.

Immunofluorescence. Cells were seeded onto glass coverslips for high-resolution imaging. After growth, cells were rinsed in PBS and fixed in warm 4% PFA for 15 min at 37 °C. Cells were blocked in blocking buffer (1% BSA, 5% goat serum, 0.3% triton X-100) for 1 hour at RT, and probed with primary anti-tubulin antibody (abcam ab6160; 1:500) diluted in antibody buffer (1% BSA, 0.3% triton X-100) overnight at 4 °C. Following three washes of PBS, cells were incubated in secondary antibody and phalloidin (1:200) for 1 hour at RT. Cells were again rinsed, mounted on glass overnight in Prolong Gold with DAPI (Invitrogen), and imaged the following day.

HSPC isolation, transplantation, and cystine measurements. HSPCs were isolated and transplanted into lethally irradiated recipient mice as previously described (Harrison et al., 2013). In brief, bone marrow cells were flushed from the tibia and femurs of 6 to 8-week old WT, *Ctns*$^{-/-}$ and *Rac2*$^{-/-}$ eGFP mice. HSPCs were isolated by immunomagnetic separation using magnetic beads conjugated to anti-ScaI antibody (Miltenyi Biotec). Isolated HSPCs were directly transplanted via tail vein injection of 100 µL containing 1 × 106 HSPCs into *Ctns*$^{-/-}$ mice subjected to a lethal 7 Gy irradiation the previous day. Engraftment was assessed by percentage of eGFP^{+} cells in peripheral blood at 2- and 4-month post-transplantation. At six months post-transplantation, recipient mice were sacrificed, and kidney, liver, and spleen samples were isolated and analyzed by qPCR and mass spectrometry for murine Ctns expression and overall cystine load as previously described (Yeagy et al., 2011).

Statistics. All statistical analyses were performed in Prism (GraphPad). Student's t-test was performed for comparisons of two groups, while one-way analysis of variance (ANOVA) was employed for comparisons of three or more conditions. Outliers were identified and excluded from larger protrusion measurement dataset by the ROUT method (Motulsky et al., 2006). All graphs display mean ± standard deviation.

2.5: Acknowledgements

Chapter 2, in whole, is a reprint of the material as it appears in *Goodman, S., Naphade, S.,* ***Khan, M.****, Sharma, J. & Cherqui, S. Macrophage polarization impacts tunneling nanotube formation and intercellular organelle trafficking. Sci Rep 9, 14529, doi:10.1038/s41598-019-50971-x (2019).* The master's thesis author was a key investigator and co-author of this paper.

2.6: References

Abounit, S. & Zurzolo, C. Wiring through tunneling nanotubes–from electrical signals to organelle transfer. Journal of cell science 125, 1089–1098, https://doi.org/10.1242/jcs.083279 (2012).

Aflaki, E., Balenga, N. A. B., Luschnig-Schratl, P., Wolinski, H., Povoden, S., Chandak, P. G., Bogner-Strauss, J. G., Eder, S., Konya, V., Kohlwein, S. D., Heinemann, A., & Kratky, D. (2011). Impaired Rho GTPase activation abrogates cell polarization and migration in macrophages with defective lipolysis. *Cellular and Molecular Life Sciences*, *68*(23), 3933–3947. https://doi.org/10.1007/s00018-011-0688-4

Alfonso-Garcia, A., Smith, T., Datta, R., Luu, T., Gratton, E., Potma, E., & Liu, W. Label-free identification of macrophage phenotype by fluorescence lifetime imaging microscopy. J Biomed Opt 21, 46005, https://doi.org/10.1117/1.JBO.21.4.046005 (2016).

Ariazi J, Benowitz A, De Biasi V, Den Boer ML, Cherqui S, Cui H, Douillet N, Eugenin EA, Favre D, Goodman S, Gousset K, Hanein D, Israel DI, Kimura S, Kirkpatrick RB, Kuhn N, Jeong C, Lou E, Mailliard R, Maio S, Okafo G, Osswald M, Pasquier J, Polak R, Pradel G, de Rooij B, Schaeffer P, Skeberdis VA, Smith IF, Tanveer A, Volkmann N, Wu Z and Zurzolo C (2017) Tunneling Nanotubes and Gap Junctions–Their Role in Long-Range Intercellular Communication during Development, Health, and Disease Conditions. *Front. Mol. Neurosci*. 10:333. doi: 10.3389/fnmol.2017.00333

Arkwright, P. D., Luchetti, F., Tour, J., Roberts, C., Ayub, R., Morales, A. P., Rodríguez, J. J., Gilmore, A., Canonico, B., Papa, S., & Esposti, M. D. (2010). Fas stimulation of T lymphocytes promotes rapid intercellular exchange of death signals via membrane nanotubes. *Cell Research*, *20*(1), 72–88. https://doi.org/10.1038/cr.2009.112

Austefjord, M. W., Gerdes, H. H., & Wang, X. Tunneling nanotubes: Diversity in morphology and structure. Commun Integr Biol 7, e27934, https://doi.org/10.4161/cib.27934 (2014).

Bellomo, F., Signorile. A., Tamma, G., Ranieri, Mi., Emma, F., & Rasmo, D. D. Impact of atypical mitochondrial cyclic-AMP level in nephropathic cystinosis. Cell Mol Life Sci 75, 3411–3422, https://doi.org/10.1007/s00018-018-2800-5 (2018).

Ieva Bruzauskaite, I., Bironaite, D., Bagdonas, E., Skeberdis, V. A., Denkovskij, J., Tamulevicius, T., Uvarovas, V., & Eiva Bernotiene, E. Relevance of HCN2-expressing human mesenchymal stem cells for the generation of biological pacemakers. Stem Cell Res Ther 7, 67, https://doi.org/10.1186/s13287-016-0326-z (2016).

Bukoreshtliev, N. V., Wang, X., Hodneland, E., Gurke, S., Barroso, J. F. V., & Gerdes, H. H. Selective block of tunneling nanotube (TNT) formation inhibits intercellular organelle transfer between PC12 cells. FEBS Lett 583, 1481–1488, https://doi.org/10.1016/j.febslet.2009.03.065 (2009).

Busi, M. V. & Gomez-Casati, D. F. Exploring frataxin function. IUBMB Life 64, 56–63, https://doi.org/10.1002/iub.577 (2012).

Cherqui, S., Sevin, C., Hamard, G., Kalatzis, V., Sich, M., Pequignot, M. O., Gogat, K., Abitbol, M., Broyer, M., Gubler, M. C., & Antignac, C. Intralysosomal cystine accumulation in mice lacking cystinosin, the protein defective in cystinosis. Molecular and cellular biology 22, 7622–7632 (2002).

Chinnery, H. R., Pearlman, E. & McMenamin, P. G. Cutting edge: Membrane nanotubes in vivo: a feature of MHC class II+ cells in the mouse cornea. Journal of immunology 180, 5779–5783 (2008).

Delage, E., Cervantes, D. C., Pénard, E., Schmitt, C., Syan, S., Disanza, A., Scita, G., & Zurzolo, C. Differential identity of Filopodia and Tunneling Nanotubes revealed by the opposite functions of actin regulatory complexes. Sci Rep 6, 39632, https://doi.org/10.1038/srep39632 (2016).

Emma, F., Nesterova, G., Langman, C., Labbé, A., Cherqui, S., Goodyer, P., Janssen, M. C., Greco, M., Topaloglu, R., Elenberg, E., Dohil, R., Trauner, D., Antignac, C., Cochat, P., Kaskel, F., Servais, A., Wühl, E., Niaudet, P., Hoff, W. V., Gahl, W., & Levtchenko, E. Nephropathic cystinosis: an international consensus document. Nephrol Dial Transplant 29(Suppl 4), iv87–94, https://doi.org/10.1093/ndt/gfu090 (2014).

Eugenin, E. A., Gaskill, P. J., & Berman, J. W. Tunneling nanotubes (TNT) are induced by HIV-infection of macrophages: a potential mechanism for intercellular HIV trafficking. Cell Immunol 254, 142–148, https://doi.org/10.1016/j.cellimm.2008.08.005 (2009).

Gabriel, S. S., Belge, H., Gassama, A., Debaix, H., Luciani, A., Fehr, T., & Devuyst, O. Bone marrow transplantation improves proximal tubule dysfunction in a mouse model of Dent disease. Kidney international 91, 842–855, https://doi.org/10.1016/j.kint.2016.11.016 (2017).

Gaide Chevronnay, H. P., Janssens, V., Smissen, P. V. D., Rocca, C. J., Liao, X. H., Refetoff, S., Pierreux, C. E., Cherqui, S., & Courtoy, P. J. Hematopoietic Stem Cells Transplantation Can Normalize Thyroid Function in a Cystinosis Mouse Model. Endocrinology 157, 1363–1371, https://doi.org/10.1210/en.2015-1762 (2016).

Gousset, K., Marzo, L., Commere, P. H., & Zurzolo, C. Myo10 is a key regulator of TNT formation in neuronal cells. Journal of cell science 126, 4424–4435, https://doi.org/10.1242/jcs.129239 (2013).

Gurke, S., Barroso, J. F. V., Hodneland, E., Bukoreshtliev, N. V., Schlicker, O., & Gerdes, H. H. Tunneling nanotube (TNT)-like structures facilitate a constitutive, actomyosin-dependent exchange of endocytic organelles between normal rat kidney cells. Experimental cell research 314, 3669–3683, https://doi.org/10.1016/j.yexcr.2008.08.022 (2008).

Hanna, S. J., McCoy-Simandle, K., Leung, E., Genna, A., Condeelis, J., & Cox, D. Tunneling nanotubes, a novel mode of tumor cell-macrophage communication in tumor cell invasion. Journal of cell science 132, https://doi.org/10.1242/jcs.223321 (2019).

Hanna, S. J., McCoy-Simandle, K., Miskolci, V., Guo, P., Cammer, M., Hodgson, L., & Cox, D. The Role of Rho-GTPases and actin polymerization during Macrophage Tunneling Nanotube Biogenesis. Sci Rep 7, 8547, https://doi.org/10.1038/s41598-017-08950-7 (2017).

Harrison, F., Yeagy, B. A., Rocca, C. J., Kohn, D. B., Salomon , D. R., & Cherqui, S. Hematopoietic stem cell gene therapy for the multisystemic lysosomal storage disorder cystinosis. Molecular therapy: the journal of the American Society of Gene Therapy 21, 433–444, https://doi.org/10.1038/mt.2012.214 (2013).

Hase, K., Kimura, S., Takatsu, H., Ohmae, M., Kawano, S., Kitamura, H., Ito, M., Watarai, H., Hazelett, C. C., Yeaman, C., & Ohno, H. M-Sec promotes membrane nanotube formation by interacting with Ral and the exocyst complex. Nature cell biology 11, 1427–1432, https://doi.org/10.1038/ncb1990 (2009).

Higgs, H. N. & Pollard, T. D. Regulation of actin polymerization by Arp2/3 complex and WASp/Scar proteins. The Journal of biological chemistry 274, 32531–32534, https://doi.org/10.1074/jbc.274.46.32531 (1999).

Jonsson, F., Gurniak, C. B., Fleischer, B., Kirfel, G., & Witke, W. Immunological responses and actin dynamics in macrophages are controlled by N-cofilin but are independent from ADF. PloS one 7, e36034, https://doi.org/10.1371/journal.pone.0036034 (2012).

Joshi, S., Singh, A. R., Zulcic, M., Bao, L., Messer, K., Ideker, T., Dutkowski, J., & Durden, D. L. Rac2 controls tumor growth, metastasis and M1-M2 macrophage differentiation in vivo. PloS one 9, e95893, https://doi.org/10.1371/journal.pone.0095893 (2014).

Joshi, S., Singh, A. R., Wong, S. S., Zulcic, M., Jiang, M., Pardo, A., Selman, M., Hagood, J. S., & Durden, D. L. Rac2 is required for alternative macrophage activation and bleomycin induced pulmonary fibrosis; a macrophage autonomous phenotype. PloS one 12, e0182851, https://doi.org/10.1371/journal.pone.0182851 (2017).

Kalatzis, V., Cherqui, S., Antignac, C., & Gasnier, B. Cystinosin, the protein defective in cystinosis, is a H(+)-driven lysosomal cystine transporter. The EMBO journal 20, 5940–5949, https://doi.org/10.1093/emboj/20.21.5940 (2001).

Lobry, T., Miller, M., Nevo, N., Rocca, C. J., Zhang, J., Catz, S. D., Moore, F., Thomas, L., Pouly, D., Bailleux, A., Guerrera, I. C., Gubler, M. C., Cheung, W. W., Mak, R. H., Montier, T., Antignac, C., & Cherqui, S. Interaction between galectin-3 and cystinosin uncovers a pathogenic role of inflammation in kidney involvement of cystinosis. Kidney international, https://doi.org/10.1016/j.kint.2019.01.029 (2019).

Martinez, F. O., & Gordon, S. The M1 and M2 paradigm of macrophage activation: time for reassessment. F1000prime reports 6, 13, https://doi.org/10.12703/P6-13 (2014).

McWhorter, F. Y., Wang, T., Nguyen, P., Chung, T., & Liu, W. F. Modulation of macrophage phenotype by cell shape. Proc Natl Acad Sci USA 110, 17253–17258, https://doi.org/10.1073/pnas.1308887110 (2013).

Medic, G., van der Weijden, M., Karabis, A., & Hemels, M. A systematic literature review of cysteamine bitartrate in the treatment of nephropathic cystinosis. Curr Med Res Opin 33, 2065–2076, https://doi.org/10.1080/03007995.2017.1354288 (2017).

Mills, C. D., Kincaid, K., Alt, J. M., Heilman, M. J., & Hill, A. M. M-1/M-2 macrophages and the Th1/Th2 paradigm. Journal of immunology 164, 6166–6173 (2000).

Miskolci, V., Wu, B., Moshfegh, Y., Cox, D., & Hodgson, L. Optical Tools To Study the Isoform-Specific Roles of Small GTPases in Immune Cells. Journal of immunology 196, 3479–3493, https://doi.org/10.4049/jimmunol.1501655 (2016).

Motulsky, H. J. & Brown, R. E. Detecting outliers when fitting data with nonlinear regression - a new method based on robust nonlinear regression and the false discovery rate. BMC Bioinformatics 7, 123, https://doi.org/10.1186/1471-2105-7-123 (2006).

Murray, P. J., Allen, J. E., Biswas, S. K., Fisher, E. A., Gilroy, D. W., Goerdt, S., Gordon, S., Hamilton, J. A., Ivashkiv, L. B., Lawrence, T., Locati, M., Mantovani, A., Martinez, F. O., Mege, J. L., Mosser, D. M., Natoli, G., Saeij, J. P., Schultze, J. L., Shirey, K. A., Sica, A., Suttles, J., Udalova, I., Ginderachter, J. A. V., Vogel, S. N., & Wynn, T. A. Macrophage activation and polarization: nomenclature and experimental guidelines. Immunity 41, 14–20, https://doi.org/10.1016/j.immuni.2014.06.008 (2014).

Naphade, S.,Sharma, J., Chevronnay, H. P. G., Shook, M. A., Yeagy, B. A., Rocca, C. J., Ur, S. N., Lau, A. J., Courtoy, P. J., & Cherqui, S. Brief reports: Lysosomal cross-correction by hematopoietic stem cell-derived macrophages via tunneling nanotubes. Stem cells 33, 301–309, https://doi.org/10.1002/stem.1835 (2015).

Onfelt, B., Nedvetzki, S., Benninger, R. K. P., Purbhoo, M. A., Sowinski, S., Hume, A. N., Seabra, M. C., Neil, M. A. A., French, P. M. W., & Davis, D. M. Structurally distinct membrane nanotubes between human macrophages support long-distance vesicular traffic or surfing of bacteria. Journal of immunology 177, 8476–8483 (2006).

Osswald, M., Solecki, G., Wick, W., & Winkler, F. A malignant cellular network in gliomas: potential clinical implications. NeuroOncol 18, 479–485, https://doi.org/10.1093/neuonc/now014 (2016).

Pergola, C., Schubert, K., Pace, S., Ziereisen, J., Nikels, F., Scherer, O., Hüttel, S., Zahler, S., Vollmar, A. M., Weinigel, C., Rummler, S., Müller, R., Raasch, M., Mosig, A., Koeberle, A., & Werz, O. Modulation of actin dynamics as potential macrophage subtype-targeting anti-tumour strategy. Sci Rep 7, 41434, https://doi.org/10.1038/srep41434 (2017).

Raggi, F., Pelassa, S., Pierobo, D., Penco, F. Gattorno, M., Novelli, F., Eva, A., Varesio, L., Giovarelli, M., & Bosco, M. C. Regulation of Human Macrophage M1-M2 Polarization Balance by Hypoxia and the Triggering Receptor Expressed on Myeloid Cells-1. Front Immunol 8, 1097, https://doi.org/10.3389/fimmu.2017.01097 (2017).

Ridley, A. J. Rho GTPases and actin dynamics in membrane protrusions and vesicle trafficking. Trends Cell Biol 16, 522–529, https://doi.org/10.1016/j.tcb.2006.08.006 (2006).

Roberts, A. W., Kim, C., Zhen, L., Lowe, J. B., Kapur, R., Petryniak, B., Spaetti, A., Pollock, J. D., Borneo, J. B., Bradford, G. B., Atkinson, S. J., Dinauer, M. C., Williams, D. A. Deficiency of the hematopoietic cell-specific Rho family GTPase Rac2 is characterized by abnormalities in neutrophil function and host defense. Immunity 10, 183–196 (1999).

Rocca, C. J., Goodman, S. M., Dulin, J. N., Haquang, J. H., Gertsman, I., Blondelle, J., Smith, J. L. M., Heyser, C. J., & Cherqui, S. Transplantation of wild-type mouse hematopoietic stem and progenitor cells ameliorates deficits in a mouse model of Friedreich's ataxia. Sci Transl Med 9, https://doi.org/10.1126/scitranslmed.aaj2347 (2017).

Rocca, C. J., Kreymerman, A., Ur, S. N., Frizzi, K. E., Naphade, S., Lau, A., Tran, T., Calcutt, N. A., Goldberg, J. L., & Cherqui, S. Treatment of Inherited Eye Defects by Systemic Hematopoietic Stem Cell Transplantation. Invest Ophthalmol VisSci 56, 7214–7223, https://doi.org/10.1167/iovs.15-17107 (2015).

Rostam, H. M., Reynolds, P. M., Alexander, M. R., Gadegaard, N., & Ghaemmaghami, A. M. Image based Machine Learning for identification of macrophage subsets. Sci Rep 7, 3521, https://doi.org/10.1038/s41598-017-03780-z (2017).

Rustom, A., Saffrich, R., Markovic, I., Walther, P., & Gerdes, H. H. Nanotubular highways for intercellular organelle transport. Science 303, 1007–1010, https://doi.org/10.1126/science.1093133 (2004)

Sansanwal, P., Yen, B., Gahl, W. A., Ma, Y., Ying, L., Wong, J. L. C., & Sarwal, M. M. Mitochondrial autophagy promotes cellular injury in nephropathic cystinosis. Journal of the American Society of Nephrology: JASN 21, 272–283, https://doi.org/10.1681/ASN.2009040383 (2010).

Schiller, C., Diakopoulos, K. N., Rohwedder, I., Kremmer, E., Toerne, C. V., Ueffing, M., Weidle, U. H., Ohno, H., & Weiss, E. H. LST1 promotes the assembly of a molecular machinery responsible for tunneling nanotube formation. Journal of cell science 126, 767–777, https://doi.org/10.1242/jcs.114033 (2013)

Souriant, S., Balboa, L., Dupont, M., Pingris, K., Kviatcovsky, D., Cougoule, C., Lastrucci, C., Bah, A., Gasser, R., Poincloux, R., Raynaud-Messina, B., Saati, T. A., Inwentarz, S., Poggi, S., Jose Moraña, E. J., González-Montaner, P., Corti, M., Lagane, B., Vergne, I., Allers, C., Kaushal, D., Kuroda, M. J., Sasiain, M. D. C., Neyrolles, O., Maridonneau-Parini, I., Lugo-Villarino, G., & Vérollet, C. Tuberculosis Exacerbates HIV-1 Infection through IL-10/STAT3-Dependent Tunneling Nanotube Formation in Macrophages. Cell Rep 26, 3586–3599 e3587, https://doi.org/10.1016/j.celrep.2019.02.091 (2019).

Sowinski, S., Alakoskela, J. M., Jolly, C., & Davis, D. M. Optimized methods for imaging membrane nanotubes between T cells and trafficking of HIV-1. Methods 53, 27–33, https://doi.org/10.1016/j.ymeth.2010.04.002 (2011).

Symons, M. Rho family GTPases: the cytoskeleton and beyond. Trends Biochem Sci 21, 178–181 (1996).

Syres, K., Harrison, F., Tadlock, M., Jester, J. V., Simpson, J., Roy, S., Salomon, D. R., & Cherqui, S. Successful treatment of the murine model of cystinosis using bone marrow cell transplantation. Blood 114, 2542–2552, https://doi.org/10.1182/blood-2009-03-213934 (2009).

Tatano, Y., Shimizu, T., & Tomioka, H. Unique macrophages different from M1/M2 macrophages inhibit T cell mitogenesis while upregulating Th17 polarization. Sci Rep 4, 4146, https://doi.org/10.1038/srep04146 (2014).

Van den Bossche, J., Lamers, W. H., Koehler, E. S., Geuns, J. M. C., Alhonen, L., Uimari, A., Pirnes-Karhu, S., Overmeire, E. V., Morias, Y., Brys, L., Vereecke, L., Baetselier, P. D., & Ginderachter, J. A. V. Pivotal Advance: Arginase-1-independent polyamine production stimulates the expression of IL-4-induced alternatively activated macrophage markers while inhibiting LPS-induced expression of inflammatory genes. Journal of leukocyte biology 91, 685–699, https://doi.org/10.1189/jlb.0911453 (2012).

Wang, N., Liang, H., & Zen, K. Molecular mechanisms that influence the macrophage m1-m2 polarization balance. Front Immunol5, 614, https://doi.org/10.3389/fimmu.2014.00614 (2014).

Wang, X. & Gerdes, H. H. Transfer of mitochondria via tunneling nanotubes rescues apoptotic PC12 cells. Cell Death Differ 22, 1181–1191, https://doi.org/10.1038/cdd.2014.211 (2015).

Wang, X., Veruki, M. L., Bukoreshtliev, N. V., Hartveit, E., & Gerdes, H. H. Animal cells connected by nanotubes can be electrically coupled through interposed gap-junction channels. Proc Natl Acad Sci USA 107, 17194–17199, https://doi.org/10.1073/pnas.1006785107 (2010).

Wittig, D., Wang, X., Walter, C., Gerdes, H. H., Funk, R. H. W., & Roehlecke, C. Multi-level communication of human retinal pigment epithelial cells via tunneling nanotubes. PloS one 7, e33195, https://doi.org/10.1371/journal.pone.0033195 (2012).

Yeagy, B. A., Harrison, F., Gubler, M. C., Koziol, J. A., Salomon, D. R., & Cherqui, S. Kidney preservation by bone marrow cell transplantation in hereditary nephropathy. Kidney international 79, 1198–1206, https://doi.org/10.1038/ki.2010.537 (2011).

Ying, W., Cheruku, P. S., Bazer, F. W., Safe, S. H., & Zhou, B. Investigation of macrophage polarization using bone marrow derived macrophages. J Vis Exp, https://doi.org/10.3791/50323 (2013).

Zhang, X., Goncalves, R., & Mosser, D. M. The isolation and characterization of murine macrophages. Curr Protoc Immunol Chapter 14, Unit 14 11, https://doi.org/10.1002/0471142735.im1401s83 (2008).

Chapter 3: *Shpk*-deficient Hematopoietic Stem Cell Therapy Temains Effective to Rescue Cystinosis

The following section 3, in part, is a reprint of a manuscript entitled "*Shpk*-deficient hematopoietic stem cell therapy remains effective to rescue cystinosis" that is in preparation for publication.

3.1: Introduction

Cystinosis is an autosomal-recessive lysosomal storage disorder caused by mutations in the *CTNS* gene that affects about one out of every 100,000 live births (Ariazi et al., 2017). Over 100 unique mutations ranging from single base substitutions to large indels have been identified as causing for cystinosis by perturbing the localization or function of cystinosin, an ubiquitously expressed lysosomal transmembrane cystine-proton transporter (Cherqui et al., 2002, Kalatzis et al., 2004). Without functional cystinosin, cystine accumulates within the lysosomes and deposits as crystals throughout the body, causing organ failure (Elmonem et al., 2016). While renal Fanconi syndrome presents as the first clinical manifestation in the first year of life, patients also experience later end-stage renal failure, photophobia, muscle atrophy, diabetes, hypothyroidism and neurological defects (Bäumner and Weber 2018). Current specific treatment is the drug cysteamine, which delays symptomatic progression and does not address the root genetic pathology (Biffi et al., 2017).

Our group has focused on developing hematopoietic stem cell (HSPC) transplantation therapy for cystinosis (Cherqui et al., 2002). We transplanted wildtype (WT) or gene-corrected HSPCs into lethally irradiated knockout cystinotic (C*tns*$^{-/-}$) recipients (Rocca et al., 2015), a model which develop comparable disease complications than the cystinosis patients (Nevo et. al., 2010; Kalatzis et al., 2001). After bone marrow reconstitution, HSPC progeny engrafted into all organs, and cystine was significantly decreased across all tissues (Harrison et. al., 2013). We observed morphological preservation of the kidney, cornea, and thyroid for the lifespan of WT HSPC recipients, indicating that a single HSPC transplantation appears to be an effective therapy preventing cystinosis disease progression in the mouse (Yeagy et al., 2011). Studying the mechanism of action revealed that HSPCs differentiate into macrophages and are able to

deliver cystinosin-bearing lysosomes to the diseased cells via tunneling nanotubes (TNTs) (Rocca and Cherqui 2019; Goodman et al., 2019). Based on these promising data, we have initiated a Phase I/II clinical trial translating this strategy to human cystinosis patients, where patients' HSPCs are genetically modified *ex vivo* using a lentiviral vector containing functional *CTNS* prior to being reintroduced into the myleoablated patient (ClinicalTrials.gov Identifier: NCT03897361).

One concern with moving this strategy into humans lies in the nature of the most common disease-causing mutation; a large 57 kilo base pair (kb) deletion spanning not only the entire *CTNS* gene, but also the neighboring sedoheptulokinase (*SHPK)* locus (Touchman et al., 2000). Sedoheptulokinase (*SHPK*), formerly known as carbohydrate-like kinase (*CARKL*), is metabolic regulatory enzyme found in the non-oxidative arm of the pentose phosphate pathway (PPP) that supplies carbon substrates for glycolysis (Nagy and Hashemi 2013). In an ATP-dependent fashion, *Shpk* generates sedoheptulose-7-phosphate (S7P), both a product and substrate of glucose metabolism. Via this contribution to metabolic flux, *Shpk* is a critical regulator of macrophage polarization and differentiation (Haschemi et. al., 2012). As roughly 40% of human patients carry the 57-kb deletion in the homozygote state and so do not express *SHPK*, coupled with the fact that tissue rescue by HSPC transplantation relies upon their differentiation into macrophages (Goodman et. al., 2019), we had to investigate any therapeutic impact of *SHPK*-deficient HSPCs for cystinosis. Understanding *SHPK* in this context is critical to determine if patients carrying the 57-kb deletion at the homozygote state could be enrolled in the ongoing clinical trial.

In this present study, we seek to address the impact of *Shpk* in the therapeutic efficacy of HSPC transplantation. We generated and characterized two novel *Shpk*-deficient mouse models and observed reduction in mRNA and protein expression, as well as a mild metabolic phenotype consisting of perturbation of PPP metabolites in the liver and urine. Transplantation of *Shpk*$^{-/-}$ HSPCs into cystinotic mice (*Ctns*$^{-/-}$*Shpk*$^{+/+}$) retained the ability of rescuing cystinosis as assessed by cystine accumulation, *Ctns* expression and renal function. Therefore, cystinosis patients lacking *SHPK* are equally likely to receive therapeutic benefit from autologous transplantation of gene-modified HSPCs and will be enrolled in the clinical trials.

3.2: Results

Generation and Characterization of novel Shpk knockout mouse models. Rudimentary documentation revealing the metabolic regulatory and immunomodulating capacity of sedoheptulokinase (*SHPK)* (Haschemi et. al., 2012) may present implications in the pathological progression and efficacy of stem cell-based immunotherapy of cystinosis, respectively, that have yet to be deduced. Therefore, we generated novel Shpk-knockout (*Shpk*$^{-/-}$) mouse models used to: 1) evaluate the isolated consequences of *Shpk*-deficiency in the clinical presentation of cystinosis and 2) determine if *Shpk* is required for effective HSPC transplantation therapy to mimic the genotypes of patients harboring the 57-kb deletion eliminating *SHPK* at the homozygotic state.

Two murine mutants were developed to independently validate findings using CRISPR-Cas9 editing creating heritable homozygous indels via non-homologous genomic end-joining. We generated the first *Shpk*$^{\Delta ATG}$ strain with CRISPR guides targeting the transcriptional site of the *Shpk* transcript in C57BL/6 mice (Fig. 3.1a). PCR-based genotyping assays and Sanger sequencing of 15 potential knockout offspring yielded one heterozygous male founder with a frameshift mutation constituting bi-allelic 168-bp deletions of coding and non-coding regions that included the first 38 BP of *Shpk* (Fig. 3.1b). The second *Shpk*$^{\Delta E2}$ strain, provided by UC Davis, harbored deletions spanning exon 2 of the *Shpk* gene. PCR genotyping assays using a specialized 3-part primer and Sanger sequencing indicated a 675-bp elimination surrounding exon 2 (Supplementary File 2, Fig. 1). Each mouse line was independently bred to homozygosity, as sequencing confirmed Mendelian segregation of 50% heterozygous F1 offspring from respective founders and WT C57BL/6 mice breeding and 25% homozygous F2 offspring from F1 crossbreeding (Supplementary File 2, Fig. 1). Furthermore, *Shpk*$^{\Delta ATG}$, *Shpk*$^{\Delta E2}$, and cystinotic (*Ctns*$^{-/-}$) were crossbred with DsRed$^{+/+}$ C57BL/6 mice to generate both no-color and fluorescently-labeled mouse lines utilized in subsequent experiments evalauating transplantation outcomes.

Following genomic characterization of both *Shpk*$^{-/-}$ mice, we assessed molecular (RNA and protein) expression in *Shpk*$^{-/-}$ tissue as a comparative measure of knockout efficacy with respect to the altered

genomic loci of *Shpk* in each mouse model. Human tissues with high *SHPK* mRNA expression include liver, kidney, pancreas, and heart (Nagy and Haschemi 2013). Reverse transcription-quantitative PCR (RT-qPCR) quantitation of murine *Shpk* mRNA expression indicated significant reduction in *Shpk* mRNA transcription across these tissues in $Shpk_{\Delta E2}$ mice, while $Shpk_{\Delta ATG}$ mice retained variable degrees of RNA transcription (Fig. 3.1c). On the protein level, immunoblotting of $Shpk^{-/-}$ tissues revealed that changes in expression of *Shpk* protein (~57 kDa) appeared tissue function-specific. As such, *Shpk* expression was detected mainly in the highly metabolic liver (Fig. 3.1d; Supplementary File 2, Fig. 2) and (kidney Supplementary File 2, Fig. 2) of WT and $Ctns^{-/-}$ mice, which was notably diminished in both $Shpk_{\Delta E2}$ and $Shpk_{\Delta ATG}$ mice, quantitatively confirmed by densitometry analysis relative to tubulin (Fig. 3.1d); non-metabolic tissues heart, spleen, brain, muscle, and eye did not exhibit *Shpk* protein expression in both knockouts (Supplementary File 2, Fig. 2). Of note, $Shpk_{\Delta ATG}$ mice presented the inconsistent molecular profiles of variable RNA expression, yet eliminated protein expression. Nevertheless, while transcriptional discrepancies exist between both $Shpk^{-/-}$ mouse models, they both maintain the capacity for successful translational impairment of *Shpk* gene.

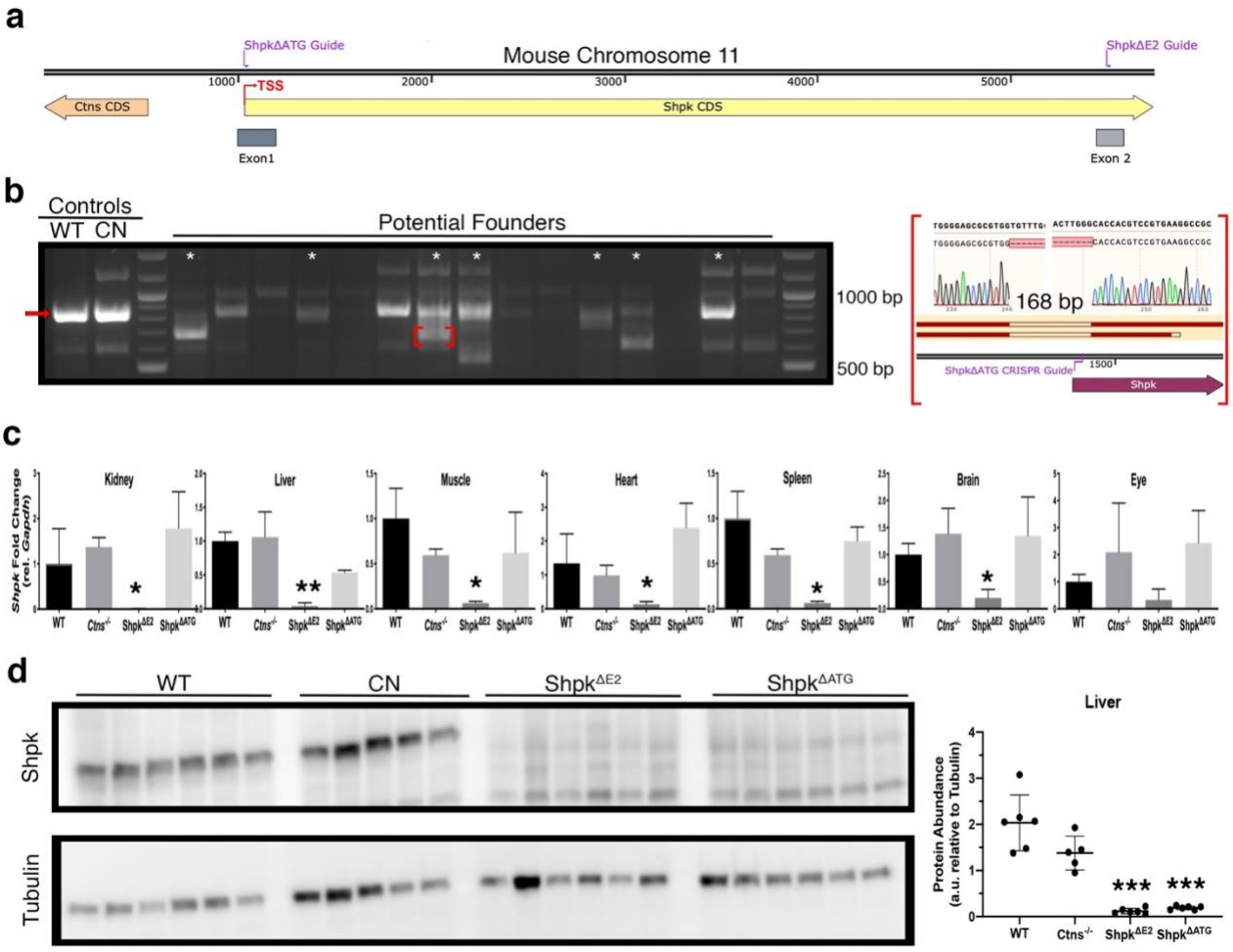

Figure 3.1: Genomic, RNA, and protein characterization of Shpk knockout mouse models. **(a)** Diagram of the mouse genomic region between *Ctns* and *Shpk.* CRISPR-Cas9 guides depicted at start codon (Shpk*ΔATG*) or second exon (Shpk*ΔE2*). **(b)** Generation of *Shpk*$^{\Delta ATG}$ mouse line with CRISPR-CAS9 targeting of the start codon (*Δ*ATG) of *Shpk* gene in mouse blastocysts. Genotyping-based PCR assay used to identify potential homozygote knockouts. Genomic sequencing of select homozygotes revealed 168 BP genomic deletion that includes the first 38 BP of *Shpk* transcript. **(c)** Bar graphs depicting *Shpk* mRNA expression relative to housekeeping control *GapDH* gene across several tissue in WT, *Ctns*-knockout (*Ctns*$^{-/-}$), *Shpk*$^{\Delta ATG}$, and *Shpk*$^{\Delta E2}$ mice measured over 3 transplant groups. *Shpk* mRNA expression normalized to WT. **(d)** Immunoblots and quantitation visualizing *Shpk* protein expression (~51 kDa) in the liver of WT (n=6), *Ctns*$^{-/-}$ (n=5), *Shpk*$^{\Delta ATG}$ (n=6), and *Shpk*$^{\Delta E2}$ (n=6) mice. *Tubulin* protein used as loading control and for quantitation normalization. All graphs shown as mean ± SD. Stars depict significant difference relative to WT. Full uncropped westerns shown in Supplementary Figure 2. P values determined by one-way ANOVA or student's t-tests. *P < 0.05, **P < 0.01.

Elucidating a mild metabolic phenotype by consequence of Shpk-deficiency. We investigated pathological phenotypes of our *Shpk*$^{-/-}$ mouse models following *Shpk* genomic elimination and molecular impairment. Phosphorylation of sedoheptulose into sedoheptulose-7-phosphate (S7P) by *Shpk* enzymatic activity is a rate-limiting factor for carbon effluxes in glucose metabolism (Fig. 3.2a). Therefore, we performed pentose phosphate pathway (PPP) metabolomics via mass spectometry on *Shpk*$^{-/-}$ livers isolated from both mouse models to investigate potential metabolic phentoypes. We measured changes in relative abundance of the following metabolites given their respective relevance to *Shpk* enzymatic function: S7P, direct indicator of *Shpk* loss-of-function; erythrose-4-phosphate (E4P), a precursor biomolecule to erythritol, which is found at high urininary concentrations in patients with cystinosis and *SHPK*-Deficiency (SHPKD) (Wamelink et. al., 2015); and upstream PPP intermediates ribose-4-phosphate (R4P), xylose-4-phopshate (X4P), and 6-phosphogluconate (6PG), contributors to *SHPK* metabolism (Fig. 3.2a). Metabolite relative abundance calculated the peak area ratio of PPP metabolites normalized to combined WT and *Ctns*$^{-/-}$ control averages, due to both harboring *Shpk*$^{+/+}$ genotypes. We observed significant reductions in S7P abundance, as well as dysregulation of all PPP metabolites except E4P in both *Shpk*$^{\Delta ATG}$ and *Shpk*$^{\Delta E2}$ mice (Fig. 3.2b).

Furthermore, since patients of both 57-kb cystinosis or isolated SHPKD harbor urinary metabolic phenotypes, we examined the metabolic consequences of *Shpk*-deficiency in the urine of both *Shpk*$^{-/-}$ mice. Preliminary urine metabolomics appear to indicate elevated levels of sedoheptulose and erythritol compared to WT and *Ctns*$^{-/-}$ controls, enhancing the metabolic profile of murine *Shpk*, independent of cystinosis (further testing is required to determine statistical significance) (Fig. 3.2c). In both metabolic tests, no significant differences were observed between *Shpk*$^{\Delta ATG}$ and *Shpk*$^{\Delta E2}$ mice. No dysregulation of non-PPP metabolites in the liver was observed (Supplementary File 2, Fig. 3). Thus, coupled with preceding molecular conclusions, these data affirm a metabolic phenotype as a consequence of *Shpk*-deficiency in both *Shpk*$^{-/-}$ mice. Most importantly, in response to the unknown clinical contributions of *Shpk* in the heterogeneity of cystinosis, our *Shpk*$^{-/-}$ models serve as the first murine indicators recapitulating *in vitro* and human clinical findings that isolate metabolic phenotype to *Shpk*-deficiency, suggesting *Shpk* a mild metabolic contribution to the clinical heterogeneity of cystinosis (Wamelink et. al., 2008).

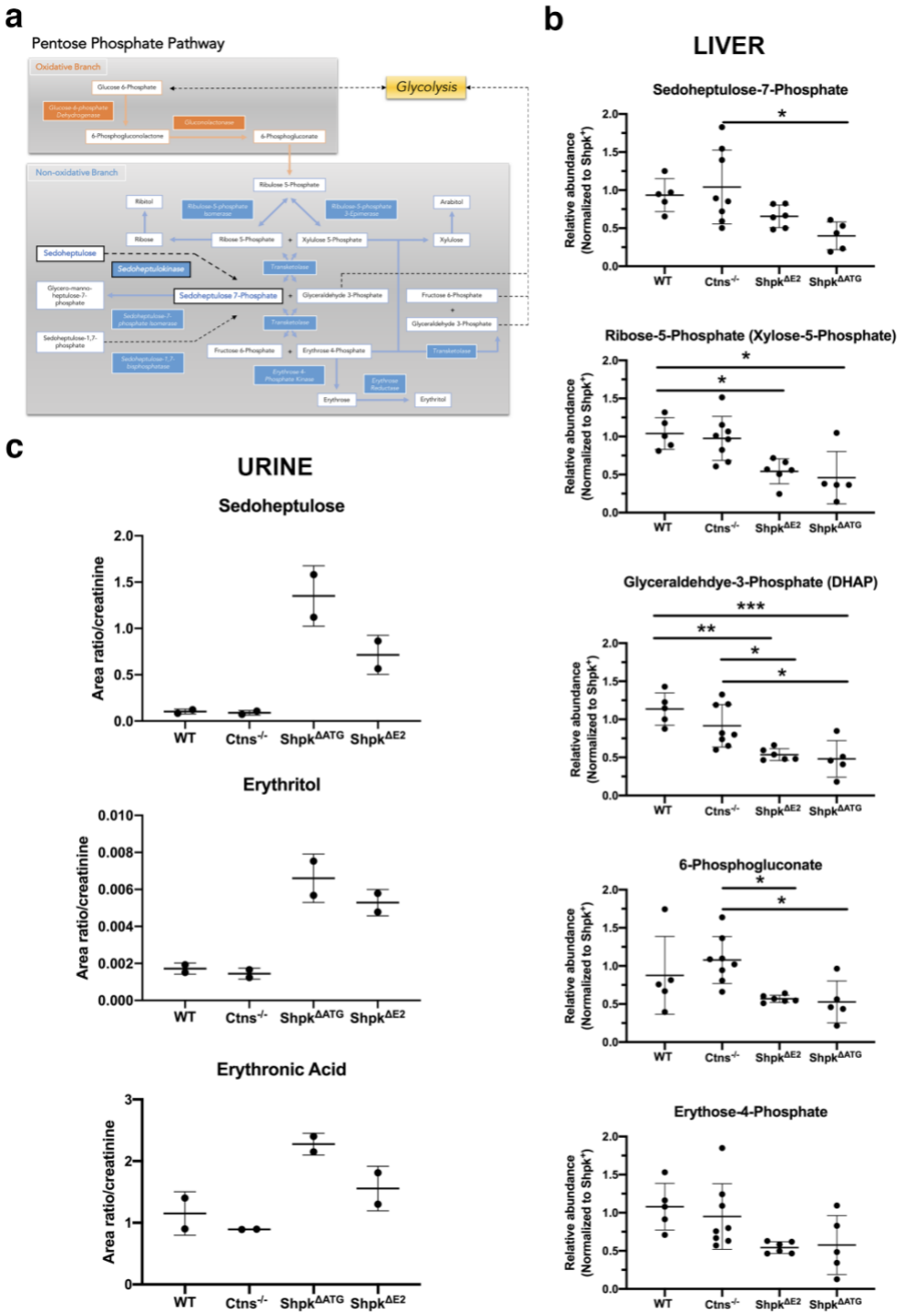

Figure 3.2: Metabolic phenotype of Shpk-/- mouse models. **(a)** Schematic of the pentose phosphate pathway (PPP) illustrating *SHPK* metabolism of implicated metabolites. **(b)** Mass spectrometry quantitation of PPP metabolite relative abundance in WT (n=5), *Ctns*$^{-/-}$ (n=8), *Shpk*$^{\Delta ATG}$ (n=6), and *Shpk*$^{\Delta E2}$ (n=5) livers. **(c)** Mass spectrometry preliminary quantitation of urinary metabolic content as a consequence of Shpk-deficiency in WT (n=2), *Ctns*$^{-/-}$ (n=2), *Shpk*$^{\Delta ATG}$ (n=2), and *Shpk*$^{\Delta E2}$ (n=2) livers. Substrates are directly affected by Shpk enzymatic activity. All graphs shown as mean ± SD. P values determined by one-way ANOVA or student's t-tests. *$P < 0.05$, **$P < 0.01$, ***$P < 0.001$.

Shpk-deficient HSPC transplantation reduces cystine load and restores Ctns mRNA expression across multiple tissues of recipient cystinotic mice. Following generation and characterization of *Shpk*$^{-/-}$ mice, we examined therapeutic success as mediated by donor *Shpk*$^{-/-}$ HSPC transplantation into recipient cystinotic mice. Sca1^{+} HSPCs were immunomagnetically obtained from donor WT, *Ctns*$^{-/-}$, *Shpk* $^{\Delta TG2}$ and *Shpk* $^{\Delta E2}$ bone marrow and transplanted into lethally-irradiated recipient cystinotic (*Ctns*$^{-/-}$/*Shpk*$^{+/+}$) mice. Six months post-transplantation, we investigated *Ctns* mRNA restoration, cystine reduction, tissue morphological rehabilitation, renal improvements, and donor cell tissue integration and identification in cystinotic recipient tissues.

Recovery of *Ctns* mRNA expression and diminished cystine buildup are critical assessors of stem cell gene therapy capacity (Harrison et. al., 2013). *Ctns* mRNA expression was measured using RT-qPCR on recipient tissue RNA. While *Ctns* mRNA expression was ablated in *Ctns*$^{-/-}$ HSPC recipients, we observed that WT, *Shpk* $^{\Delta ATG}$, and Shpk $^{\Delta E2}$ HSPCs restored expression in transplanted *Ctns*$^{-/-}$ liver spleen, and kidney (Fig. 3.3a). As a functionality measure of exogenous *Ctns* protein expression, cystine content was measured via mass spectrometry in the liver, spleen, muscle eye, and kidney of cystinotic recipient mice. Non-transplanted WT, WT-HSPC recipients and *Ctns*$^{-/-}$-HSPC recipients were used as controls; as previously reported by Harrison et al., WT HSPCs decreased cystine content compared to *Ctns*$^{-/-}$ HSPCs controls across all tissues except male kidney, and *Ctns*$^{-/-}$ recipients retained cystinotic conditions (Fig. 3.3b). Cystinotic recipients of *Shpk* $^{\Delta E2}$ HSPCs showed significant reduction of cystine content in the liver, spleen, muscle, eye and female kidney; recipients transplanted with *Shpk* $^{\Delta ATG}$ HSPCs showed improved cystine levels in muscle and eye. Kidney cystine measurements were separated by gender, due to reports of female kidneys generally exhibiting higher cystine levels than that of male kidneys (Harrison et. al., 2013). While male kidneys did not show significant differences between controls and *Shpk*$^{-/-}$ HSPCs, likely due to minimal availability of technical replicates, cystine depletion was statistically significant in female kidneys transplanted with *Shpk* $^{\Delta E2}$ HSPCs (Fig. 3.3b). Taken together, *Shpk*$^{-/-}$ HSPCs appear capable of emulating WT HSPC-mediated disease rescue of two primary pathological markers of cystinosis – exogenous restoration cystinosin protein supply and subsequent alleviation of cystine content.

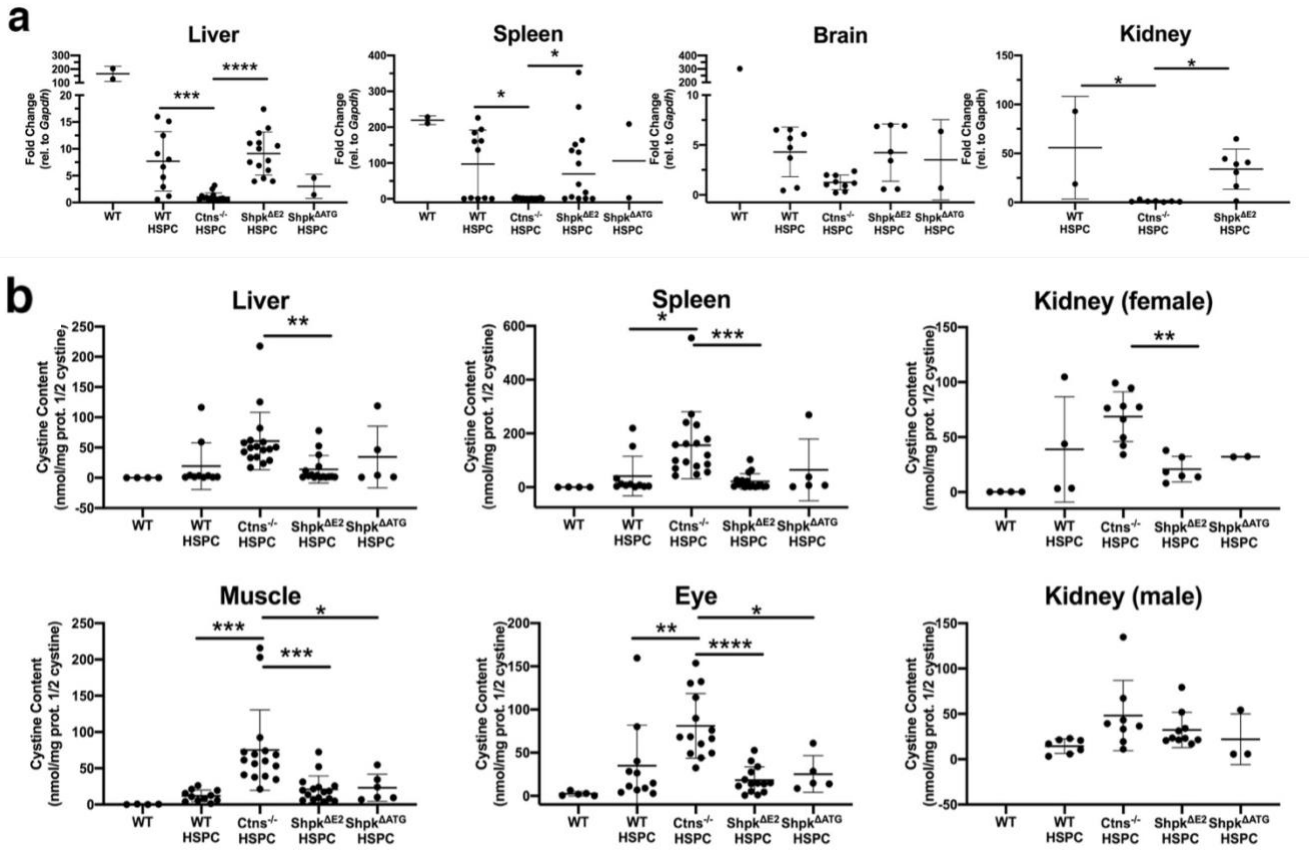

Figure 3.3. Cystinosin molecular and functional restoration following Shpk$^{-/-}$ HSPC transplantation in recipient Ctns$^{-/-}$ mice. **(a)** Histograms depicting RT-qPCR quantitation of *Ctns* mRNA expression across several tissue following transplantation of WT (n=1-2), *Ctns*$^{-/-}$ (n=9), *Shpk* $^{\Delta E2}$ (n=6-14), and *Shpk* $^{\Delta ATG}$ (n=2; not kidney) HSPCs in cystinotic mice. mRNA expression measured relative to housekeeping control GapDH gene and *mCtns* expression normalized to transplanted *Ctns*$^{-/-}$ HSPCs. **(b)** Graphs depicting mass spectrometry analysis of cystine availability following transplantation of WT (n=4-5; no male kidney), WT HSPC (n=4-11) *Ctns*$^{-/-}$ HSPC (n=13-16), *Shpk* $^{\Delta E2}$ HSPC (n=6-14), and *Shpk* $^{\Delta ATG}$ HSPC (n=2-5) HSPCs. Non-transplanted WT mice used as controls. Cystine content normalized to total protein quantitated via BCA assay. Points represent individual mice across multiple transplantation groups. All graphs shown as mean ± SD. P values determined by one-way ANOVA or student's t-tests. *P < 0.05, **P < 0.01, ***P < 0.001, ****P < 0.0001.

Tissue Morphological Preservation Faculty of transplanted Shpk-deficient HSPCs in recipient cystinotic mice. Histopathology analysis of the kidney section was performed using a blinded scoring system previously described and performed by a certified pathologist (Yeagy et al., 2011). We observed that tissue morphology is especially susceptible to irradiation required for HSPC transplantation, so we separately considered the untreated and *Ctns*$^{-/-}$ HSPC cystinotic recipients. Regarding the extent of cortical damage, significant reductions in the severity of the kidney damage in WT and *Shpk*$^{-/-}$ HSPC *Ctns*$^{-/-}$ recipients as compared to *Ctns*$^{-/-}$ HSPCs recipients were observed (Figure 3.4). Glomerulosclerosis, dilated or atrophic convoluted proximal tubules, thickening of the basement membranes, protein casts, and mononuclear infiltrates were reported in all transplanted mice, but at different degree among the multiple transplant groups, appearing most frequent in the *Ctns*$^{-/-}$ HSPC recipients. Thus, WT and both *Shpk*$^{-/-}$ HSPCs appear to enact a protective effect on kidney morphological structure as opposed to *Ctns*$^{-/-}$ HSPCs in cystinotic mice. In addition, foci of inflammation or mononuclear perivascular cuffs were observed in the lungs of some of the *Ctns*$^{-/-}$ mice, and yet again most commonly in *Ctns*$^{-/-}$ recipients (Supplementary File 2, Fig. 5).

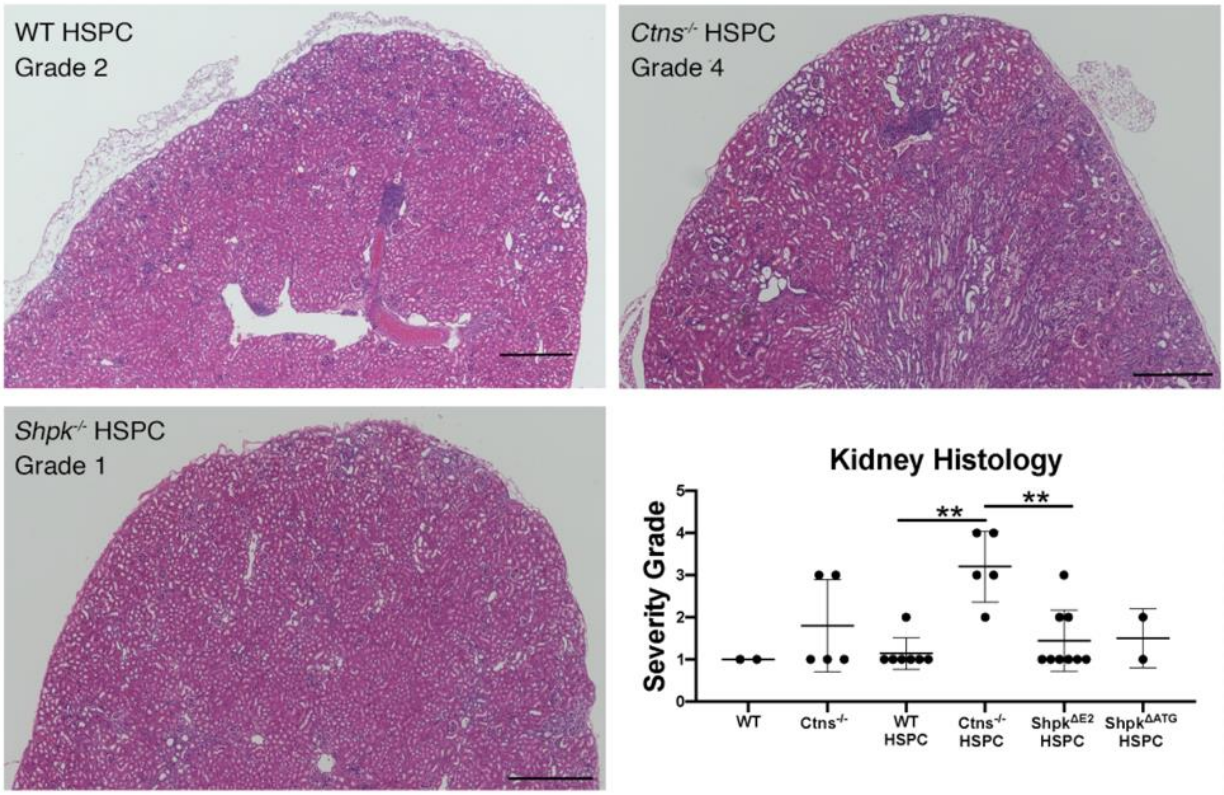

Figure 3.4. Transplantation of Shpk$^{-/-}$ HSPCs into recipient Ctns$^{-/-}$ mice preserves kidney morphology. Sample representative H&E images depicting kidney morphology in mice 6-months post-transplant. WT HSPC (n=7), *Ctns*$^{-/-}$ HSPC (n=5), *Shpk* $^{\Delta E2}$ HSPC (n=9), and *Shpk* $^{\Delta ATG}$ HSPC (n=w) samples were compared to untransplanted WT (n=2). Points represent individual mice across multiple transplantation groups. Samples are graded blind based on cortical damage – see Methods for details. Error bars represent standard deviation. Scale bars = 50 μm. * $P<0.05$, ** $P<0.01$.

Shpk-deficient HSPC transplantation normalizes renal function in recipient cystinotic mice. Hallmark physiological afflictions constitute early renal Fanconi syndrome and chronic kidney deterioration. Thus, therapeutic resolution by *Shpk*$^{-/-}$ HSPC transplantation into cystinotic mice was ultimately determined by renal function improvements based on renal markers measured in urine and plasma serum. While mixed genetic background *Ctns*$^{-/-}$ mice initially did not present tubulopathy or renal failure, congenic C57BL/6 *Ctns*$^{-/-}$ crossbreeds showed loss of biochemical and protein Fanconi syndrome markers: glucosuria, creatininurea, phosphaturia, and urea (Nevo et al., 2010), as well as proteinuria of intermediate molecular weight (IMW) proteins such as transferrin (Gaide Chevronnay et al., 2014). In this pursuit, we tested compounds creatinine, creatinine clearance, phosphate, glucose, and urea in 24-hour urine collections and cystatin C in retro-orbitally obtained serum six-months post-transplantations. While we did note that healthy WT mice had a significantly higher body mass than all groups of cystinotic HSPC recipients, there were no specific differences between any transplant groups (Supplemental File 2, Fig. 4a). Furthermore, creatinine clearance, phosphate, urea and proteinuria appeared normal urine, as well as Cystatin C in the serum (Supplemental File 2, Fig. 4b-f). However, we observed glucosuria in cystinotic recipients of *Ctns*$^{-/-}$ HSPCs that was resolved to untransplanted WT levels in recipients of WT, *Shpk* $^{\Delta E2}$, and *Shpk* $^{\Delta ATG}$ HSPCs (Fig. 3.5a). Blood chemistry analysis did not reveal any significant differences between the HSPC-transplanted groups (Supplemental File 2, Tables 2). Analysis of complete blood counts (CBC) revealed minor differences between the percentage of lymphocytes and monocytes between individual transplant groups, but values were always within normal range for C57 BL/6 mice, indicating that transplantation of Shpk-deficient stem cells did not specifically alter normal hematopoiesis (Supplemental File 2, Table 3). Taken together, these data suggest gradual degradation of the renal phenotypes in cystinotic mice, yet partial proximal tubular phenotypes can be corrected by Shpk-/- HSPCs. Ultimately, our *Shpk*$^{-/-}$ HSPC transplantation system is the first mouse model of cystinosis to demonstrate the partial pathophysiological restoration of cystinotic renal dysfunction, thus indicating the therapeutic index of stem cell gene therapy of cystinosis is unperturbed by *Shpk*-deficiency.

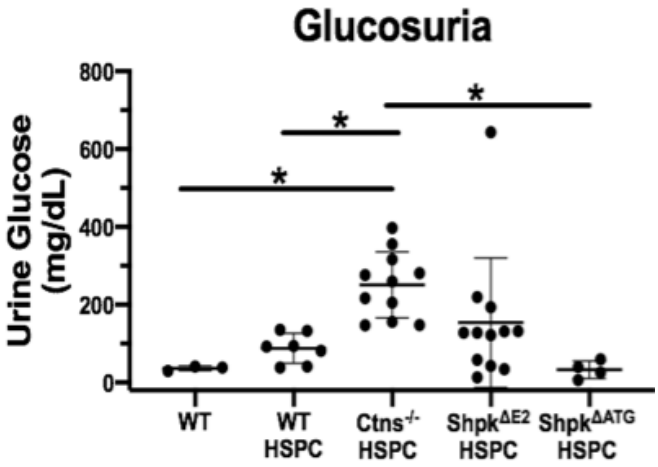

Figure 3.5. Renal function recovery measured in urine of recipient Ctns*$^{-/-}$ *mice following Shpk*$^{-/-}$ *HSPC transplantation. **(a)** Histogram measuring glucose urinary concentrations in recipient mice six months post-transplantations of WT HSPC (n=7), *Ctns*$^{-/-}$ HSPC (n=11), *Shpk* $^{\Delta E2}$ HSPC (n=12), and *Shpk* $^{\Delta ATG}$ HSPC (n=4) compared to untransplanted WT (n=3). Urine samples were collected over 24 hours and treated with protease/phosphatase inhibitors. Points represent individual mice across multiple transplantation groups. Error bars represent standard deviation. All graphs shown as mean ± SD. P values determined by one-way ANOVA or student's t-tests. *$P < 0.05$.

Transplanted Shpk-deficient HSPC progenies capable of tissue integration and differentiation into immune cells in recipient cystinotic liver. Since HSPC differentiation bears blood cells, we evaluated tissue integration and progeny identification of DsRed-labeled donor *Shpk*$^{-/-}$ cells in no-color recipient tissue environments using immunofluorescence. Confocal microscopy was used to visualize DsRed^{+} HSPC signaling in recipient liver, indicating tissue integration of engrafted donor cells (Fig. 3.4). Given that intracellular trafficking of cargo is facilitated by HSPC-derived tissue-resident macrophages, we stained recipient tissues with antibodies for macrophage markers CD68 (general macrophage marker), F4/80 (Kupffer cell-specific marker), and MHCII (dendritic cell-specific marker) to establish engrafted donor blood cell lineage identity. Livers transplanted with *Shpk* $^{\Delta E2}$ HSPCs carry consistent overlap between all three markers (green) and donor HSPC-derived cells (red). Therefore, HSPC progenies were identified as differentiated macrophages due to co-localization of donor cell DsRed signaling with macrophage markers in the liver. Taken together, these data indicate that *Shpk*-deficiency does not hinder macrophage differentiation and tissue integration capacity of donor HSPC progenies in cystinotic mice.

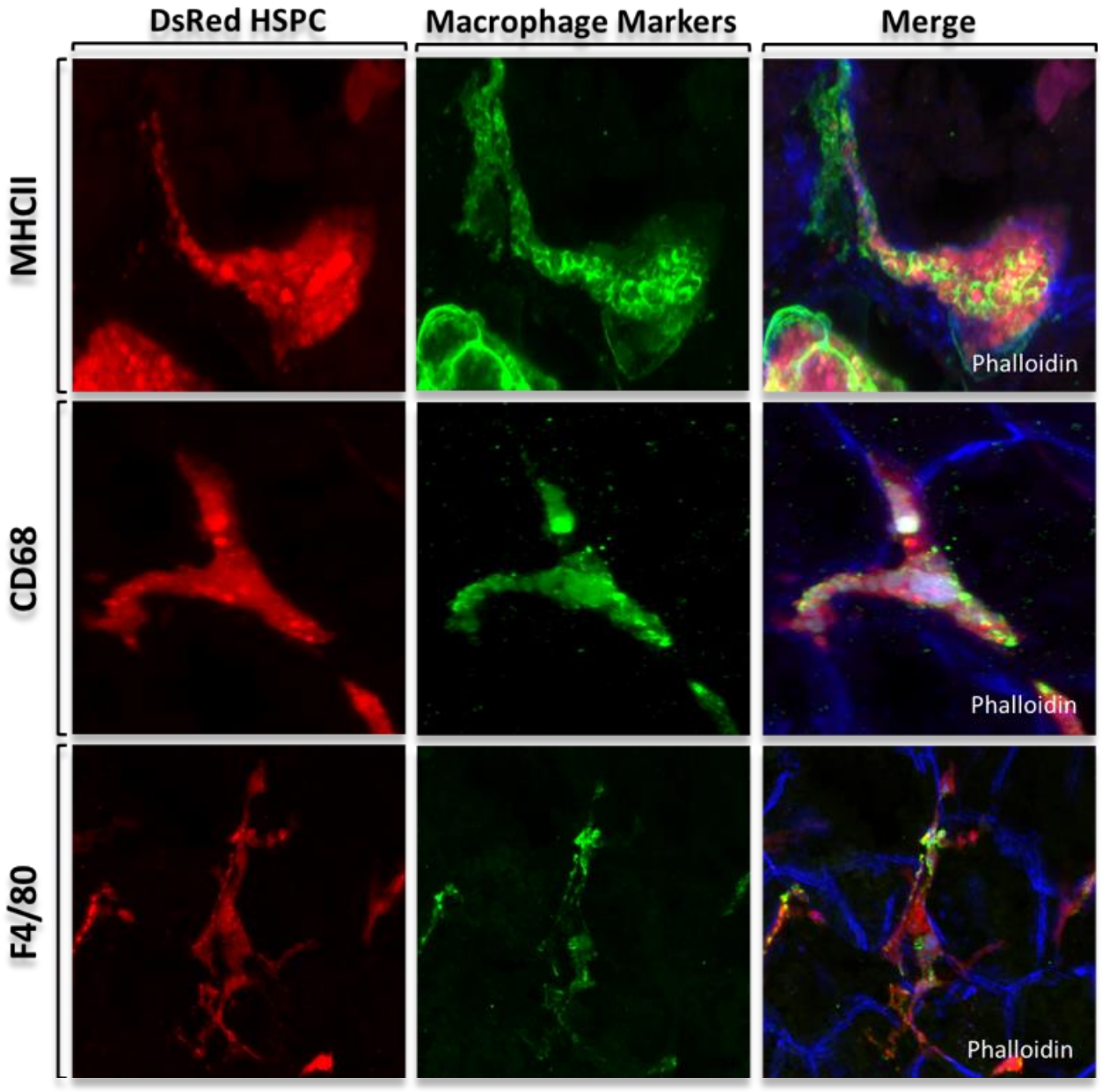

Figure 3.6. Transplanted Shpk$^{-/-}$ HSPC progeny engraftment and identification in recipient Ctns$^{-/-}$ tissue. **(a)** Confocal images showing co-localization between transplanted DsRed$^{+/+}$ *Shpk* $^{\Delta E2}$ HSPCs (red) and macrophage markers MHCII, CD68, and F4/80 (GFP; green) in recipient *Ctns*$^{-/-}$ livers. F-actin visualized via phalloidin staining shown in blue. Scale bars = 100 um. F-actin visualized via phalloidin staining shown in blue. Scale bars = 100 um.

3.2: Discussion

Summary of Findings. The present study explored the clinical relevance of sedoheptulokinase (*SHPK*) gene to the hematopoietic stem cell therapy for cystinosis by consequence of the most prevalent 57-kb homozygous mutation spanning both *CTNS* and contiguous *SHPK* genes. Given *SHPK* metabolism has been identified as a key regulator of macrophage polarization, it was unknown if the utility of HSPC-derived macrophage-based gene therapy will benefit *SHPK*-deficient patients with cystinosis. To confirm that the therapeutic application can be extended to all patients in ongoing clinical trials, we evaluated *SHPK* in two contexts: (1) contribution to the heterogeneity of the disease and (2) impact on therapeutic efficacy of HSPC-derived macrophage-mediated gene therapy for the disease.

Homozygous *SHPK*-Deficiency (SHPKD) causes mild perturbation of PPP metabolites in murine macrophages *in vitro* (Haschemi et. al., 2012), as well as urinary accretion of erythritol (Kardon et. al., 2008) and sedoheptulose (Wamelink et. al., 2008) in 57-kb mutated cystinosis and isolated SHPKD patient profiles (Wamelink et. al., 2014). However, literature acknowledged the lack of clear delineation of *SHPK*-deficiency accounting for the clinical heterogeneity of the disease. To analyze the isolated clinical consequences of *SHPK*-deficiency for cystinosis *in vivo*, we generated two novel *Shpk* knockout (*Shpk*$^{-/-}$) mice with normal *Ctns*$^{+/+}$ expression and probed for functional phenotypes. After molecular characterization confirmed genomic eliminations, we observed PPP intermediate dysregulation in the liver, as well as elevated sedoheptulose and erythritol urinary concentrations in both *Shpk*$^{-/-}$ mouse models. Recapitulating previous findings of a mild, yet consistent metabolic phenotype, this data further independently suggests that homozygous *SHPK* deletions may minimally contribute to the clinical heterogeneity of cystinosis.

We have previously demonstrated that transplanted HSPC-differentiated macrophages preferentially adopt a pro-inflammatory M1-like polarization state – which is inversely modulated by *SHPK* gene expression (Haschemi et. al., 2012) – for lysosomal intercellular trafficking *in vivo* (Goodman et. al., 2019). Thus, it is critical to investigate the impact of *Shpk* absence on differentiation and lysosomal

trafficking capacity of HSPC-derived tissue-resident macrophages following transplantation. We confirmed widespread disease rescue indicated by reduction in cystine levels, restoration of *Ctns* mRNA expression, and morphological preservation across several tissue, as well as renal function improvement in cystinotic mice. We also showed that transplantation of donor HSPCs isolated from *Shpk*$^{-/-}$ mice into recipient cystinotic mice resulted in successful engraftment of donor cells and progeny identification as a variety of tissue-resident macrophages. Taken together, our novel HSPC gene therapy retains therapeutic efficacy for all patients even the patients carrying the 57-kb deletion at the homozygote state.

Analyses of Findings. Previous characterization of cystinosis murine homologs solely evaluated the consequences of *Ctns*-deficiency (Cherqui et. al., 2002), but did not mimic the predominant cystinosis mutation genotype (*CTNS*$^{-/-}$/*SHPK*$^{-/-}$). We report the first CRISPR-generated *Shpk*$^{-/-}$ (with normal *Ctns*$^{+/+}$ gene expression) mice models with deletions at two different loci of murine Shpk to comparatively investigate the genetic underpinnings of *Shpk* in the context of cystinosis. We unexpectedly discovered that while *Shpk*$^{\Delta E2}$ mouse showed consistent genomic, molecular, and metabolic perturbations, the *Shpk*$^{\Delta ATG}$ mouse model appeared to sustain transcriptional capabilities. It was, indeed, surprising that deletions of the start codon in the *Shpk*$^{\Delta ATG}$ mouse model were evaded elimination of *Shpk* RNA, yet significantly reduced *Shpk* protein (Fig. 3.1c,d). Preservation of protein translation and metabolic activity could be explained by internal genomic and/or molecular nuances that mechanistically evaded the start codon deletion, such as the presence of an active internal methionine (ATG) site in the coding region of *Shpk* by virtue of frameshift mutation. Molecular feedback loops may also play a role in preserving *Shpk* expression: functional protein may not be produced without whole transcription of exonic coding regions as seen in our data, but may upregulate RNA transcription in response to decreased protein translation. While these genomic and molecular nuances remain to be determined, HSPCs isolated from both *Shpk*$^{-/-}$ mice remained capable of disease rescue following transplantation into cystinotic mice.

One particularly interesting finding is that our mouse models effectively recapitulate urinary accumulation of the PPP metabolites erythritol and sedoheptulose (Fig. 3.2c). It has been hypothesized that cystinosis patients with the 57-kb deletion have *SHPK*-deficiency (SHPKD) based on elevation of the compounds such as sedoheptulose and erythritol (Wamelink et al., 2008, Kardon et al., 2008). Wamelink *et al.* reported in 2015 that two unrelated patients presented isolated cases of *SHPK-deficiency* with strongly elevated urinary PPP metabolites; however, due to their variable and inconsistent clinical profiles, attribution of this phenotype to *SHPK* deletion specifically remained inconclusive. Our discovery that only *Shpk*, but not *Ctns*, knockout mice demonstrate the known metabolic phenotype provides further independent evidence supporting the hypothesis that the loss of *SHPK* itself in patients does have a detectable effect and may contribute to a small degree to the clinical heterogeneity of cystinosis (Wamelink et al., 2015). Furthermore, while increased urinary sedoheptulose can be directly attributed to *SHPK*-deficiency in patients, the metabolic mechanism for erythritol elevation in urine remains unclear. Previous studies have proposed that elevated sedoheptulose becomes a substrate for fructokinase catabolism to produce erythrose which is further reduced to erythritol (Kardon et al., 2008, Wamelink et al., 2008). Future elucidation of the metabolic mechanisms surrounding functional loss of *Shpk* independent of cystinosis can be further explored using our *Shpk*$^{-/-}$ mouse models.

In pursuit of comprehensive metabolic profiling of *SHPK*, Dr. Haschemi previously analyzed the effects of LPS-induced pro-inflammatory stimulation on metabolic activity of murine RAW 264.7 macrophages with altered *SHPK* expression, finding a general increase of PPP metabolites R5P, X5P, and G3P, and a decrease in S7P (Haschemi et al., 2012). Metabolomics of *Shpk*$^{\Delta E2}$ and *Shpk*$^{\Delta ATG}$ livers revealed the opposite metabolite perturbation trend except for S7P (Fig. 3.2b). We also did not detect any changes in the polarization profiles of either unstimulated BMDMs or peritoneal macrophages derived from our *Shpk* knockout mice (Supplementary File 2, Fig. 6). Taken together with urine metabolomics, free-flowing sedoheptulose only enters the catabolic pathway if phosphorylated into S7P (Nagy and Haschemi 2013); thus, in the absence of functional *Shpk*, we found increased excreted sedoheptulose and lowered converted S7P concentrations in the liver. However, decreases in R5P, G3P, 6-PG, and E4P in response to *Shpk*-

deficiency in tissue once again reiterates that within *in vivo* environments, the functional regulation of *Shpk* may be context-dependent (Nagy and Haschemi 2015), such as feedback inhibition, metabolic and/or cellular constraints, or alternative enzymatic supply of metabolites. We postulate that since S7P phosphorylation is known to be a rate-limiting carbon-flux rheostat (Nagy and Haschemi 2015), limited supply of S7P may decrease its G6P-conjugated conversion into F6P and E4P within the liver. In addition, previous studies noted the uncertainty surrounding quantitative contribution of *Shpk*-mediated supply of S7P for the PPP (Nagy and Haschemi 2013). In both *Shpk*$^{-/-}$ models, the permanence in metabolite dysregulation suggests that *Shpk*-mediated supply of S7P is a more critical regulatory shunt of the PPP than previously anticipated. Ultimately, these differences may be explained by the functional dichotomy of *in vitro* and *in vivo* models: *in vivo* susceptibility to physiological nuances unaccounted for in controlled *in vitro* conditions. For example, Dr. Haschemi's *in vitro* experiments involved LPS-stimulation of M1 polarization of macrophages which caused metabolic dysregulation; our *in vivo* metabolomics did not involve stimulation of M1-like polarization of macrophages, yet still sustained a metabolic phenotype. A previous study related macrophage inflammation and systemic metabolism in hyperglycemia: high cholesterol inhibits PPP activity, including R5P and S7P, which reduces LPS-activated high-fat diet (HFD) peritoneal macrophage inflammatory response (Baardman et. al., 2018). Given hyperglycemia is a symptom of cystinosis, which was recapitulated in our cystinotic mouse models and rescued by WT and *Shpk*$^{-/-}$ HSPC transplantations, this further supports the notion that *in vivo* environments offer effective human physiological remodeling.

Lastly, clinical examination of patients with cystinosis has revealed increased sedoheptulose in dried bloodspots (Wamelink et. al., 2011), but consequences in tissue metabolism remains unknown as obtaining human tissue biopsies poses difficulties. Our murine observations of perturbed liver PPP metabolites in *Shpk*$^{-/-}$ mice suggest that human metabolic dysregulation is present in tissues, rather than confined only to urine and bloodspots. *Shpk*$^{-/-}$ mice present opportunities for further exploration of the metabolic consequences of *Shpk* protein in other tissues it is found to be highly expressed such as liver,

kidney, and pancreas. Taken together, our data highlights the importance of *in vivo* exploration of simplified *in vitro* findings to better represent the physiological complexity of human biological processes.

Limitations. Our stem cell gene therapy retains remedial efficacy for patients lacking *SHPK*, but presents a few limitations. Patients harboring the 57-kb deletion have homozygous deletions of both *CTNS* and *SHPK* which is not replicated in our current transplantation model. In this regard, we propose similar studies with a double knockout *Ctns*$^{-/-}$/*Shpk*$^{-/-}$ *in vivo* model to investigate if stem cell transplantations of this genotype can still offer effective therapeutic opportunity. While generation of a double knockout mouse was underway, complications arose in inducing successful biallelic CRISPR-Cas9 heritable deletions due to the local proximity of the two genes. In addition, although literature has established that *SHPK* directly modulates macrophage polarization (Haschemi et al., 2012) and cellular and systemic PPP metabolism attenuates inflammatory responses in diseased conditions (Baardman et al., 2018), we did not find inflammatory phenotypes in *Shpk*$^{-/-}$ macrophages (Supplementary File 2, Fig. 6a). Thus, we propose further *in vitro* investigations evaluating *Shpk*$^{-/-}$ macrophage inflammatory functions and trafficking capacity when co-cultured with cystinosis diseased cells, including ELISA-analysis of cytokine secretion in co-culture media and macrophage-mediated lysosomal trafficking following polarization stimulation. Such experiments were complicated by degradation of *Shpk* RNA and protein expression in both cultured bone marrow-derived macrophages (BMDMs) (Supplementary File 2, Fig. 6b) and peritoneal macrophages (data not shown) isolated from *Shpk*$^{-/-}$ mice. These follow-up experiments will further confirm the efficacy of the therapy, as well as elucidate if *Shpk* harbors an inflammatory phenotype in patient cells.

Conclusory Remarks. To maximize remedial benefit for patients undergoing Phase I/II clinical trials of *ex vivo* lentiviral-corrected *CTNS* transduction into patient HSPCs for autologous transplantation, we evaluated pathogenic contributions of *Shpk* metabolic gene in our novel HSPC gene therapy to understand if the predominant absence of *SHPK* in the genome of patients compromises the mechanistic integrity of the macrophage-mediated therapy. We generated and characterized novel *Shpk*$^{-/-}$ mice and evaluated

therapeutic efficacy of *Shpk*$^{-/-}$ HSPCs transplanted into *Ctns*$^{-/-}$ mice for prevention of disease progression. We found that *SHPK* may account for a mild metabolic aspect of the clinical heterogeneity of cystinosis, but evidently may not be responsible for greater physiological consequences of the disease. Furthermore, our *in vivo* findings indicate that *Shpk*-deficient HSPC gene therapy retains long-term remedial benefits for patients with *Shpk* genomic absence. Our findings shed light into the unknown physiological pathology of *SHPK* gene carrying nuances in metabolism, inflammation, and cystinosis. Our data further enhances the therapeutic utility of our stem cell therapy for LSDs. Finally, our findings permit admittance of patients with the 57-kb induced *SHPK*-deficiency into clinical trials for cystinosis.

3.3: Methods

Mice and Ethics Statement. C57BL/6 *Ctns*$^{-/-}$ mice were provided by Dr. Antignac (Inserm U983, Paris, France). Shpk$^{\Delta ATG}$ (C57BL/6 *Shpk*$^{-/-}$) mice were generated by the UCSD Mouse Genomics Core. C57BL/6 blastocysts were injected with CRISPR-Cas9 targets aimed the start codon of Shpk genomic locus. Shpk$^{\Delta E2}$ (C57BL/6 *Shpk*$^{-/-}$) mice with CRISPR-Cas9 targets aimed at exon 2 of *Shpk* were obtained from UC Davis. Both strains were continuously bred to homozygosity. Both strains were also crossbred with transgenic DsRed (B6.Cg-Tg(CAG-DsRed*MST)1Nagy/J) mice provided by the Jackson Laboratory (Bar Harbor, ME) to establish colored lines with constitutive expression of DsRed fluorescent protein. All strains and mouse procedures were approved by University of California, San Diego (UCSD) in accordance with the guidelines set forth by the Institutional Animal Care and Use Committee (Protocol ID S12288).

Mouse Genotyping. Shpk mutant status was identified using PCR-based genotyping assays from mouse tail tissue. DirectPCR (Tail) (Viagen) and Protinease K treatment of mouse tails was used for DNA extraction. PCR protocol of Shpk$^{\Delta ATG}$ DNA amplification is as follows: 95°C (3 min) initial denaturation; 30 cycles of 98°C (20 s) denaturation, 65°C (15 s) annealing, and 72°C (15 s) extension; and 72°C (1 min/kb) final extension. Resultant wild-type band sizes were 632 bp; and mutant size was 495 bp. PCR protocol of Shpk$^{\Delta E2}$ DNA amplification was provided by UC Davis and is as follows: 94°C (2 min) initial denaturation; 10 cycles of 94°C (10 s) denaturation, 65°C (15 s) annealing with consecutive runs lowering in temperature by 1°C (-1°C/cycle), and 68°C (2 min) extension; and 25 cycles of 94°C (2 min) denaturation, 65°C annealing (30 s), and 68°C (2 min) extension with consecutive runs increasing in duration by 20 s (+20 s/cycle). Resultant wild-type band sizes were 638 and 1184 bp; and mutant size was 500 bp. Primer sequences found in Table S1.

Cell isolation and culture. Bone-marrow derived macrophages (BMDMs) were isolated as previously described (Goodman et. al., 2019). To isolate thioglycolate-elicited macrophages, donor mice were

administered 5 ml of 3% thioglycolate via peritoneal injections. Following inflammatory response spanning 5-7 days, isoflurane-euthanized mice were peritoneally injected with 5 ml of PBS, gently massaged, and removed of injected fluid. Isolated peritoneal macrophages were cultured overnight at 37 °C and 5% CO_2 incubation in complete DMEM media (10% FBS, 2% penicillin/streptomycin) on tissue-culture (TC) treated plastic. Media was changed the following day to remove non-macrophages, and subsequent media changes occurred every two days. Fibroblast isolation occurred as previously described (Goodman et. al., 2019) Briefly, small skin biopsies isolated from neonatal mice were attached to culture dishes containing complete DMEM media (10% FBS, 2% penicillin/streptomycin). Fibroblast migration was allowed to occur for several days, after which skin was removed and remaining cells were regularly media changed**.** Co-cultures between 75,000 macrophages and 50,000 fibroblasts were combined in 6-well dishes under polarization conditions for two days.

Real Time-qPCR. RNEasy Mini Kit and protocol (Qiagen, Hilden, Germany) was used for whole RNA extraction; blood RNA was extracted using the RNeasy Protect Animal Blood Kit (Qiagen). cDNA synthesis occurred by reverse transcription of 1 ug tissue and blood RNA using iScript cDNA Synthesis Kit (Bio-Rad, Hercules, CA). RT-qPCR reaction assembly consisted of 5 ul iTaq Universal SYBR Green, 3 μL cDNA (5 ng/ul), 0.6 μL forward and reverse primer (10 μM), and 1.8 μL H20, and ran on a CFX96 thermocycler (Bio-Rad) under the following conditions: 95 °C (30 s); 40 cycles of 95 °C (5 s) and 60 °C (30 s); then 65 °C (5 s); and 95 °C (5 s). Gene expression was measured using the delta/delta CT method relative to glyceraldehyde 3-phosphate dehydrogenase (*Gapdh*). All primer sequences are shown in Supplementary Table 1.

Immunoblotting. RIPA lysis buffer (Sigma, St Louis, MO) composed of protease/phosphatase inhibitor cocktail (Thermo Fisher Scientific, Waltham, MA) was used for protein lysis. The Pierce BCA Protein Assay Kit (Thermo Fisher Scientific) was used to calibrate protein concentrations. SDS-NuPAGE treatment of 10-20 ug of protein were ran on 4–12% Bis-Tris Gel (Novex by Life Technologies, Carlsbad, CA) and

transferred to PVDF membranes. Primary incubation ran at 4 °C overnight using the following antibodies: Anti-Shpk (Abcam; 1:1,000). The next day, membranes were washed three times in Protein Wash Buffer (Azure Biosystems, Dublin, CA) and incubated in HRP-conjugated secondary antibodies goat anti-rabbit (Sigma; 1:2000) and rhodamine anti-tubulin (BioRad; 1:2,000) for 1 hr at RT. Membranes are again washed three times and a final time in 1x tris buffered saline (TBS). Blots were activated by HRP substrate Radiance Plus ECL Reagent (Azure) and chemiluminescent detection was captured on the c600 Imager (Azure).

Metabolomics. Harvested livers were rapidly freeze-clamped and placed in ice-cold liquid nitrogen to preserve robust metabolic activity. Samples were then powderized and 20 mg was suspended in extraction solution (40% methanol/40% acetonitrile/20% H_20) supplemented with 40 µL 13C-labeled internal standards (Cambridge Isotype Laboratories) per mL solution. Samples were homogenized using Precillys homogenizer, immediately returned to dry ice for 1 hr, then spun at 13000 xg for 15 mins. Supernatant was then lyophilized on a speed vac with cold trap to dryness. Mass spectrometry measured relative area ratio relative to urinary creatinine concentrations and/or relative abundance of metabolites.

HSPC isolation and transplantation. HSPC isolation and transplantation were performed as previously described (Harrison et. al., 2013). In brief, bone marrow fluid was flushed from harvested tibias and femurs of donor wild-type, *Ctns*$^{-/-}$, *Shpk*$^{\Delta ATG}$, and *Shpk*$^{\Delta E2}$ mice. Sca1^{+} HSPCs were isolated by immunomagnetic separation using magnetic beads conjugated to anti-ScaI antibody (Miltenyi Biotec, Auburn, CA). *Ctns*$^{-/-}$ mice subjected to 6.5 Gy lethal irradiation the previous day were transplanted with 100 µL containing $1 \times 10_6$ HSPCs via tail vein injection. At ~6 months post-transplantation, recipient mice were sacrificed, and kidney, liver, and spleen samples were isolated for analyses of therapeutic efficacy.

Cystine Content. Tissue cystine was measured as previously described (Harrison et al., 2013). Briefly, explanted tissues were homogenized using the Precellys 24 homogenizer (Bertin Technologies) N-ethylmaleimide (Fluka Biochemika). Lysates were transferred to 15% % 5-sulfosalicylic acid (SSA) (Fluka

Biochemika) and centrifuged to remove proteins for comparative quantitation using BCA assay (Pierce). The cystine-containing supernatants were transferred to 3% SSA and diluted before being quantitated by mass spectrometry at the UCSD Biochemical Genetics as described previously (Gertsman et al., 2016).

Histology. To assess general tissue morphology, dissected tissues were fixed in 10% formalin for 48 hours and transferred to the UCSD Moores Cancer Center Biorepository & Tissue Technology Center. Samples were embedded in paraffin, sectioned at 4μm and stained with routine H&E staining to assess histologic anomalies. For kidney, further analysis was done in order to quantify the extent of cortical damage as previously described (Yeagy et al., 2011). To estimate the extend of the affected parenchyma in kidneys, periodic acid- shift (PAS) staining was also performed, which stains basement membrane, so is useful for evaluating glomerular cell number, basement membrane, mesangium, tubular basement membrane and apical end of the proximal convoluted tubule epithelium's brush border (Agarwal et al., 2012) All kidney's H&E and PAS slides were blindly scored by Dr. Valeria Estrada (Tissue Technology Shared Resource, Moores Cancer Center, UCSD) based on extent of cortical damage ; a grade of 1 corresponded to 0-10% damage, Grade 2 to 10-30%, Grade 3 to 30-50% and Grade 4 to 50-70% (Yeagy et al., 2011).

Immunofluorescence. For marker immunofluorescence, tissues were fixed in 4% paraformaldehyde, dehydrated in 20% sucrose and mounted in Tissue Tek Optimum Cutting Temperature (OCT) stored at -80°C. Tissues were cut into 16 um-wide sections and placed on IHC slides. For staining, slides were washed in PBS three times for 10 mins at RT, treated with blocking buffer (1% BSA, 5% goat serum, 0.3% triton X-100) for 1 hour at RT, and probed with macrophage markers CD68 (Biolegend; 1:500), F4/80 (Abcam; 1:500), and MHCII (Biolegend; 1:500) primary antibodies overnight at 4°C. The following day, slides were washed in PBS three times and probed with secondary antibodies anti-rabbit AF562 (ThermoFisher; 1:500) and phalloidin AF647 (Invitrogen; 1:200) for 1 hour at RT. After two more 10-minute PBS washes and a final PBS and DAPI (1:1000) wash, slides were mounted with glass slips using Prolong Gold. The following day, images were taken using the LSM 880 confocal microscope (Zeiss).

Renal Function and Blood Analyses. 24-hour urine collections were preformed using metabolic cages with collection over ice and treated with 100x Protease Inhibitors (Sigma, St Louis, MO). Renal markers creatinine, creatinine clearance, phosphate, and urea were measured using colorimetric assays according to the manufacturer recommendations (BioAssay Systems, Hayward, CA) as previously described (Harrison et al., 2013). Total protein was measured using Pierce BCA Protein Assay Kit (Thermo Fisher Scientific) as previously described (Harrison et al., 2013). Low molecular weight (LMW) proteinuria indicator Clara cell protein of 16 kDa (CC16) was assayed via ELISA (BIOMATIK) per manufactures recommendation. Plasma serum was obtained from survival retro-orbital bleeding and analyzed for creatinine, phosphate, glucose, and urea. Blood samples were submitted to the UCSD ACP Veterinary Diagnostics Laboratory for hemogram tests determining complete blood count (CBC) and comparative chemistry assessments.

Statistics. All statistics were analyzed using Graphpad Prism 8 software. Briefly, Student's *t*-test was used for comparisons of two groups, and one-way analysis of variance (ANOVA) for comparisons of three or more conditions with Tukey's multiple comparison test used to evaluate differences between individual groups. For histological scoring comparisons, the Kruskal Wallis test was employed, followed by Dunn's multiple correction. All graphs display mean ± standard deviation.

3.4: Acknowledgements

Chapter 3, in part, is currently being prepared for submission for publication of the material, *Goodman S., **Khan M**., Sharma J., Cano J., Zi, L., Estrada, V., Gertsman, I., Cherqui, S. "Shpk-deficient hematopoietic stem cell therapy remains effective to rescue cystinosis."* The master's thesis author was a key investigator and author of this paper.

3.5: References

Agarwal, S.K., Sethi, S., and Dinda, A.K. Basics of kidney biopsy: A nephrologist's perspective. *Indian J Nephrol*. 2013;23:243-252.

Ariceta, G., Giordano, V., & Santos, F. (2019). Effects of long-term cysteamine treatment in patients with cystinosis. *Pediatric Nephrology*, *34*(4), 571–578. https://doi.org/10.1007/s00467-017-3856-4

Atri, C., Guerfali, F. Z., & Laouini, D. (2018). Role of human macrophage polarization in inflammation during infectious diseases. *International Journal of Molecular Sciences*, *19*(6). https://doi.org/10.3390/ijms19061801

Bäumner, S., & Weber, L. T. (2018). Nephropathic cystinosis: Symptoms, treatment, and perspectives of a systemic disease. *Frontiers in Pediatrics*, *6*(March), 1–8. https://doi.org/10.3389/fped.2018.00058

Biffi, A. (2017). Hematopoietic Stem Cell Gene Therapy for Storage Disease: Current and New Indications. *Molecular Therapy*, *25*(5), 1155–1162. https://doi.org/10.1016/j.ymthe.2017.03.025

Biffi, A., Capotondo, A., Fasano, S., Del Carro, U., Marchesini, S., Azuma, H., Malaguti, M. C., Amadio, S., Brambilla, R., Grompe, M., Bordignon, C., Quattrini, A., & Naldini, L. (2006). Gene therapy of metachromatic leukodystrophy reverses neurological damage and deficits in mice. *Journal of Clinical Investigation*, *116*(11), 3070–3082. https://doi.org/10.1172/JCI28873

Buntinx, L., Voets, T., Morlion, B., Vangeel, L., Janssen, M., Cornelissen, E., Vriens, J., De Hoon, J., & Levtchenko, E. (2016). TRPV1 dysfunction in cystinosis patients harboring the homozygous 57 kb deletion. *Scientific Reports*, *6*(September), 1–9. https://doi.org/10.1038/srep35395

Cherqui, S., Sevin, C., Hamard, G., Kalatzis, V., Sich, M., Pequignot, M. O., Gogat, K., Abitbol, M., Broyer, M., Gubler, M.-C., & Antignac, C. (2002). Intralysosomal Cystine Accumulation in Mice Lacking Cystinosin, the Protein Defective in Cystinosis. *Molecular and Cellular Biology*, *22*(21), 7622–7632. https://doi.org/10.1128/mcb.22.21.7622-7632.2002

Cherqui, Stephanie. "Stem Cell Gene Therapy for Cystinosis - Tabular View." *Tabular View - ClinicalTrials.gov*, clinicaltrials.gov/ct2/show/record/NCT03897361?view=record.

Cohen, C., Charbit, M., Chadefaux-Vekemans, B., Giral, M., Garrigue, V., Kessler, M., Antoine, C., Snanoudj, R., Niaudet, P., Kreis, H., Legendre, C., & Servais, A. (2015). Excellent long-term outcome of renal transplantation in cystinosis patients. *Orphanet Journal of Rare Diseases*, *10*(1), 4–11. https://doi.org/10.1186/s13023-015-0307-9

Canté-Barrett, K., Mendes, R. D., Smits, W. K., Van Helsdingen-Van Wijk, Y. M., Pieters, R., & Meijerink, J. P. P. (2016). Lentiviral gene transfer into human and murine hematopoietic stem cells: Size matters. *BMC Research Notes*, *9*(1), 1–6. https://doi.org/10.1186/s13104-016-2118-z

Das, A., Sinha, M., Datta, S., Abas, M., Chaffee, S., Sen, C. K., & Roy, S. (2015). Monocyte and Macrophage Plasticity in Tissue Repair and Regeneration. *American Journal of Pathology*, *185*(10), 2596–2606. https://doi.org/10.1016/j.ajpath.2015.06.001

Duran-struuck, R., & Dysko, R. C. (2009). *Bmt Review*. *48*(1), 11–22.

Emma, F., Nesterova, G., Langman, C., Labbé, A., Cherqui, S., Goodyer, P., Janssen, M. C., Greco, M., Topaloglu, R., Elenberg, E., Dohil, R., Trauner, D., Antignac, C., Cochat, P., Kaskel, F., Servais, A., Wühl, E., Niaudet, P., Van't Hoff, W., … Levtchenko, E. (2014). Nephropathic cystinosis: An international consensus document. *Nephrology Dialysis Transplantation*, *29*, iv87–iv94. https://doi.org/10.1093/ndt/gfu090

Gaide Chevronnay, H. P., Janssens, V., Van Der Smissen, P., N'Kuli, F., Nevo, N., Guiot, Y., Levtchenko, E., Marbaix, E., Pierreux, C. E., Cherqui, S., Antignac, C., & Courtoy, P. J. (2014). Time course of pathogenic and adaptation mechanisms in cystinotic mouse kidneys. *Journal of the American Society of Nephrology*, *25*(6), 1256–1269. https://doi.org/10.1681/ASN.2013060598

Gertsman I, Johnson WS, Nishikawa C, Gangoiti JA, Holmes B, Barshop BA. Diagnosis and Monitoring of Cystinosis Using Immunomagnetically Purified Granulocytes. *Clin Chem*. 2016;62(5):766-772. doi:10.1373/clinchem.2015.25249

Goodman, S., Naphade, S., **Khan, M.**, Sharma, J., & Cherqui, S. (2019). Macrophage polarization impacts tunneling nanotube formation and intercellular organelle trafficking. *Scientific Reports*, *9*(1). https://doi.org/10.1038/s41598-019-50971-x

Haschemi, A., Kosma, P., Gille, L., Evans, C. R., Burant, C. F., Starkl, P., Knapp, B., Haas, R., Schmid, J. A., Jandl, C., Amir, S., Lubec, G., Park, J., Esterbauer, H., Bilban, M., Brizuela, L., Pospisilik, J. A., Otterbein, L. E., & Wagner, O. (2012). The sedoheptulose kinase CARKL directs macrophage polarization through control of glucose metabolism. *Cell Metabolism*. https://doi.org/10.1016/j.cmet.2012.04.023

Hasilik, A., Klein, U., Waheed, A., Strecker, G., & von Figura, K. (1980). Phosphorylated oligosaccharides in lysosomal enzymes: Identification of α-N-acetylglucosamine (1)phospho(6)mannose diester groups. *Proceedings of the National Academy of Sciences of the United States of America*, *77*(12 II), 7074–7078. https://doi.org/10.1073/pnas.77.12.7074

Harrison, F., Yeagy, B. A., Rocca, C. J., Kohn, D. B., Salomon, D. R., & Cherqui, S. (2013). Hematopoietic stem cell gene therapy for the multisystemic lysosomal storage disorder cystinosis. *Molecular Therapy*, *21*(2), 433–444. https://doi.org/10.1038/mt.2012.214

Kardon, T., Stroobant, V., Veiga-da-Cunha, M., & Schaftingen, E. Van. (2008). Characterization of mammalian sedoheptulokinase and mechanism of formation of erythritol in sedoheptulokinase deficiency. *FEBS Letters*, *582*(23–24), 3330–3334. https://doi.org/10.1016/j.febslet.2008.08.024

Martino, S., Emiliani, C., Tancini, B., Severini, G. M., Chigorno, V., Bordignon, C., Sonnino, S., & Orlacchio, A. (2002). Absence of metabolic cross-correction in Tay-Sachs cells: Implications for gene therapy. *Journal of Biological Chemistry*, *277*(23), 20177–20184. https://doi.org/10.1074/jbc.M106164200

Murphy, Jerome & Papathakis, Peggy. (1993). Hypercholesterolemia in children with cystinosis. Pediatric nephrology (Berlin, Germany). 7. 159-62. 10.1007/BF00864385

Nagy, C., & Haschemi, A. (2015). Time and demand are two critical dimensions of immunometabolism: The process of macrophage activation and the pentose phosphate pathway. *Frontiers in Immunology*, *6*(APR), 1–8. https://doi.org/10.3389/fimmu.2015.00164

Nagy, C., & Haschemi, A. (2013). Sedoheptulose kinase regulates cellular carbohydrate metabolism by sedoheptulose 7-phosphate supply. *Biochemical Society Transactions*, *41*(2), 674–680. https://doi.org/10.1042/BST20120354

Penati, R., Fumagalli, F., Calbi, V., Bernardo, M. E., & Aiuti, A. (2017). Gene therapy for lysosomal storage disorders: recent advances for metachromatic leukodystrophy and mucopolysaccaridosis I. *Journal of Inherited Metabolic Disease*, *40*(4), 543–554. https://doi.org/10.1007/s10545-017-0052-4

Pu, J., Guardia, C. M., Keren-Kaplan, T., & Bonifacino, J. S. (2016). Mechanisms and functions of lysosome positioning. *Journal of Cell Science*, *129*(23), 4329–4339. https://doi.org/10.1242/jcs.196287

Rastall, D. P. W., & Amalfitano, A. (2015). Recent advances in gene therapy for lysosomal storage disorders. *Application of Clinical Genetics*, *8*, 157–169. https://doi.org/10.2147/TACG.S57682

Rocca, C. J., & Cherqui, S. (2019). Potential use of stem cells as a therapy for cystinosis. *Pediatric Nephrology*, *34*(6), 965–973. https://doi.org/10.1007/s00467-018-3974-7

Shelke, A. R., Roscoe, J. A. , Morrow, G. R. , Colman, L. K. , Banerjee, T. K. , & Kirshner, J. J. (2008). NIH Public Access. *Bone*, *23*(1), 1–7. https://doi.org/10.1038/jid.2014.371

Syres, K., Harrison, F., Tadlock, M., Jester, J. V., Simpson, J., Roy, S., Salomon, D. R., & Cherqui, S. (2009). Successful treatment of the murine model of cystinosis using bone marrow cell transplantation. *Blood*, *114*(12), 2542–2552. https://doi.org/10.1182/blood-2009-03-213934

Thoene, J. G., Oshima, R. G., & Crawhall, J. C. (1976). Intracellular cystine depletion by aminothiols in vitro and in vivo. *Journal of Clinical Investigation*, *58*(1), 180–189. https://doi.org/10.1172/JCI108448

Turner, A. R., Sridharan, S., Ratajczak, M. Z., Janowska-Wieczorek, A. (2012). NIH Public Access. *Bone*, *23*(1), 1–7. https://doi.org/10.1038/jid.2014.371

Wamelink, M. M. C., Ramos, R. J. J. F., van den Elzen, A. P. M., Ruijter, G. J. G., Bonte, R., Diogo, L., Garcia, P., Neves, N., Nota, B., Haschemi, A., Tavares de Almeida, I., & Salomons, G. S. (2015). First two unrelated cases of isolated sedoheptulokinase deficiency: A benign disorder? *Journal of Inherited Metabolic Disease*, *38*(5), 889–894. https://doi.org/10.1007/s10545-014-9809-1

Wamelink, M. M. C., Struys, E. A., Jansen, E. E. W., Levtchenko, E. N., Zijlstra, F. S. M., Engelke, U., Blom, H. J., Jakobs, C., & Wevers, R. A. (2008). Sedoheptulokinase deficiency due to a 57-kb deletion in cystinosis patients causes urinary accumulation of sedoheptulose: Elucidation of the CARKL gene. *Human Mutation*, *29*(4), 532–536. https://doi.org/10.1002/humu.20685

Chapter 4: Conclusions

This thesis sought to expound on the underlying cellular, molecular, and physiological mechanisms involved in the optimization of a stem cell gene therapy for cystinosis. While current drug therapies temporarily alleviate symptoms, regenerative medicine proffer long-lasting remedies that wholly resolve genomic and functional consequences of the disease. Our group pioneered the successful application of HSPC transplantation therapy on a *Ctns* knockout (*Ctns*$^{-/-}$) murine model of cystinosis. As the utility of this potential therapy is currently being translated into Phase I/II human clinical trials, our group moved to characterize the inflammatory mechanisms and metabolic influences surrounding the gene therapy to ultimately elucidate the therapeutic viability for patients in the clinical trials.

Previous studies showed that HSPC-derived macrophages supply healthy *Ctns*-bearing lysosomes to diseased tissue via TNT-mediated intracellular trafficking leading to disease rescue (Rocca and Cherqui 2019). Chapter 2 of this thesis investigated the effects of inflammatory polarization conditions on the disease rescue capacity of transplanted macrophages. We found that pro-inflammatory stimulation of in vivo, but not in vitro, interactions of WT cells with cystinotic environments facilitated disease rescue. These findings highlight the limitations presented by *in vitro* systems that may be resolved by the replication of complex physiological processes *in vivo* models which collectively better represent human biology.

The most prevalent cystinosis mutation constitutes 57-kbp homozygous deletions of *CTNS*, as well as adjacent PPP enzyme *SHPK* (Buntix et al., 2016), which has been found to directly regulation macrophage polarization. Chapter 3 of this thesis characterized the pathological contribution of *SHPK* to cystinosis symptom profile, as well as evaluated if *Shpk*-deficient HSPCs – the genotype of the majority of patients – will still benefit from macrophage-mediated gene therapy. We found a minimal metabolic phenotype isolated to *Shpk*-deficiency and confirmed that *Shpk*$^{-/-}$ HSPCs retain the capacity to induce multisystemic disease prevention, indicating that *Shpk*-deficiency likely does not impact therapeutic efficacy of HSPC gene therapy for all patients in clinical trials.